UNIVERSITE D'ANTANANARIVO
FACULTE DES SCIENCES
ECOLE DOCTORALE : PHYSIQUE ET APPLICATIONS

EAD : Physique Nucléaire et Physique des Hautes Energies
Laboratoire de Physique des Hautes Energies

THESE

Pour l'obtention du diplôme de
DOCTORAT EN PHYSIQUE
Spécialité : Physique des Hautes Energies
sur:

MEASUREMENTS OF CROSS-SECTION OF CHARGE CURRENT INCLUSIVE OF ANTINEUTRINO SCATTERING OFF NUCLEONS USING CARBON, IRON, LEAD AND SCINTILLATOR AT MINERνA FOR 2GEV < E_ν < 20GEV

Présentée par :
RAKOTONDRAVOHITRA Laza
Devant la commission d'examen composée de :

Président: M. RAMBOLAMANANA Gérard
Professeur Titulaire de l'Université d'Antananarivo

Rapporteur : M. Steven Dytman
Professeur Titulaire de l'Université de Pittsburgh

Mme RAMANANTSIZEHENA Georgette
Professeur Titulaire de l'Université d'Antananarivo

Examinateur: Mme ANDRIANTSOA Esther
Professeur Titulaire de l'Université d'Antananarivo

M. RAVELOMANANTSOA Solofonirina Dieudonné
Professeur de l'Université d'Antananarivo

Directeurs de Thèse:
M. RABOANARY Roland
Professeur Titulaire de L'Université d'Antananarivo

M. Jorge G Morfin
Directeur de recherche à Fermi National Accelerator Laboratory

M. Herman B White
Directeur de recherche à Fermi National Accelerator Laboratory

Le 18 Août 2015

UNIVERSITE D'ANTANANARIVO
FACULTE DES SCIENCES
ECOLE DOCTORALE : PHYSIQUE ET APPLICATIONS

EAD : Physique Nucléaire et Physique des Hautes Energies
Laboratoire de Physique des Hautes Energies

THESE

Pour l'obtention du diplôme de
DOCTORAT EN PHYSIQUE
Spécialité : Physique des Hautes Energies
sur:

MEASUREMENTS OF CROSS-SECTION OF CHARGE CURRENT INCLUSIVE OF ANTINEUTRINO SCATTERING OFF NUCLEONS USING CARBON, IRON, LEAD AND SCINTILLATOR AT MINERνA FOR 2GEV < E_ν < 20GEV

Présentée par :
RAKOTONDRAVOHITRA Laza

Devant la commission d'examen composée de :

Président: M. RAMBOLAMANANA Gérard
Professeur Titulaire de l'Université d'Antananarivo

Rapporteur : M. Steven Dytman
Professeur Titulaire de l'Université de Pittsburgh

Mme RAMANANTSIZEHENA Georgette
Professeur Titulaire de l'Université d'Antananarivo

Examinateur: Mme ANDRIANTSOA Esther
Professeur Titulaire de l'Université d'Antananarivo

M. RAVELOMANANTSOA Solofonirina Dieudonné
Professeur de l'Université d'Antananarivo

Directeurs de Thèse:
M. RABOANARY Roland
Professeur Titulaire de L'Université d'Antananarivo

M. Jorge G Morfin
Directeur de recherche à Fermi National Accelerator Laboratory

M. Herman B White
Directeur de recherche à Fermi National Accelerator Laboratory

Le 18 Août 2015

ABSTRACT

MEASUREMENTS OF CROSS-SECTION OF CHARGE CURRENT INCLUSIVE OF ANTINEUTRINO SCATTERING OFF NUCLEONS USING CARBON, IRON, LEAD AND SCINTILLATOR AT MINERνA FOR 2GEV $< E_\nu <$ 20GEV

Laza Rakotondravohitra, PhD

Neutrino physics is one of the most active fields in the domaine of high energy physics during the last century. The need of precise measurement of neutrino-nucleus interactions required by the neutrino oscillation experiments is a an exiting step. These measurements of cross-section are more than essential for neutrino oscillation experiment. Over the year, many measurements from varieties of experiments have been presented. MINERνA is one of the world leaders in measuring cross-section of neutrino and antineutrino -nucleus interactions. MINERνA is a neutrino-nucleus scattering experiment installed in the few-GeV NuMI beam line at Fermilab. In order to study nuclear dependence, MINERνA is endowed with different types of solid nuclear targets as well are liquid targets such as helium and water.

This thesis presents measurements of cross-section of antineutrino scattering off nucleons using a variety of solid nuclear targets, carbon, iron, lead and also polystyrene scintillator (CH). The data set of antineutrino used for this analysis was taken between March and July 2010 with a total of 1.60×10^{20} protons on target. Charged current inclusive interactions were selected by requiring a positive muon and kinematics limitation of acceptance of the muon spectrometer are applied. The analysis requires neutrino energy between 2GeV et 20GeV and the angle of muon $\theta_m u < 17$degree . The absolute cross-section σ as function of neutrino energy and the differential cross-section $\frac{d\sigma}{dx_{bj}}$ measured and shown the corresponding systematics for each nuclear targets. Data results are compared with prediction of the models implemented in the neutrino events generators GENIE 2.6.2

used by the experiment.

TABLE OF CONTENTS

LIST OF TABLES

LIST OF FIGURES

PREFACE

To my family Above all, thanks to God for all of the blessings that I am going to list.
Being far from family is hard, and work is not easy, but in every situation, I have a loving wife and that make everything different, thank you Henintsoa for being always supportive and patient.
I would not be able to do anything if my family did not supported me, during all the year that I kept studying, all I had was endless encouragements. I would like to thank my parent Miarison and Martine for their love and support. I have been blessed because that type of endless encouragements doubled with my parents in-law Michel and Tiana, I am blessed to have loving people in my life. I can not forget my little sister Mamy and Fanarenantsoa. I would like thanks my family at Warrenville Bible chapel. The Schleicher's especially Kevin and Karen, The Fox's Bob and Rebecca and all good friends at Warrenville that always supported us in so many ways but especially in prayers.

PREFACE

I owe thanks to many people for the support during my time as graduate student. One of the greatest opportunity that I had is to represent the University of Antananarivo to make research at Fermilab, so I would like to thank Pr Roland Raboanary for his support since my bachelor until now. His understanding help me to improve in many trial as graduate student at the University. I owe thanks to a great mentor and supervisor.

Dr Jorge G Morfin, he welcomed me at Fermilab and never gave up on me, thank you for finding a group where I can grow and learn a young student. I would like to thank him for all the knowledge that he transmitted during all the weekly meeting that we had. I would like to express my gratitude to Dr. Deborah Harris, I learned many things by interacting with Debbie, Her love of physics is translated into high valued patience to all student that worked on MINERνA. I would like to thank Pr Kevin MacFarland for the opportunity working on the experiment.

My sincere gratitude to the leaders of the University which are:

The president of the University of Antananarivo, Pr RAMANOELINA Panja

The Dean of the Faculty of Science, Pr RAHERIMANDIMBY Marson

The head of the department of Physics, Dr RAKOTONDRAMANANA Hery Tiana which I hope the work that we started together for collaboration in the neutrino experimental area will be more than productive for the good of our colleagues and researchers.

I would like to express my gratitude to the Pr RAMBOLAMANANA Gérard. it is an honor for me that you agreed to attend and preside this thesis.

An honor and a pride is to be a doctoral student of the newly Doctoral School of the Department of Physics, thank you Professor RAMANANTSIZEHENA Georgette for your support and understanding during the process of this thesis.

My sincere gratitude to the jury of this thesis, among them Pr ANDRIANTSOA Esther, you are giving me honor by agreeing to be a member of the commission of this doctorat.
Also Pr RAVELOMANANTSOA Solofonirina Dieudonné of the University of Antananarivo, I appreciate very much your support during many years at the Department of Nuclear Physics, thank you for accepting attending this defense as member of the Jury.

Professor Steve Dytman from University of Pittsburgh, Thank you for visiting our country and give a talk to motivate graduate students in our department, Thank for agreeing to attend the thesis as a member of the jury, It has been a great experience to work with you at MINERνA.

I would like to thank all the professors at the Department of Physics, I have learned life time experiences with all of you and I wish you well.

I would like to thank all my colleagues at the University of Antananarivo and especially the Department of Physics and the High Energy Physics Departement especially Andry and Fenosoa as well as Fenompaniriana.

This work has been funded by the Neutrino Division and Fermilab International Fellow, an unique and great opportunity as young scientist.

I can't forget the organizer of the ASP Physics, including Dr Christine Darve and Pr Young Kee Kim. This fellow is a unique opportunity and I am so blessed that I have been selected to come here. It opened many doors for me. I did learn quiet a few things during my stay at Fermilab, and many people have been involved during the process of the learning, I would like to express my gratitude to all MINERνA collaborates, former or current. Special thanks for my former co-worker David Martinez. I must thank all those who have helped contribute to my professional development.
I have a deep gratitude to the group learned Pr Steve Dytman who honored me by agreeing being one of the jury of this thesis, Jeff Nelson and Heather Ray. I have had the blessing of having

great colleagues and friends in particular Jose Palomino, Arturo Fiorentini, Brian Tice, Trung Le, Edgar Valencia, Matues Carneiro, Joseph Manungu and Dipak Rimal, Antonio Zegara, I did learn so much by working with Emily Maher-Aaron Mislec and Chris Marshal at the Calibration group so thank you. I would like to thank the Latin America Madagascar Fermilab group, I enjoyed all meeting and friendship that we had. I would like to thanks special people that impact me through their work, Laura Fields, Heidi Schellman and Dave Schmitz.

1.0 INTRODUCTION

The subatomic particles called neutrino was thought to be a crucial part in the formation of the universe but they are also part of our everyday existence. Trillions of neutrinos pass through our body without interaction every second, but scientists know very little about them because they are almost impossible to isolate and study. However high energy physicist at Fermi National Accelerator Laboratory know as Fermilab are working to understand neutrinos and in the process, they hope to transform the facility into the the neutrino research center of the world. High Energy physicists seek to understand the fundamental particles and the forces that act upon them. Understanding the famous ghost particle called neutrino is one of the challenges that experimental physics is currently facing, neutrinos are one of these fundamentals particles and it is one of the least understood causing interest and need to fully describe neutrino mass and oscillations. Neutrino interaction cross sections are an essential ingredient in most neutrino experiments. MINERνA is one of the experiments located at Fermilab dedicated to provides informations about neutrino cross-section. MINERνA is fine grained neutrino scattering experiment designed to perform precision studies of neutrino-nucleus scattering using ν_μ and $\overline{\nu}_\mu$ neutrinos incident at 1-20 GeV in the NuMI beam at Fermilab. Neutrino interaction cross section measurements are fundamental to understand the behavior and structure of nucleons and nuclei in weak interactions.

This thesis describe the results of our research at the Main Injector Neutrino Experiment for ν - A known as MINERνA. This work consists of the first measurement of the ratios of cross-section as a function of neutrino energy and differential cross-section as a function of Bjorken x for antineutrino charged current inclusive interactions on carbon, lead , iron and hydrocarbon (CH). The first chapter describes briefly the history of neutrinos from theoretical conception to the Standard Model and its limitations, general aspects of neutrino physics will be described as well as theoretical formalism of charged current neutrino-nucleon scattering.

- **Chapters 2** is a full description of the MINERνA detector and the source of neutrino or NuMI Beam line located at Fermi National Accelerator Laboratory.
- **Chapter 3** describes the calibration of the detector and the general event reconstruction.
- **Chapter 4** is about specific reconstruction techniques used by this analysis.
- **Chapter 5** discusses the neutrino interaction simulation.
- **Chapter 6** describes the analysis of $\overline{\nu}_\mu$ charge current analysis on the passive target region of MINERνA.
- **Chapter 7** reports the conclusion of the measurement of charge current inclusive on different nuclei along side with the discussion and the impact of the measurements on the neutrino interaction physics community.

1.1 BRIEF HISTORY OF THE NEUTRINO

One of the most significant discovery of particle physics in recent years is the ability of neutrinos to oscillate from one flavor to another as they propagate through space. But before that breakthrough, neutrinos passed through a long and probing history within the nuclear physics and high energy physics communities.

Neutrinos are light neutral particles that do not interact through the strong nuclear force.

When neutrinos meet matter, they travel deep within the nucleus and interact, then they either continues on as a neutrino or change to its associated lepton. Von Bayer, Otto Hahn and Lise Meitner [3],in 1911 suggested after their experiment that the energy emitted in the beta decay has a continuos spectrum rather than discrete, a experimental observation which is inconsistent to the energy conservation law due to the loss of energy during the process.

$$n \rightarrow p + e + \bar{\nu} \tag{1.1}$$

During a famous physics conference in Tubingen, Germany in 1930, Wolfgang Pauli proposed the solution that could solve the problem, the existence of a neutral weakly interacting fermion emitted in the beta decay. This neutral fermion, with a mass closer to the mass of electron and without electric charge, was called neutron. But when Chadwick, in 1932 discovered the neutron

that we know today [6] , Enrico Fermi gave the name of neutrino to the particle that Wolfgang Pauli proposed. After a comparison between Fermi[8] spectrums and Perrin[8] spectrums it was postulated that the neutrino should have no mass.

In 1934, Fermi[7] used Dirac, Heisenberg and Pauli ś quantum electrodynamics to formally develop the beta decay theory. This theory predicted that inverse beta decay was also possible.

$$\bar{\nu}_e + p \rightarrow n + e^+ \tag{1.2}$$

Then back in 1956 Reines and Cowan[8] made the first direct observation of the neutrino by using a nuclear reactor as a source of 1 MeV antineutrinos and a target of water and cadmium chloride to observe the reaction. The very small interaction probability required the very intense flux of antineutrinos provided by the reactor and a very large volume of the target. In 1958, Goldhaber observed that neutrinos have left hand helicity [9] and in 1959 Davis showed that a ν can be distinguished from its antiparticle $\overline{\nu}$. Leon Lederman lead an experiment [11] in 1960 at the Brookhaven Alternating Gradient Synchrotron (AGS) detected a new type of neutrino, the muon neutrino ν_μ. Followed a decade later by the observation of the weak neutral currents[12] by the magnificent Gargamelle giant bubble chamber at CERN using a beam of $\overline{\nu}$.

Experiments with solar neutrinos began on 1968 when Davis [13] revealed a discrepancy between theoretical predictions and the measured solar neutrino flux. This discrepancy came to be known as the solar neutrino problem. A discrepancy between the expected and the measured flux was also observed in experiments with atmospheric neutrinos that registered the apparent disappearance of muon neutrinos in a hundred of kilometers of propagation. The experiments that measured the flux of solar neutrinos found results suggesting that electron neutrinos disappeared in the traveling distance between Sun and Earth. These result led Gribov and Pontecorvo[14], in 1968, to describe neutrino flavor oscillation if the neutrinos have mass. The disappearance of atmospheric neutrinos (ν_μ) and solar neutrinos (ν_e) is impossible to explain in oscillation terms if mass terms are not included. It is important to notice that neutrino oscillation is not predicted by the Standard Model.

The discovery of the neutrinos and neutrino oscillations started a new era of physics. We have found evidences that neutrinos have mass a fact that goes beyond the Standard Model despite its overwhelming success. It is referred to Physics beyond the Standard Model since it can not explain

Boson	Spin	Charge	Mass (GeV/c^2)	Role
photon	1	0	0	Mediate electromagnetic force
$W^{\pm}$	1	± 1	80.385	Mediate charge current weak interactions
Z	1	0	91.188	Mediate neutral current weak interactions
gluons	1	0	0	Mediate strong nuclear force
Higgs	0	0	≈ 125	Excitation in the Higgs field

Table 1.1: A list of the fundamental bosons described by the Standard Model [4] [5] [6].

all observed phenomena. To provide more experimental evidences,many important neutrino beam facilities have been built at JPARC, CERN and Fermilab.

1.2 NEUTRINO AMONG THE FUNDAMENTAL PARTICLES

The Standard Model describes the dynamics of three fundamental forces, electromagnetism, the weak force, and the strong force. Each force is described in terms of the exchange of gauge bosons. Table 1.3 lists the fundamental bosons described by the Standard Model along with various properties of each particle.

The fundamental particles described in the Standard Model consist of fermions and gauge bosons. The fermions are categorized into quarks and leptons and each particle has a matching antiparticle with the same mass but opposite quantum numbers. Fermions have half-integer spin while bosons have integer spin. Fermions are so named since they obey Fermi statistics while bosons obey Bose-Einstein statistics. Fermions also obey the Dirac equation (1.3).

$$(\mathrm{i}\hbar\gamma^{\mu}\frac{\partial}{\partial \mathrm{x}_{\mu}} - \mathrm{mc})\psi = 0, \tag{1.3}$$

where the term ψ is the four component spinor field describing a fermion and γ^{μ} are the Dirac matrices. There are six species of quarks – up (u), down (d), strange (s), charm (c), bottom (b), and top (t) – arranged into three pairs called generations: ud, cs, and tb. The leptons are comprised of three neutrinos and three charged leptons and are also arranged into three generations: $e\nu_e$, $\mu\nu_{\mu}$,

Type of Particle	Spin	Charge	Interacts Strongly?	Mass
Quarks				
u	1/2	2/3	Yes	2.3 MeV/c^2(speculative)
d	1/2	-1/3	Yes	4.8 MeV/c^2
c	1/2	2/3	Yes	1.275 GeV/c^2
s	1/2	-1/3	Yes	95 MeV/c^2
t	1/2	2/3	Yes	173.5 GeV/c^2
b	1/2	-1/3	Yes	4.65 GeV/c^2
Leptons				
e	1/2	-1	No	0.5486 MeV/c^2
ν_e	1/2	0	No	$\sum_{\alpha=e,\mu,\tau} m_{\nu_\alpha} <$ 0.3-1.5 eV/c^2
μ	1/2	-1	No	105.7 MeV/c^2
ν_μ	1/2	0	No	$\sum_{\alpha=e,\mu,\tau} m_{\nu_\alpha} <$ 0.3-1.5 eV/c^2
τ	1/2	-1	No	1.777 GeV/c^2
ν_τ	1/2	0	No	$\sum_{\alpha=e,\mu,\tau} m_{\nu_\alpha} <$ 0.3-1.5 eV/c^2

Table 1.2: A list of the three generations of fundamental fermions and their properties. Only limits exist on the masses of neutrinos [6].

and $\tau\nu_\tau$.

Particles composed of quarks are known as hadrons. The property of color determines the type of particles that can be formed by quarks. There are two general types of hadrons, mesons and baryons. Mesons are generally made up of a quark and an anti-quark. No stable forms of mesons exist in nature. Baryons are composed of either three quarks or three anti-quarks. The protons and neutrons found in atomic nuclei are types of baryons. The total number of baryons found in the universe is conserved within the Standard Model.

Baryons heavier than the proton and mesons often decay weakly. In the case of charged pions, the decay is generally $\pi^\pm \rightarrow \mu^\pm + \bar{\nu}_\mu(\nu_\mu)$. For mesons and baryons composed of heavier quarks, the heavy quarks decay weakly to light quarks. The weak force mixes quark flavors as described by the Cabibbo-Kobayashi-Maskawa (CKM) matrix [20]. Both mesons and baryons are color-neutral. Neither naked color or naked quarks have been observed in nature. This is due to the nature of the strong force.

Neutrinos are classified as leptons, there are three generations of leptons, each generation being

composed of a charged lepton and a neutrino. The first generation is composed of an electron (e) and electron-neutrino (ν_e), the second of a muon (μ) and muon-neutrino (ν_μ), and the third of a tau (τ) and tau neutrino (ν_τ). Properties of leptons are listed in Table 1.2. Like quarks, particles of each generation differ in mass. Unlike quarks, leptons are associated with another property, lepton number, conserved by interactions within the Standard Model. Lepton number is conserved separately for each generation. Lepton number is found by associating +1 for a charged lepton or its neutrino partner and -1 for an anti-matter charged lepton or its anti-neutrino partner. For example, muons typically undergo the decay $\mu^- \rightarrow e^- + \bar{\nu}_e + \nu_\mu$. In this case, the μ^- has muon lepton number 1. In the decay, a ν_μ is created which also has muon lepton number of 1. In this case, the muon lepton number is 1 before and after the decay. An electron is also involved in the decay and necessary to conserve charge. The electron has a electron lepton number of 1. If a $\bar{\nu}_e$ were not also created in the decay, which has electron lepton number of -1, the decay would not conserve lepton number. Since a $\bar{\nu}_e$ is created, the total electron number is 0 before the decay and is 1 - 1 = 0 after the decay. Note that neutrino oscillation, described in Section 1.3, violates lepton number. Despite this violation, the actual Standard Model interactions conserve lepton number.

The Standard Model describes the dynamics of three fundamental forces, electromagnetism, the weak force, and the strong force. Table 1.3.There are four spin-1 vector gauge bosons. The W and Z bosons mediate the weak force, the photon γ mediates the electromagnetic force, and the gluon g mediates the strong force. The fifth boson is a spin-0 scalar called the Higgs boson (H) and is responsible for providing itself and other particles with mass. Tables 1.3 and 1.4 summarize the properties of the fundamental particles and the fundamental forces that act between them.

1.2.1 Neutrino Properties

Neutrinos are one of the the fundamental particle in the universe, the other knowns particles are the charge leptons and the quarks, that make up the proton and neutron which make up us. Neutrinos are very much fundamentals as the quarks but they interact very rarely so they are much harder to detect. That being said, there are huge numbers of them so they are big influence of how the universe have involved. For every proton, neutron or electron, the universe contains 1 billion neutrinos. Neutrinos are in abundance ; therefore, it is important to have a comprehensive knowledge

Table 1.3: Properties of bosons.

Particle	Force or Effect	Mass (GeV/c^2)	Charge (e)
Gluon	Strong	0	0
Photon	Electromagnetic	0	0
$W^{\pm}$	Weak	81.8	$\pm$1
Z	Weak	92.6	0
H	Provides mass to particles	126	0

Table 1.4: Properties of fermions.

Particle	Mass (MeV/c^2)	Lifetime (s)	Charge (e)	Weak Force?	Strong Force?
ν_e	undefined	∞	0	yes	no
e	0.511	∞	-1	yes	no
ν_μ	undefined	∞	0	yes	no
μ	105.7	2.2×10^{-6}	-1	yes	no
ν_τ	undefined	∞	0	yes	no
τ	1784	3.3×10^{-13}	-1	yes	no
u	1–5	∞	2/3	yes	yes
d	3–9	∞	-1/3	yes	yes
c	1.15–1.35$\times10^3$	–	2/3	yes	yes
s	75–170	–	-1/3	yes	yes
t	174.3$\times10^3$	–	2/3	yes	yes
b	4–4.4$\times10^3$	–	-1/3	yes	yes

about them. Several properties of neutrinos have already been observed and measured. Neutrinos are neutral and interact through the weak force and gravity. Only left-handed (LH) neutrinos and right-handed (RH) anti-neutrinos are created in Standard Model interactions. In the Standard Model, RH neutrinos and LH anti-neutrinos would not couple weakly. If boosted into the proper reference frame, LH neutrinos would appear as RH neutrinos and RH anti-neutrinos as LH anti-neutrinos to an observer at rest in that reference frame. This is fairly impractical given the tiny mass of neutrinos. This would not be possible if neutrinos were massless, but the discovery of neutrino oscillation established that neutrinos do in fact have mass.

1.2.2 Neutrino Flavors

The standard model of particle physics contains three neutrino flavors: ν_e, ν_μ and ν_τ. Each neutrino forms a doublet with a corresponding charged lepton. The ν_τ was discovered not even 13 years ago[7]. The number of neutrinos participating in the electroweak interaction can be determined by the Z^0 decay width. It was beautifully confirmed at LEP (CERN)[9, 10, 11, 19], long before the observation of the ν_τ, that there are only three light neutrinos.

In 1995 Liquid Scintillator Neutrino Detector (LSND) claimed that three neutrinos were not enough to explain their results and introduced a sterile neutrino [14]. This sterile neutrino does not undergo weak interactions nor interacts in any other way (except gravity).

1.2.3 Helicity

Wu showed in the late 1950s that parity is violated in weak interactions [22] and Goldhaber [23] observed that neutrinos have spin antiparallel to their momentum (left-handed) and antineutrinos have it parallel (right-handed). Therefore, only left-handed neutrinos and right-handed antineutrinos are included in the Standard Model.

1.2.4 Neutrino mass

Currently, the absolute values of the neutrino masses are unknown and the Standard Model assumes that neutrinos are massless. However, no fundamental aspect of the Standard Model

forbids massive neutrinos and it is quite straightforward to insert neutrino mass terms into the Standard Model Lagrangian. There are two basic methods to generate neutrino mass terms that are both gauge and Lorentz invariant [24].

Dirac mass. This can be obtained by assuming the same mechanism (Higgs Mechanism) which explains the generation of masses of charged fermions and quarks, also for neutrinos, though in this case, the much smaller Yukawa couplings for neutrinos would be a mystery [1]. The mass term in the Lagrangian is:

$$\mathcal{L}_{Dirac} = -(\overline{\nu}_L M \nu_R + \overline{\nu}_R M \nu_L), \tag{1.4}$$

where ν_{L_R} are the neutrino flavor eigenstates and M is the 3x3 neutrino mass matrix.

Majorana mass. A massive Majorana neutrino can be created by modifying the Higgs sector in the Standard Model. An additional singlet, doublet or triplet is added to the original Higgs doublet, although this introduces a new mass scale in the form of the Higgs vacuum expectation value. The mass term in the Lagrangian is:

$$\mathcal{L}_{Majorana} = \frac{1}{2}\overline{\nu}^c_R M \nu_R + h.c. \tag{1.5}$$

In this case neutrinos are their own anti-particles since ν^c_L is a right-handed neutrino. These mass terms violate lepton number conservation by two units and their presence could be indicated by the observation of neutrino double beta decay, nuclear transitions of the type,

$$(Z, A) \rightarrow (Z-2, A) + 2e-, \tag{1.6}$$

which are only possible in the presence of massive Majorana neutrinos. The non-observation of this transition in current experiments sets a limit to the mass of the electron neutrino of $m_{\nu_e} < 0.5$ eV if the ν_e is assumed to be a Majorana particle. If both types of masses, Dirac and Majorana masses exist simultaneously, and if the right handed Majorana mass is very large such as one close to the GUT scale, it is possible to explain very small mass of neutrinos by the so called Seesaw Mechanism [15], [16], [17].

[1] These neutrinos appear in many Grand Unified Theories

1.2.5 Limitations of the Standard Model

Despite the success of the Standard Model, neutrinos show many characteristics that are beyond the standard model of particle physics, there are observations and phenomena that it does not describe. The model does not describe gravity. There are several independent pieces of evidence for dark matter, which is necessary to account for the observed rotation of galaxies. The Standard Model does not include any particle that has the properties consistent with dark matter [28]. Additionally, observations have found that the expansion of the universe appears to be accelerating, the hypothetical cause of which we refer to as dark energy [29]. The Standard Model does not predict a dark energy mechanism. Last, the Standard Model does not describe the origin of neutrino mass, why particles have a particular mass, the cause of CP violation, or why there are three generations of particles.

1.3 NEUTRINO OSCILLATIONS

One of the strangest aspects of neutrinos is that they do not pick just one flavor and stick to it. They oscillate between all three flavors. This phenomenon is known as Neutrino oscillation, a phenomenon in which neutrinos of one flavor are later measured in another flavor, is not included in the Standard Model. Neutrino flavor eigenstates are not the same as the neutrino mass eigenstates. A consequence of this is that as neutrinos propagate, the superposition of mass eigenstates that compose a flavor eigenstate has a time dependent interference pattern that leads to a varying probability that a particular flavor eigenstate will be observed. This mixing is the oscillation.

A superposition of at least three mass eigenstates is requiered to describe the mixing. However, there is evidence for mixing involving one or more sterile neutrinos from the Liquid Scintillator Neutrino Detector (LSND) [30] and MiniBooNE experiments [32]. Sterile refers to the lack of coupling by any Standard Model interaction. Only the three flavor eigenstates are needed to be considered in the description of neutrino oscillation from studies of Z decays at LEP [6]. LEP established that there are no more than three weakly coupling neutrinos with less than half the mass of the Z boson. Flavored neutrinos heavier than the Z boson mass are disfavored by cosmology [6].

The Pontecorvo-Maki-Nakagawa-Sakata (PMNS) matrix [34] details the three flavored eigenstates in terms of a superposition of three mass eigenstates in Equation 1.8. A commonly used form of this matrix for three generations is

$$\begin{pmatrix} c_{12}c_{13} & s_{12}c_{13} & s_{13}e^{-i\delta} \\ -s_{12}c_{23} - c_{12}s_{23}s_{13}e^{i\delta} & c_{12}c_{23} - s_{12}s_{23}s_{13}e^{i\delta} & s_{23}c_{13} \\ s_{12}s_{23} - c_{13}c_{23}s_{13}e^{i\delta} & -c_{12}s_{23} - s_{12}c_{23}s_{13}e^{i\delta} & c_{23}c_{13} \end{pmatrix}, \tag{1.7}$$

with $s_{ij} = \sin\theta_{ij}$, $c_{ij} = \cos\theta_{ij}$ and $\theta_{ij} = \theta_{12}$, θ_{23}, or θ_{13}. These are the neutrino mixing angles that determine the combination of mass eigenstates needed to make a neutrino flavor eigenstate. The term δ is the CP violating phase. The PMNS matrix is generally multiplied by a diagonal matrix containing two Majorana phases, but this matrix is not shown here. These phases could be present if neutrinos are Majorana particles. The Majorana phases cannot affect neutrino oscillation, although they can have an impact on lepton number conservation [35].

The CP violating phase is of great interest. CP violation is the only known asymmetry between matter and anti-matter. This asymmetry is suspected to be the cause of the matter-anti-matter asymmetry we find in the universe. Currently, CP violation has only been observed in the quark sector, but quantitately is too small to give rise to the present imbalance. CP violation in the neutrino sector could be the source of this imbalance, a phenomenon which is refered to as leptogenesis [25].

Given the PMNS matrix, it is possible to construct neutrino flavor eigenstates from the neutrino mass eigenstates

$$\nu_l = \sum_{i=1,2,3} U_{li}\nu_i, l \in e, \mu, \tau, \tag{1.8}$$

where the term U_{li} is the PMNS matrix described in Equation 1.7, ν_i is a neutrino mass eigenstate, and ν_l is a neutrino flavor eigenstate. This, however, is not sufficient to describe neutrino oscillation. Neutrino oscillation is dependent upon several other terms. The probability of oscillation of one type of neutrino to another assuming oscillation between only two flavors is given by [36]

$$P(\nu_\alpha \to \nu_\beta) = \sin^2(2\theta)\sin^2\left(\frac{1.267\Delta m^2_{ij}(eV^2)L(km)}{E(GeV)}\right), \tag{1.9}$$

where ν_α and ν_β are neutrino flavor eigenstates. The term θ is the relevant mixing angle that characterizes the two neutrino oscillation model. The value L is the pathlength of the neutrino in

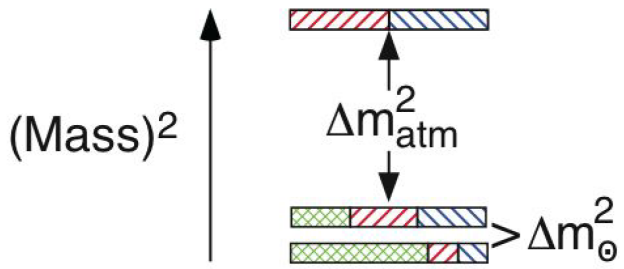

Figure 1.1: Flavor composition of the neutrino mass eigenstates ordered in the normal hierachy. In this depiction, the heaviest eigenstate is ν_3, the second heaviest is ν_2 and the lightest is ν_1. Flavor composition is depicted for each neutrino mass-eigenstate with the ν_e component as cross-hatched lines (green), the ν_μ component as right-leaning lines (red), and the ν_τ component as left-leaning lines (blue). Due to results from Daya Bay [43] and RENO [44], we now know that ν_3 has a small ν_e component.

kilometers, E is the energy of the neutrino in units of GeV, and Δm^2_{ij} is the difference of the square of the two neutrino mass eigenstates, or $m^2_i - m^2_j$, being considered in the oscillation model. Although three neutrino mixing is slightly more complicated than the model above, the oscillations are depenent upon the same general quantities. Oscillations depend upon the ratio $\frac{L}{E}$, which experimenters can control, the term Δm^2_{ij}, and the neutrino mixing angles θ_{12}, θ_{23}, and θ_{13}. The CP violating phase should also be observable in certain types of oscillation. Values of the $\sin^2 2\theta_{ij}$ for each mixing angle along with the values of Δm^2_{ij} are given in Table 1.5. Note that for two of the mass splitting terms, Δm^2_{13} and Δm^2_{23}, the sign of these are not known. Specifically, it is not known whether ν_3 is the lightest or heaviest neutrino mass eigenstate. Solar neutrino observations establish that the ν_2 eigenstate is heavier than ν_1 eigenstate [6]. The scenario where ν_3 is the lightest neutrino mass eigenstate is referred to as an inverted neutrino mass hierarchy [6]. Figure 1.1 depicts the neutrino mass eigenstates and their relative flavor composition.

The first evidence for neutrino oscillation came from the Homestake Experiment, which found roughly a third fewer neutrinos generated by the sun (solar neutrinos) than predicted given the rate of fusion reactions [37]. Super Kamiokande measured neutrino oscillation in neutrinos generated from cosmic ray interactions in the atmosphere (atmospheric neutrinos) [38]. The Super Kamiokande results were verified by two accelerator based experiments, KEK to Kamioka (K2K) [39] and Main Injector Neutrino Oscillation Search (MINOS) [40]. Data from the Sudbury

Parameter	Value
$\sin^2 2\theta_{12}$	$0.857^{+0.023}_{-0.025}$
$\sin^2 2\theta_{23}$	> 0.95 (90% confidence)
$\sin^2 2\theta_{13}$	0.098 ± 0.013
Δm^2_{12}	$7.5^{+0.19}_{-0.20} \times 10^{-5} eV^2$
$\lvert\Delta m^2_{23}\rvert$	$2.32^{+0.12}_{-0.08} \times 10^{-3} eV^2$
$\lvert\Delta m^2_{13}\rvert$	$2.32^{+0.12}_{-0.08} \times 10^{-3} eV^2$
δ	Unknown

Table 1.5: The current best measurements of different parameters that affect neutrino oscillation based on recent PDG values which includes data from RENO and Daya Bay. The CP violating phase δ has not been measured. Note that the values of Δm^2_{13} and Δm^2_{23} cannot be distinguished at this time nor is it known whether these particular parameters are positive or negative [6].

Neutrino Observatory (SNO) helped confirm that neutrino mixing is the explantion for the solar neutrino deficit [41]. Kamioka Liquid Scintillator Antineutrino Detector (KamLAND) further bolstered the three neutrino mixing model by observing neutrino oscillations in a similar regime as solar neutrinos, but using reactor anti-neutrinos [42]. We know the value of θ_{13} from recent measurements by the Daya Bay [43] and RENO [44] experiments. For such accelerator based neutrino experiments, baselines and the corresponding neutrino energies require operating in the few GeV region. In this region, errors on neutrino cross-sections are large and sometimes contradictory and nuclear effects important. This has motivated the study of such topics by oscillation experiments and dedicated experiments such as MINERνA.

1.4 NEUTRINO SCATTERING

The dimensionful measure of probability known as cross-section is the most common quantity of interest in particle physics. Neutrinos interact only via weakly force.

Neutrino scattering is particularly challenging to measure because primarily the incoming energy of ν_μ or $\overline{\nu}_\mu$ is unknown so neutrino physicist have to rely on the measurements of the final state. Within any $\overline{\nu}_\mu$- nucleus scattering, any given final state is accessible by many different initial states.

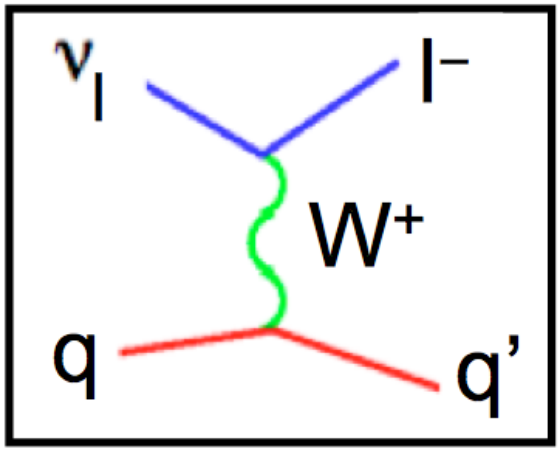

Figure 1.2: Charge Current neutrino interaction with a charged lepton with matching lepton number as a final state

There are two types of interactions, the first one is Charge Current (CC) (1.2) where a neutrino comes in and a charged lepton gets out, the flavor of the outgoing leptons "tags" the flavor of the incoming neutrino, also the charge of the outgoing lepton determines wether it is a neutrino or antineutrino.

The second type of interaction is Neutral Current, observed for the first time in 1972. It this case neutrino come in and interact with a nucleus or atomic electron and neutrino come out as final state particle (1.3).

A general strategy to compute cross-sections in interactions between neutrinos and hadrons is described as following: For two body elastic scattering, the differential cross-section can be calculated using the Feynman rules like:

$$\mathrm{d}\sigma = |\mathcal{M}|^2 \frac{(2\pi)^4}{4\sqrt{\mathrm{p}_1 \cdot \mathrm{p}_2 - \mathrm{m}_1\mathrm{m}_2}} \delta^{(4)}(\mathrm{p}_3 + \mathrm{p}_4 - \mathrm{p}_1 - \mathrm{p}_2) \frac{\mathrm{d}^3\mathrm{p}_3}{(2\pi)^3 2\mathrm{E}_3} \frac{\mathrm{d}^3\mathrm{p}_4}{(2\pi)^3 2\mathrm{E}_4} \,, \tag{1.10}$$

where $\mathcal{M}$: matrix amplitude which is determined by the particulars of the interaction. This matrix amplitude depend upon the particles involved, how they interact, and whether there are several ways this final state can be achieved.

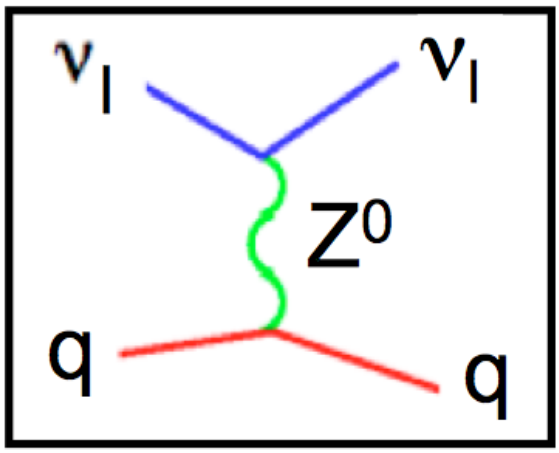

Figure 1.3: A neutral current interaction where the final state lepton has the same lepton number as the incoming neutrino and it is mediated by Z

By assuming the natural Heaviside Lorentz units where c = $\hbar$ = 1. Below follows a derivation by [52]. For point-like particles, this amplitude can be calculated analytically. For instance, for a muon neutrino scattering off of an electron via W exchange ($\nu_\mu + e^- \rightarrow \mu^- + \nu_e$) like in Figure 1.4, we find the matrix element to be:

$$\mathcal{M} = \frac{g_W^2}{8}(\bar{u}(3)\gamma^\mu(1-\gamma^5)u(1))\frac{-i(g_{\mu\nu} - \frac{q_\mu q_\nu}{M_W^2})}{q^2 - M_W^2}(\bar{u}(4)\gamma^\nu(1-\gamma^5)u(2)) \; . \tag{1.11}$$

Taking the case where $q^2 \ll M_W^2$, averaging over initial spins, and summing over final spins, one finds:

$$\begin{aligned} < |\mathcal{M}|^2 >= \frac{1}{2}\sum_{\text{spins}} |\mathcal{M}|^2 = \left(\frac{g_W^2}{8M_W^2}\right)^2 \text{Tr}[\gamma^\mu(1-\gamma^5)(\not{p}_1 + m_e)\gamma^\nu(1-\gamma^5)\ \not{p}_3] \\ \times \text{Tr}[\gamma_\mu(1-\gamma^5)(\not{p}_2 + m_e)\gamma_\nu(1-\gamma^5)\ \not{p}_4] \; . \end{aligned} \tag{1.12}$$

Using trace theorems, Equation 1.12 reduces to

$$< |\mathcal{M}|^2 >= 2\left(\frac{g_W}{M_W}\right)^4 (p_1 \cdot p_2)(p_3 \cdot p_4). \tag{1.13}$$

Using Equations 1.10 and 1.13, going to the center of mass frame, by considering relativistic energies where $\left(\frac{m_e}{E_\nu}\right)$ is small, it can be obtain that:

$$\frac{d\sigma}{d\Omega} = \frac{1}{2}\left(\frac{g_W^2 E_\nu^*}{4\pi M_W^2}\right)\left(1 - \left(\frac{m_\mu}{2E_\nu^*}\right)^2\right)^2 , \tag{1.14}$$

where neglecting the mass of the electron, $E_\nu^* = \frac{E_\nu}{2}$ with E_ν the energy of the incident muon neutrino assuming the electron has negligible momentum.

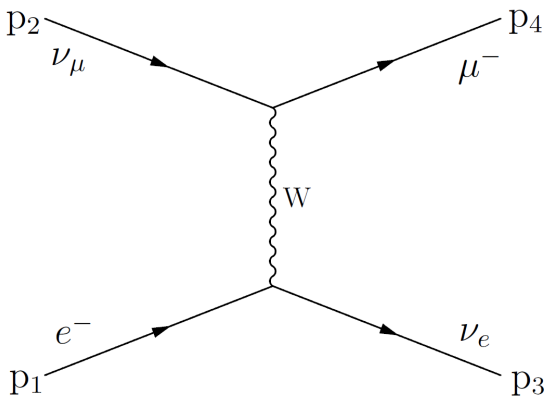

Figure 1.4: Feynman diagram of $\nu_\mu + e^- \rightarrow \mu^- + \nu_e$.

For a neutrino scattering off of a proton or neutron, there is no entirely analytical way to find the matrix amplitude $\mathcal{M}$ due to the structure of a nucleon nature.

$$W^{\mu\nu} = -W_1 g^{\mu\nu} + \frac{W_2}{M_p^2} p^\mu p^\nu + \frac{W_4}{M_p^2} q^\mu q^\nu + \frac{W_5}{M_p^2} + \frac{W_5}{M_p^2}(p^\mu p^\nu + q^\mu p^\nu), \tag{1.15}$$

where M_p is the mass of the proton and the terms W_1, W_2, W_3, W_4, and W_5 are form factors. In this formalism, the anti-symmetric $(p^\mu p^\nu - q^\mu p^\nu)$ tensor is omitted since it cannot contribute to the cross-section due to the Pauli exclusion principle. It is left to experiments to find the form factors, which need not be constants. This is the general strategy used to calculate cross-sections in interactions between neutrinos and hadrons.

This thesis presents an analysis of charge current cross-section where the neutral current considered as background is negligible so a description of charge current interactions will be predominantly described in this chapter. A summary of neutrino cross-sections across energy scales

have been summarized at (Neutrino Cross-section from eV to EeV paper here). The formalism of neutrino interactions is described by using the simplest neutrino electron scattering case and by shifting into different range of neutrino energies. Different neutrino sources determine the range of energies and the description of the nuclear and hadronic effect is also energy dependent as it is shown on Figure (1.5)

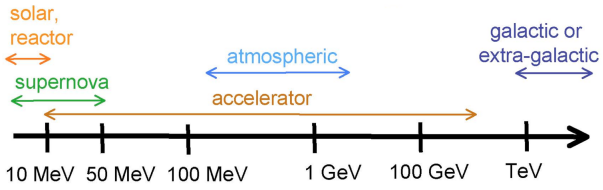

Figure 1.5: Different neutrino sources and range of energies

For neutrino-nucleon scattering in the few GeV range, there are three dominant interactions channels.

Elastic and quasielastic scattering Neutrinos scatters off an entire nucleon liberating a nucleon (or multiple nucleons) from the target. In the case of charged current neutrino scattering, this process is called as quasielastic scattering and for neutral-current scattering this is traditionally referred to as elastic scattering.

Resonance production Neutrinos can excite the target nucleon to a resonance state. The resulting baryonic resonance decays to a variety of possible mesonic final states producing combinations of nucleons and mesons.

Deep inelastic scattering Given enough energy, the neutrino can resolve the individual quark constituents of the nucleon. The results is any number of hadronic final state particles. Often that hadronic system is composed by many pions. The final state may include particles of neutrino interactions from the emission of nucleons to more complex final states including pions, kaons, and collections of mesons.

1.4.1 Inclusive scattering

Many experiments have measured total cross-section for neutrino and antineutrino and scattering results on both charged current (CC) and neutral current (NC) neutrino channels have been col-

lected over many decades using a variety of targets, analysis techniques, and detector technologies (PDG). A summary for world data measurements cross-section using antineutrino can be seen at the figure (1.6)

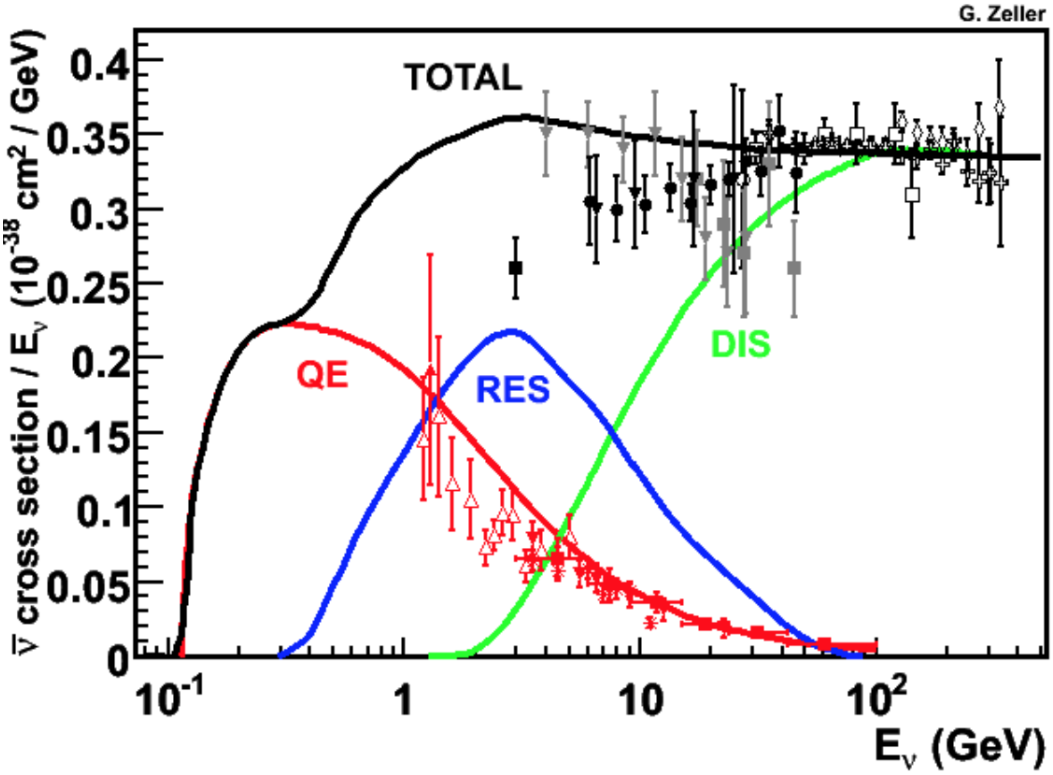

Figure 1.6: The total cross-section are in black, Red shows the quasi elastic contribution that still need data especially at low energy. Blue shows nucleons resonances and pions, green is the DIS prediction without any data measurement available

The neutrino interactions can be described as following for charge current interactions. For neutrino $\nu_\mu + \mathrm{N} \rightarrow \mu^- + \mathrm{X}$ and for antineutrino $\bar{\nu}_\mu + \mathrm{N} \rightarrow \mu^+ + \mathrm{X}$

where N is the target nucleon and X is the hadron final state (see figure 1.7). The differential cross section for neutrino scattering in the center of mass frame of the nucleon is given by:

$$d\sigma = \frac{|M|^2}{4(M_N)|\overrightarrow{k}|} d\phi^{n+1}(k, p; k', p_1, .., p_n) \tag{1.16}$$

$$d\sigma = \frac{|M|^2}{8(2\pi)^3 M_N |\overrightarrow{k}|} \frac{d^3k'}{\epsilon'} d\phi^n \tag{1.17}$$

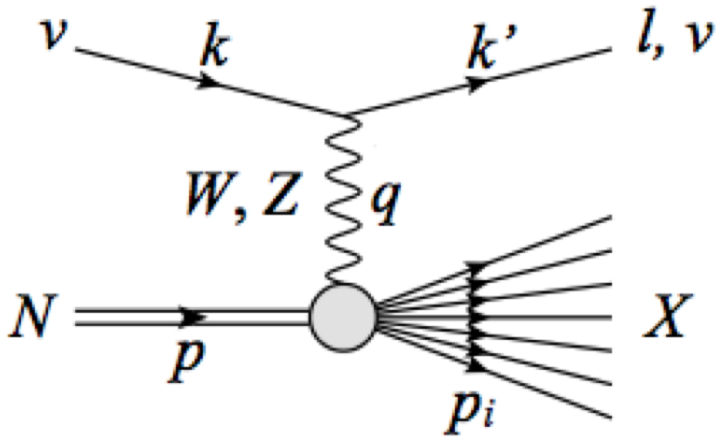

Figure 1.7: Variable definition for the Charged Current Inclusive channel.

$$\frac{d^2\sigma}{d\epsilon' d\Omega} = \frac{1}{2\pi^2}\frac{|M|^2}{32 M_N \pi}\frac{|\overrightarrow{k'}|}{|\overrightarrow{k}|}d\phi^n \tag{1.18}$$

Where:

- Neutrino is massless. The neutrino and charged lepton four momentum given by $k = (E_\nu, 0, 0, E_\nu)$, $k' = (\epsilon', \overrightarrow{k'})$
- The four momentum transer $q = k - k'$ is the difference of the charged lepton with neutrino four-momentum.
- $d^3k' = |\overrightarrow{k'}|^2 d|\overrightarrow{k'}|d\omega$, where ω is the solid angle ($d\omega = d(cos\theta)d\phi$).
- $|\overrightarrow{k'}|d|\overrightarrow{k'}| = \epsilon' d\epsilon'$
- We used the definition of the n-body phase space $d\phi^n \equiv (2\pi)^4\delta^4(\sum_i p_i - p - q)\coprod_{i=1}^{n}\frac{d^3p_i}{2E_i(2\pi)^3}$

So to calculate the invariant amplitude, M_{CC} for a charged current interaction:

$$M_{CC} = \left(\frac{g}{2\sqrt{2}}\right)^2 \bar{l}(k')\gamma_\alpha(1-\gamma_5)\nu(k)\frac{-i(g^{\alpha\beta} - q^\alpha q^\beta/M_W^2)}{q^2 - M_W^2}\langle X(p_1,..,p_n)|J_\beta^{CC}|N(p)\rangle \tag{1.19}$$

where $l(k^{'})$ and $\nu(k)$ are the lepton and neutrino spinors. Assuming low momentum transfer ($|q^2| << M_W$) the propagator is:

$$\frac{-ig^2(g^{\alpha\beta} - q^{\alpha}q^{\beta}/M_W^2)}{8(q^2 - M_W^2)} \approx -ig^{\alpha\beta}\frac{G_F}{\sqrt{(2)}} \tag{1.20}$$

Replacing in equation 1.19, one finds:

$$M_{CC} = \frac{G_F}{\sqrt{2}}\bar{l}(k^{'})\gamma_{\alpha}(1-\gamma_5)\nu(k)\langle X|J^{\alpha}_{CC}|N\rangle \tag{1.21}$$

then the spin-average squared amplitude is:

$$|\overline{M_{CC}}|^2 = \frac{G_F^2}{2}\Big(\sum_{s\nu}\sum_{s\mu}\big([\bar{l}\gamma_{\alpha}(1-\gamma_5)\nu][\bar{l}\gamma_{\beta}(1-\gamma_5)\nu]^{\dagger}\big)\frac{1}{4}\sum_{s_N}\sum_{s_X}\langle X|J^{\alpha}|N\rangle\langle X|J^{\beta}|N\rangle^{\dagger}\Big) \tag{1.22}$$

Where the factor 1/4 corresponds to $\frac{1}{(2s_{\nu}+1)(2s_N+1)}$ with $s_{\nu}, s_N = 1/2$ are the neutrino and nucleon spin values. Simplifying the leptonic term:

$$\sum_{s\nu}\sum_{s\mu}\big([\bar{l}\gamma_{\alpha}(1-\gamma_5)\nu][\bar{l}\gamma_{\beta}(1-\gamma_5)\nu]^{\dagger}\big) = Tr\big([\bar{l}\gamma_{\alpha}(1-\gamma_5)\nu][\bar{\nu}\gamma_{\beta}(1-\gamma_5)l]\big) \tag{1.23}$$

$$= 8[k^{'}_{\alpha}k_{\beta} + k^{'}_{\alpha}k^{'}_{\beta} - g_{\alpha\beta}k\cdot k^{'} + \epsilon_{\alpha\beta\rho\sigma}k^{\rho}k^{'\sigma}] = 8L_{\alpha\beta} \tag{1.24}$$

where the leptonic tensor $L_{\alpha\beta}$ is defined as in [13]. Defining, in addition, a hadronic tensor $W^{\alpha\beta}$, allow us to express equation 2.24 as the multiplication of the leptonic tensor and the hadronic tensor defined in [13]

$$W^{\alpha\beta} = \frac{1}{2M_N}\sum_X \frac{(2\pi)^4\delta^4(P_X - p_N - q)}{2\pi}\langle X|J^{\alpha}|N\rangle^{\dagger}\langle X|J^{\beta}|N\rangle \tag{1.25}$$

$$W^{\alpha\beta} = \frac{1}{2M_N}\sum_X (2\pi)^3\delta^4(P_X - p_N - q)\langle X|J^{\alpha}|N\rangle^{\dagger}\langle X|J^{\beta}|N\rangle \tag{1.26}$$

where the sum includes the sum over the final states as well as the average over the initial spins. The integration is over $\frac{dp_i^3}{2E_i(2\pi)^3}$, and $P_X = \sum_i p_i$ is the total four momentum of the hadronic final state. With the definitions given in equations 1.24 and 1.26 used together with equation 1.18, we obtain the general expresion of the differential cross section:

$$\frac{d^2\sigma}{d\epsilon^{'}d\Omega} = \frac{G_F^2}{4\pi^2}\frac{|\overrightarrow{k^{'}}|}{|\overrightarrow{k}|}L_{\alpha\beta}W^{\alpha\beta} \tag{1.27}$$

The expression for neutral current M_{NC} can be obtained by changing $g \rightarrow \bar{g} = \frac{g}{cos\theta_W}$, $M_W \rightarrow M_Z$,$\bar{l} \rightarrow \bar{\nu}$ and $J_{CC} \rightarrow J_{NC}$ in equations 1.19, 1.20 and 1.21. From equations 1.24 and 1.26 can be noted that the leptonic tensor is exactly calculable while the hadronic tensor is not and depends on the energy transferred. At lower energies, where the neutrinos interact only with bound nucleons or the entire nucleus, strong interactions prevent the hadronic current from being exactly calculable. At low neutrino energies, the most common neutrino interaction energies are those that minimally affect the interaction target. In the case of the charged current interaction this implies the change of electric charge in the baryon target: this interaction is called quasi-elastic interaction(see section 2.8.5). If the $W^{\pm}$ transfers enough momentum, so that the target gets a resonance state, the decay of the resonance will tipically produce a nucleon and a pion (see section 2.8.2).
At low energies, the neutrino interacts with bound nucleons. Hence, any interaction with a bound nucleon will affect the other nucleons in the nucleus. Therefore, nuclear effect has to be taken into account. In the following, we study first the simple neutrino interaction with a free nucleon (section 2.8.2 and section 2.9.5). In section 2.8.3 we study the particular case of neutrinos interacting with the entire nucleus producing coherently a pion without changing the nucleus. At higher energies many mesons and baryons can be produced. This case is called deep inelastic scattering (see section 2.8.4). Figure 1.8 shows the actual knowledge of the total neutrino cross sections for low energies.

1.4.2 Quasielastic scattering

For neutrino energies less than $\sim$ 2 GeV, neutrino-nucleon interactions are predominantly quasielastic (QE). In a charged current neutrino QE interaction, the target neutron is converted to a proton. In the case of an antineutrino interaction, the target proton is converted to a neutron,

$$\nu n \rightarrow \mu^{-} p, \qquad \bar{\nu} p \rightarrow \mu^{+} n \tag{1.28}$$

The most used theoretical description of this proccess is given in a review on neutrino interactions made by Llewellyn Smith [53] in 1972. Where the author uses the standard theory of weak interactions considering the neutrino scattering off free nucleons that are not necessarely point particles.

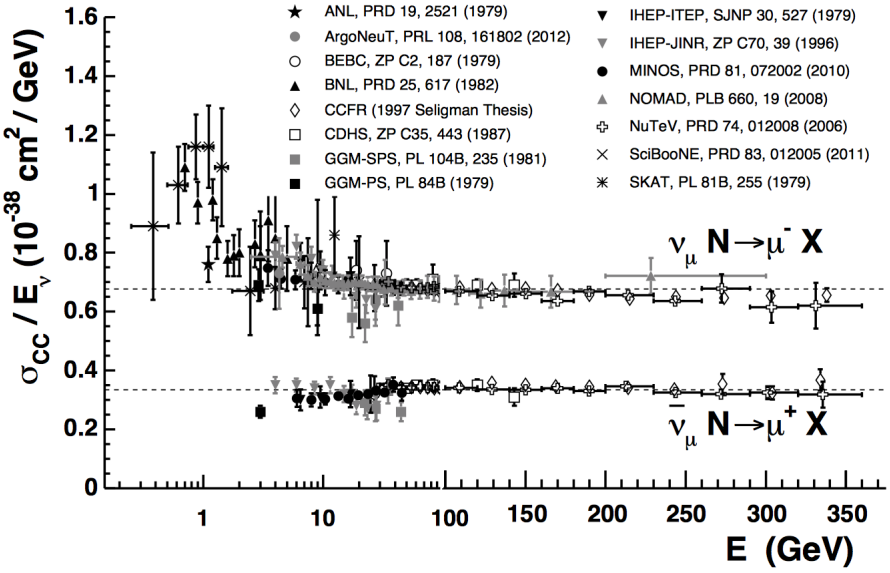

Figure 1.8: Figure from the PDG showing the measurements of ν_μ and $\overline{\nu}_\mu$ CC inclusive scattering cross sections divided by neutrino energy as a function of neutrino energy. Note the transition between logarithmic and linear scales occurring at 100 GeV. Neutrino-nucleon cross sections are typically twice as large as the corresponding antineutrino cross sections, though this difference can be larger at lower energies. NC cross sections (not shown) are generally smaller (but non-negligible) compared to their CC counterparts.

All experiments rely heavily on this formalism and according to it, the quasielastic differential cross section can be expressed as

$$\frac{d\sigma}{dQ^2} = \frac{G_f^2 M^2 \cos^2\theta_C}{8\pi E_\nu^2}\left[A(Q^2) \pm \frac{s-u}{M^2}B(Q^2) + \frac{(s-u)^2}{M^4}C(Q^2)\right] \tag{1.29}$$

where (-)+ refers to (anti)neutrino scattering, G_F is the Fermi coupling constant, θ_C is the Cabbibo angle, Q^2 is the squared four-momentum transfer ($Q^2 = -q^2 > 0$) from the leptonic to hadronic system, M is the nucleon mass, m is the lepton mass, E_ν is the incident neutrino energy, and $(s-u) = 4ME_\nu - Q^2 - m^2$ is a simple combination of two Mandelstam invariants. The factors $A(Q^2)$, $B(Q^2)$, and $C(Q^2)$ are functions of the Q^2-dependent vector, F_1 and F_2, axial-vector F_A, and pseudoscalar F_P form factors of the nucleon (the form factors describes how different the

nucleon is from a point like particle in an elastic scattering). The explicit dependence is shown in formulae 1.30, 1.31 and 1.32 where the definition $\tau = Q^2/4M^2$ is used.

$$A(Q^2) = \frac{m^2+Q^2}{M^2}\Big[(1+\tau)F_A^2 - (1-\tau)F_1^2 + \tau(1-\tau)F_2^2 + 4\tau F_1^2 F_2^2 - \frac{m^2}{4M^2}((F_1^2+F_2^2)^2 + (F_A^2+2F_P^2)^2 - 4(1+\tau)F_P^2)\Big] \quad (1.30)$$

$$B(Q^2) = \frac{Q^2}{M^2}F_A(F_1+F_2) \quad (1.31)$$

$$C(Q^2) = \frac{1}{4}(F_A^2 + F_1^2 + \tau F_2^2) \quad (1.32)$$

The vector part of the neutrino cross section, F_1 and F_2, can also be expresed in terms of the electric and magnetic vector form factors, G_E and G_M. Under the conserved vector current (CVC) hypothesis, these electric and magnetic vector form factors are related to the elastic nucleon form factors in electron scattering G_E^n, G_E^p, G_M^n and G_M^p.

$$G_E = G_E^p - G_E^n \quad (1.33)$$

$$G_M = G_M^p - G_M^n \quad (1.34)$$

These form factors have been measured in electron scattering experiments and their data used to parametrize their functional form which are close to a dipole form. One of these parametrizations is called *BBBA05* [12] and is used in neutrino interaction Monte Carlo simulations. Small contributions to the total cross section from the pseudo-scalar form factor F_P is expected for muon neutrino scattering [**?**]. The only remaining unknown in the model is the nucleon axial form factor which can only be measured using neutrinos. It is costumary to assume a dipole form for the axial form factor, equation 1.35, which depends on two empirical parameters: the value of the axial-vector form factor at $Q^2 = 0 \rightarrow g_A = F_A(0) = 1.2694 \pm 0.0028$ and the value of the Axial mass (M_A).

$$F_A(Q^2) = \frac{g_A}{(1+Q^2/M_A^2)^2} \quad (1.35)$$

The main interest in experiments between 1970-1990, was testing the vector-axial vector (V-A) nature of the weak interaction and measuring the axial-vector form factor of the nucleon, topics that were considered particularly important in providing an anchor for the study of NC interactions. By the end of this period, the neutrino QE cross section could be accurately and consistently described by the model assuming a dipole axial-vector form factor with $M_A = 1.026 \pm 0.021\ GeV$ [18]. To complete the description of charged current QE interactions, a model for nucleons in a nucleus is needed. The most common and simplest approach in Monte Carlo simulations used by most experiments is to use the Impulse Approximation (IA), where the nucleus is considered a collection of independent nucleons, and the relativistic Fermi-gas model (RFG) [74]. In this model, nucleons form a Fermi gas with an average fermi momentum and binding energy that were adjusted to reproduce data of electron scattering experiments. For carbon, a binding energy of 34 MeV and fermi momentum of 200 MeV is used. More recent experiments, such as neutrino oscillation experiments, use heavy target such as carbon, oxygen or iron to improve data rates. Measured cross section are 20% higher than the prediction and inconsistencies as function of Q^2 were found (Miniboone, K2K, MINOS [31]). They have also measured values of M_A ~1.2 GeV which differs from the value obtained in the old experiments that used hidrogen or deuterium targets. Figure 1.9 summarizes the existing measurements of ν_μ QE scattering cross sections as a function of neutrino energy. Figure 1.10 shows the status of measurements of the corresponding

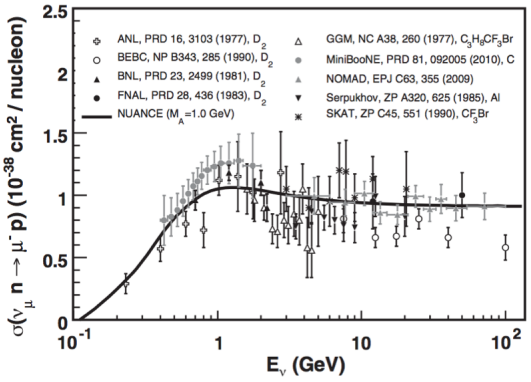

Figure 1.9: Cross section, $\nu_\mu n \rightarrow \mu^- p$, as a function of neutrino energy on a variety of nuclear targets. The free nucleon scattering prediction assuming $M_A = 1.0\ GeV$ is shown for comparison.

antineutrino QE scattering cross section. Recent results from the NOMAD [69] experiment have expanded the reach out to higher neutrino energies, however, there are currently no measurements of the antineutrino QE scattering cross section below 1 GeV.

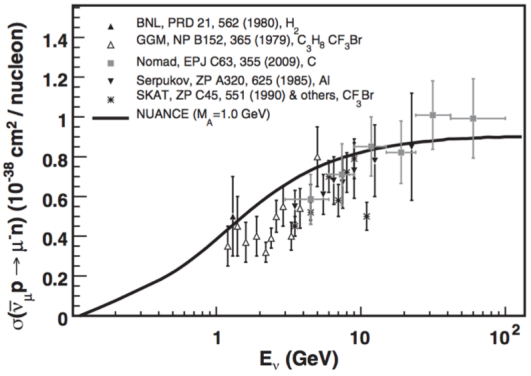

Figure 1.10: Cross section, $\bar{\nu}_\mu p \rightarrow \mu^+ n$, as a function of neutrino energy on a variety of nuclear targets.

1.4.3 Resonant single pion, photon , η and kaon production

The Rein-Sehgal model describes single pion production in the charged and neutral current neutrino scattering. The pions are produced by excitations of 18 resonances [69]. In resonant production the neutrino scatters from a free nucleon. In this section we consider a single nuclear resonance (see figure 1.11) that can be expressed by:

$$\nu + N \rightarrow l + N^* \tag{1.36}$$

$$\nu + N \rightarrow \nu + N^* \tag{1.37}$$

$$N^* \rightarrow N^{'} + \pi \tag{1.38}$$

where N^* denotes one of the 18 nucleon resonances. Because the particle of interest are looking at only single pion production, the kinematical region of this reaction is restricted to the regime of

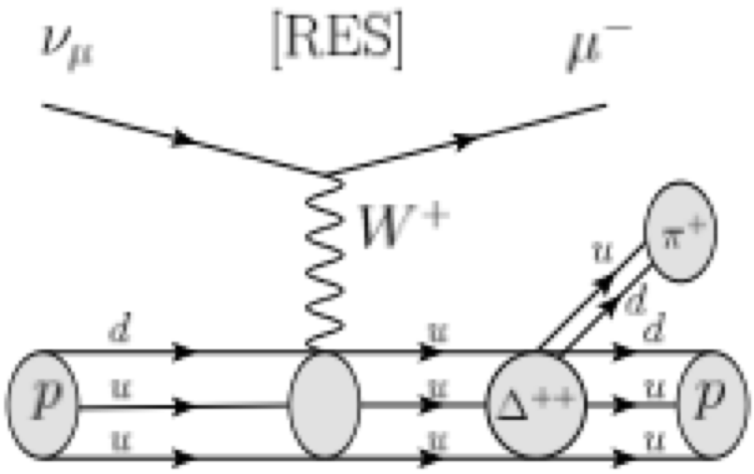

Figure 1.11: Feynman diagram of a single nucleon resonance.

low Q^2 ($Q^2 < 2GeV$). At higher momentum transfer multi-meson resonances and deep inelastic scattering start to be important and are relatively well known (see section 2.8.4). The amplitude of transition is given by:

$$M_{CC} = \frac{G_F cos\theta_C}{\sqrt{(2)}}[\bar{l}\gamma^\alpha(1-\gamma^5)\nu]\langle N^*|J_\alpha|N\rangle \tag{1.39}$$

where J_α is the hadronic current operator containing a vector and an axial vector part. The expression for neutral current can be obtained using $\bar{l} \to \bar{\nu}$ and $G_F cos\theta_C \to G_F$. The cross section for a single resonance with mass M_{N^*} and negligible width is then given by:

$$\frac{d^2\sigma}{dQ^2 dE_q} = \frac{1}{32 M_N E^2}\frac{1}{2}\sum_{spins}|M|^2\delta(W^2 - M_{N^*}^2) \tag{1.40}$$

where M_N is the nucleon mass and W the observed resonance mass. In the cases of non-negligible width, the delta function is replaced by a Breit-Wigner factor:

$$\delta(W - M_N) \to \frac{1}{2\pi}\frac{\Gamma}{(W - M_{N^*})^2 + \Gamma^2/4} \tag{1.41}$$

where Γ is the decay width of N^*, and E_q is the energy of the virtual $W^{\pm}$ or Z^0. Since the Rein-Sehgal model provides the amplitudes of neutrino resonance production, it is possible to calculate the cross section of single photon, kaon and η productions. Therefore, the need is to change the decay probabilities of the resonances.

1.4.4 Coherent pion production

In addition to resonance production, neutrinos can also coherently produce single pion final states. In this case, the neutrino coherently scatters from the entire nucleus, transferring negligible energy to the target (A). These low Q^2 interactions produce no nuclear recoil and a distinctly forward-scattered pion, compared to their resonance mediated counterparts. Both CC (see figure 1.12) and NC coherent pion production processes are possible.

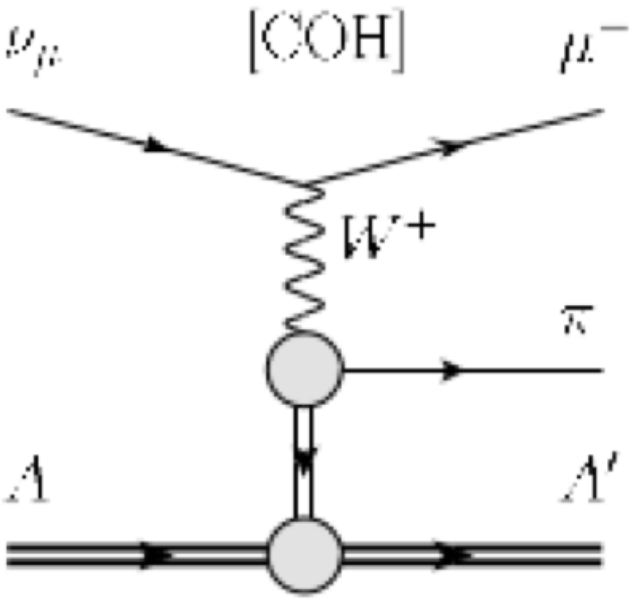

Figure 1.12: Feynman diagram of coherent pion production.

$$\nu_\mu A \rightarrow \nu_\mu A \pi^0, \qquad \bar{\nu}_\mu A \rightarrow \bar{\nu}_\mu A \pi^0 \tag{1.42}$$

$$\nu_\mu A \to \mu^- A \pi^+, \qquad \bar{\nu}_\mu A \to \mu^+ A \pi^- \tag{1.43}$$

The coherent π^0 cross section used in the Rein-Seghal model is based on the Adlers PCAC formula (Partially Conserved Axial-vector Current) [69]. In particular PCAC states that the hadronic axial current $J^a_{\mu 5}$ must satisfy the following continuity equation 1.44.

$$\partial^\mu J^a_{\mu 5} = -f_\pi m_\pi^2 \prod^a \tag{1.44}$$

where $\prod^a$ is the pion field operator, m_π is the pion mass and $f_\pi = 0.93 m_\pi$ is the pion decay constant [69]. the forward scattering configuration, for any elastic neutral current reaction $\nu + N \to \nu + X$, where X denotes an inelastic channel, the cross section is:

$$\left(\frac{d\sigma}{dxdy}\right)_{PCAC} = \frac{G^2 M_N E_\nu}{2\pi^2}(1-y) f_\pi^2 \times \sigma(\pi_0 N \to X)\Big|_{E_\pi = E_y} \tag{1.45}$$

where the muon mass is neglected and the cross section is given in terms of the Bjorken kinematical variables:

$$\nu = \frac{p \cdot q}{M_N}, Q^2 = -(k - k')^2 \to x = \frac{Q^2}{2M_N \nu}, y = \frac{\nu}{E_\nu} \tag{1.46}$$

In order to calculate the charged current cross section $\nu + A \to l^- + X$ it is necessary to take into account the effect of lepton mass that is neglected in equation 1.45. The correction factor of the lepton mass (C) is defined in [69] as:

$$C = \left(1 - \frac{1}{2}\frac{Q^2_{min}}{Q^2 + m_\pi^2}\right)^2 + \frac{1}{4} y \frac{Q^2_{min}(Q^2 - Q^2_{min})}{(Q^2 + m_\pi^2)^2} \tag{1.47}$$

where

$$Q^2_{min} = m_l^2 \frac{y}{1-y} \tag{1.48}$$

The range of the variable Q^2 is :

$$Q^2_{min} \leq Q^2 \leq 2 M_N E y_{max} \tag{1.49}$$

where y lies between $y_{min} = m_\pi / E$ and $y_{max} = 1 - m_l / E$. Thus , the corrected PCAC formula valid for small angle scattering for $\nu + A \to l^- + X$ is [64]:

$$\left(\frac{d\sigma}{dxdy}\right)_{PCAC, m_l \neq 0} = \frac{G^2 M_N E}{\pi^2} f_\pi^2 (1-y) \sigma(\pi^+ + A \to X)\Big|_{E_\pi = E_y} \times C \Theta(Q^2 - Q^2_{min}) \Theta(y - y_{min}) \Theta(y_{max} - y) \tag{1.50}$$

The cross section for $nu + A \rightarrow l^- + A + \pi^+$ is given by:

$$\left(\frac{d\sigma^{\pi^+}}{dxdydt}\right) = \left(\frac{d\sigma^{\pi^0}}{dxdydt}\right) C\Theta(Q^2 - Q^2_{min})\Theta(y - y_{min})\Theta(y_{max} - y) \tag{1.51}$$

The physical interpretation of the correction factor is as follows: when the muon mass is not neglected , the reaction $\nu + A \rightarrow l^- + X$ receives a contribution from the exchanged of a charged pion between the lepton vertex and the hadron vertex. The coupling at the lepton vertex is $f_\pi m_l \bar{l}\gamma_5\nu$ and the amplitude contains the characteristic pion propagator $(Q^2 + m^2_\pi)^{-1}$. This so called pseudo scalar amplitude interferes with the remaining amplitude, which is free of the pion singularity. The two amplitudes interfere destructively and the destructive nature of the interference is visible in the first term of the correction factor. While the cross sections for these processes are predicted to be comparatively small, coherent pion production has been observed across a broad energy range in both NC and CC interactions of neutrinos and antineutrinos. Figure 1.13 shows the measurements of coherent pion production cross sections for a variety of nuclei.

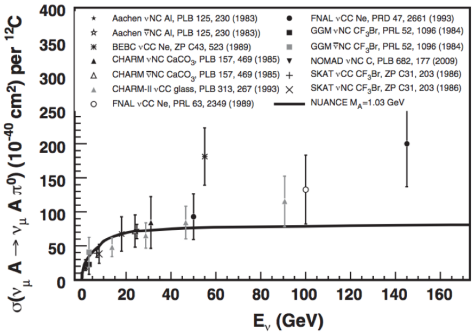

Figure 1.13: Measurements of absolute coherent pion production cross sections from a variety of nuclear targets and samples. Both NC and CC data are displayed on the same plot after rescaling the CC data using the prediction that $\sigma_{NC} = \frac{1}{2}\sigma_{CC}$. In addition, data from various targets have been corrected to carbon cross sections assuming $A^{1/3}$ scaling. Figure taken from reference [58].

1.4.5 Deep Inelastic Scattering (DIS)

Deep inelastic scattering begins to appears at high neutrino energy and is well known at $Q^2 > 2$ GeV^2. DIS can be described by:

$$\nu_l + A \rightarrow l^- + X \tag{1.52}$$

$$\nu_l + A \rightarrow \nu_l + X \tag{1.53}$$

where A is the nucleus. The feynman diagram associated to this procces is shown in figure 1.14. The differential cross section of the process $\nu + A \rightarrow l^- + X$ is given in its general form by equation:

$$\frac{d^2\sigma}{d\Omega d\epsilon} = \frac{G_F^2}{4\pi^2}\frac{|\overrightarrow{k'}|}{|\overrightarrow{k}|}L_{\mu\nu}W^{\mu\nu} \tag{1.54}$$

where $\epsilon^{'}$ is the energy of the outgoing lepton, $W^{\mu\nu}$ can be expressed in its most general way as:

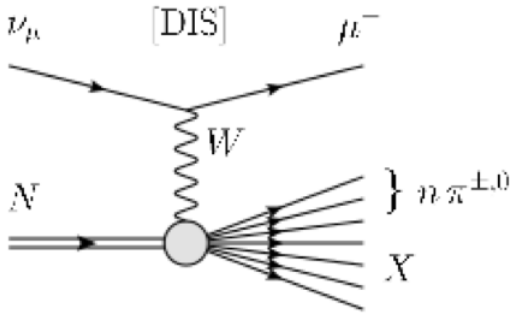

Figure 1.14: Feynman diagram of Deep Inelastic Scattering.

$$W^{\mu\nu} = W_1(-g^{\mu\nu} + \frac{q^\mu q^\nu}{q^2}) + \frac{W_2}{M_N^2}(p^\mu - \frac{p\cdot q}{q^2}p^\mu)(p^\nu - \frac{p\cdot q}{q^2}p^\nu) - W_3\frac{i\epsilon^{\mu\nu\alpha\beta}}{2M_N^2}p_\alpha p_\beta \tag{1.55}$$

where M_N is the mass of the nucleon and the W_i are the hadronic structure functions. In the limit of high Q^2 ($Q^2 >$ 2GeV), they represent the parton distribution functions. This can be shown by changing the Bjorken kinematical variables in the laboratory frame:

$$\nu = \frac{p\cdot q}{M_N}, \quad Q^2 = -(k-k^{'})^2 \rightarrow x = \frac{Q^2}{2M_N(E_\nu - \epsilon^{'})}, \quad y = \frac{(E_\nu) - \epsilon^{'}}{E_\nu} \tag{1.56}$$

For high Q^2, we then have:

$$M_N W_1(Q^2, \nu) \rightarrow F_1(x) \tag{1.57}$$

$$\nu W_2(Q^2, \nu) \rightarrow F_2(x) \tag{1.58}$$

$$\nu W_3(Q^2, \nu) \rightarrow F_3(x) \tag{1.59}$$

where F_1, F_2 and xF_3, are the parton distribution functions. Using Callan-Gross relation, $2xF_1 = F_2$, we obtain:

$$\frac{d^2\sigma}{dxdy} = \frac{G_F^2 M_N E_\nu}{\pi}[(1 - y + \frac{1}{2}y^2 + C_1)F_2(x, q^2) \pm y(1 - y + \frac{1}{2}y^2 + C_2)xF_3(x, q^2)] \tag{1.60}$$

$$C_1 = \frac{1}{2E_\nu}\Big(\frac{yM_l^2}{2M_N x} - xyM_N - \frac{M_l^2}{2E_\nu} - \frac{M_l^2}{2M_N x}\Big) \tag{1.61}$$

$$C_2 = -\frac{M_l^2}{4M_N E_\nu x} \tag{1.62}$$

where M_l is the mass of the lepton and E_ν is the energy of the incoming neutrino.

1.4.6 Nuclear Effects

For the case of charge current quasi elastic the calculation of the cross-section in Equation 1.63 for CCQE scattering is for a free nucleon. But if the scattering is not on hydrogen, that nucleon is contained within a nucleus. The presence of the target nucleon in a nucleus may show several effects such as Pauli blocking, final state interactions, and other potential nuclear effects such as meson exchange current. The cross-section and the final state kinematics will be affected by these nuclear effects.

$$\frac{\mathrm{d}\sigma}{\mathrm{dQ^2}} = \frac{\mathrm{M^2 G^2 \cos^2\theta_c}}{8\pi \mathrm{E_\nu^2}}\left(\mathrm{A(Q^2)} \mp \mathrm{B(Q^2)}\frac{(\mathrm{s-u})}{\mathrm{M^2}} + \frac{\mathrm{C(Q^2)(s-u)^2}}{\mathrm{M^4}}\right) \tag{1.63}$$

where the term $\mp$ is negative for neutrinos and positive for anti-neutrinos, G is the weak coupling constant, M is the mass of the nucleon that the neutrino is scattering from, E_ν is the incident

(anti-)neutrino energy, θ_c is the Cabibbo angle, $(s-u) = 4ME_\nu - Q^2 - m_l^2$, where s and u are Mandelstam variables[1], and Q^2 is the square of the momentum transferred from the neutrino to the nucleon. The terms $A(Q^2)$, $B(Q^2)$, and $C(Q^2)$ are given by Equations 1.64, 1.65, and 1.66 as functions of vector form factors F_V^1 and F_V^2, psuedo-scalar form factor F_P, axial vector form factor F_A, and ξ which is the difference between the anomalous magnetic moment of the proton and neutron. We use Q^2 where $Q^2 = -q^2$.

$$\begin{aligned} A(Q^2) = \frac{(m_l^2+Q^2)}{M^2}[(1+\tau)\,|F_A|^2 - (1-\tau)\,|F_V^1|^2 + \tau\,(1-\tau)\,|F_V^2|^2 \\ +4\tau \mathrm{Re}F_V^{1*}\xi F_V^2 - \frac{m_l^2}{4M^2}\left(|F_V^1+\xi F_V^2|^2 + |F_A+2F_P|^2 - 4(1+\tau)|F_P|^2\right)]. \end{aligned} \tag{1.64}$$

$$B(Q^2) = \frac{Q^2}{M^2}\mathrm{Re}F_A^*\left(F_V^1+\xi F_V^2\right). \tag{1.65}$$

$$C(Q^2) = \frac{1}{4}\left(|F_A|^2 + |F_V^1|^2 + \tau|\xi F_V^2|^2\right). \tag{1.66}$$

In the case of Pauli blocking, an effect relating to the Pauli exclusion principle is active. The nucleons within the nucleus have a distribution of momenta which corresponds to different quantum mechanical states. An interaction will be suppressed in cases where a final state nucleon would be imparted energy that would push it into an already occupied state. This imparts a threshold for scattering based on the energy transfer from the neutrino to the final state hadron, and affects the cross-section for a particular process.

Final state interactions (FSI) involving the final state hadron and the nucleus the interaction is occurring in can also have large effects. This can involve scattering of the final state hadron as it exits the nucleus. This modifies the angle and energy of that final state particle. Something more dramatic can happen, in which FSI can create pions or eject other nucleons. A particular interaction may be quasi-elastic, but may have particles in the final state that are not consistent with CCQE scattering such as pions. This can lead to the loss of signal events if this is not simulated correctly. The converse can happen as well, where a non-CCQE interaction can appear as signal due to FSI. Likely the most common example of this is pion absorption in the nucleus following resonant production. In this case, the only observable final state particles will be a muon and a

nucleon, which will likely appear as a CCQE interaction.

Other nuclear effects may also be at work such as short range correlations [72] and MEC [73]. These effects can modify scattering cross-sections. Short range correlations affect the momentum distribution of a target nucleon, which can counteract Pauli blocking and modify the final state kinematics of the muon as well. Short range correlations can lead to momenta higher than would be predicted by a Relativistic Fermi Gas (RFG) Model [74], which many simulations employ. Since reconstruction of an event often assumes a nucleon is at rest, short range correlations also can cause reconstruction errors or smearing beyond what would be predicted by the RFG. The topics of RFG and MEC are discussed below.

1.4.6.1 The Relativistic Fermi Gas Model A commonly used model of the nucleus is the RFG model. This model involves treating nucleons within a nucleus as a non-interacting Fermi gas. For a Fermi gas in the ground state, particles occupy energy levels ranging from the lowest possible energy up to the Fermi energy. In the RFG model of a nucleus, we consider the maximum momentum, known as the Fermi momentum.

The common way to implement this model in a simulation is a step function where if a final state nucleon's momentum is below the Fermi momentum, the function and consequently the cross-section is zero. A binding energy term, $\mathrm{E_b}$, is also considered. This is the amount of energy required to separate a nucleon from a particular nucleus and affects the final state energy of a nucleon [74].

This model has limitations. Perhaps the largest issue is the assumption that nucleons are non-interacting, which we know to be false. Short range correlations can lead to nucleons having a momentum greater than the Fermi momentum. To accomodate this, some models contain a high side tail for nucleon momentum [75]. Effects such as MEC, which involve the exchange of mesons between nucleons, are suspected to be present and could lead to a higher than otherwise predicted cross-section. Other models of the nucleon behavior within the nucleus do exist, such as spectral functions.

1.4.6.2 Spectral Functions Spectral functions describe the probability of removing a proton or neutron with a particular momentum from a nucleus. A spectral function is assembled by considering nucleons in two different scenarios. The first case involves filling states using the shell model of the nucleus. Most nucleons within a nucleus occupy such a state. The wave functions for nucleons up to the number that are predicted to be in such a state are used to directly calculate this particular component of a spectral function. This component of the spectral function can be modeled as a gaussian distribution, the details of which depend upon the nucleus. A small fraction of nucleons are in a higher energy state due to short range correlations. This component of the structure function is found using the wavefunctions of the correlated pair and maximum and minimum momenta of that pair [72, 76]. This model can be used as an alternative to the RFG model.

1.4.6.3 Meson Exchange Currents MEC is one proposal to explain the enhancement observed in CCQE scattering in certain experiments. An abundance of diagrams can contribute to the MEC process, but in general, a neutrino scatters off of a nucleon undergoing meson exchange with another nucleon. The final states in MEC are fundamentally different from CCQE scattering, but since final state nucleons are not necessarily observed, the process can appear as a CCQE event. For processes that have identical final states, interference can occur between diagrams when calculating a cross-section [1]. That is not applicable in the case of CCQE scattering and MEC. If MEC is present, it would enhance the overall charged current cross-section. Since MiniBooNE is not sensitive to final state nucleons, this has been put forth as a possible explanation for the size of the MiniBooNE CCQE cross-section [73].

Many different models are used to account for the effect of MEC or other similar processes that suspected to occur. One model captures the effect of MEC as an enhancement of the magnetic form factor of the nucleon [77]. This method is attractive due to the simplicity of implementing it, but it lacks details of the final state. Many other more sophisticated models exist [78, 79, 80, 81, 82, 83, 84]. Additional data are needed to verify that MEC or similar processes are present in neutrino-nucleus interactions and to test the various models that now exist.

1.4.7 Neutrino Energies and Target Materials

Modern experiments aims to make precision measurements of neutrino- nucleus interactions for neutrino energies up to a few GeV ([2]). These experiments including MINERνA will measure absolute cross- sections for a variety of inclusive and exclusive final states and for a range of nuclear target materials. Variety of nuclear targets (liquid or Solid), for the case of MINERνA the solid targets are carbon, iron, lead and scintillator and liquid targets are water and helium, argon will be added in the near future with a join collaboration with CAPITAIN Experiment becoming CAPITAIN MINERνA This should create the possibility of unfolding neutrino- nucleon scattering rates from complicated nuclear effects.

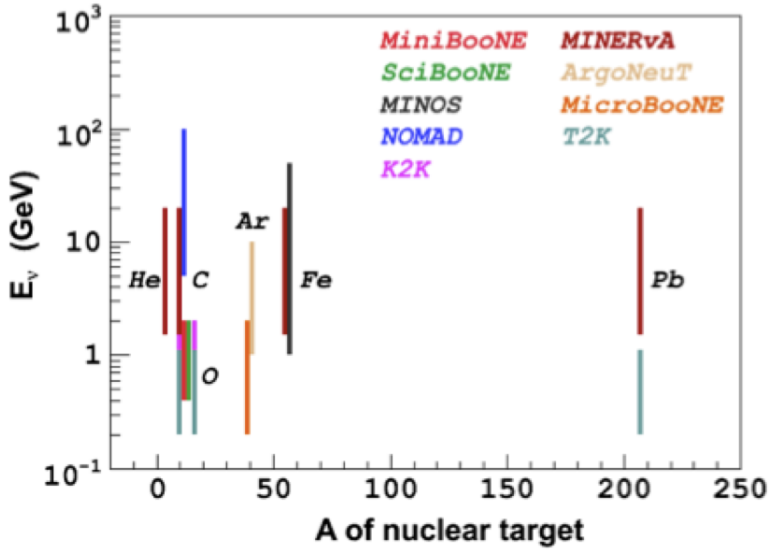

Figure 1.15: Coverage of the current and future neutrino cross-section experiments in this same (E_ν, A) phase space. This figure was borrowed from ([2])

2.0 THE NUMI BEAMLINE

To study neutrinos, at Fermilab, scientist have the NuMI (Neutrinos and the Main Injector) beamline ([50]). ν_μ and $\overline{\nu}_\mu$ are created at a large quantity. It is used by the MINERνA, MINOS, and NOνA [50] experiments as a neutrino source for oscillation and cross section measurements. The process start with a proton beam which accelerated at a certain energy, slam that beam of proton into a graphite target and produce many different kinds of subatomic particles. These subatomic particle decay over a distance and some of those decay produce neutrinos. This chapter describes the design of the NuMI beam, the process to produce neutrino and antineutrino and the measurement of its ν_μ and $\overline{\nu}_\mu$ flux.

2.1 THE PROTON BEAM

The NuMi (Neutrinos at the Main Injector) beamline is a conventional accelerator neutrino source at Fermilab ([50]). The neutrinos and anti-neutrinos that MINERνA measures come from NuMI. NuMI is part of a larger complex at Fermilab that produces beams for a variety of physics experiments as depicted in Figure 2.1.

2.2 ACCELERATING PROTONS

In order to create the beam of proton, a container of hydrogen gas is needed. The hydrogen is ionized to form H^- ions, which are then accelerated to 750 KeV by a Cockcroft-Walton[1] generator. Next, the H^- ions are accelerated to 400 MeV by a series of linear accelerators. The beam then passes through carbon foil, converting the H^- to protons, and the protons are injected into the Booster ring [85].

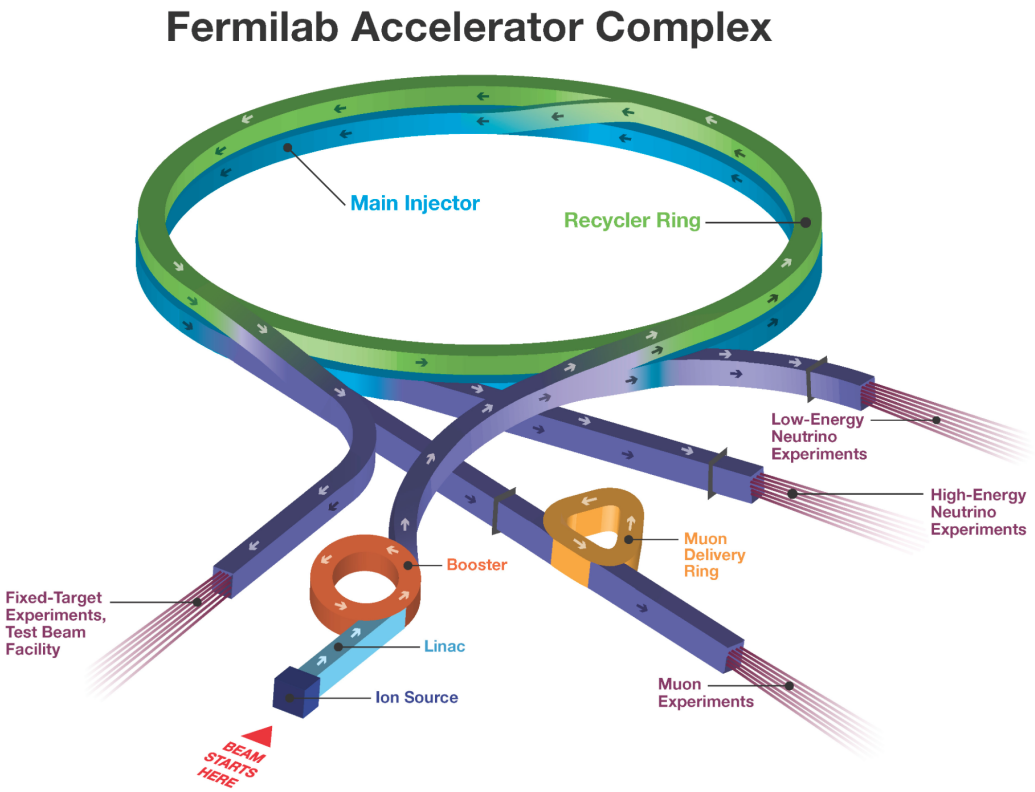

Figure 2.1: An overhead view of the various beam facilities at Fermi National Accelerator Laboratory. The Linac, Booster, and Main Injector accelerate protons which are consumed by the NuMI beam [86].

[1] In 2012, after the data used in this thesis was collected, Fermilab replaced the Cockroft-Walton with a new radio frequency quadrupole accelerator.

The H^- ions are fed to a Linac (LINear ACcelerator) and accelerated to an energy of 116 MeV using a series of drift tubes. A drift tube is an electrically-resonant copper cylinder that creates an alternating electrical field. If injected during the appropriate phase, the H^- ions will be accelerated in the forward direction. After traversing the drift tubes, the ions pass through Side-Coupled Linacs (SCL). SCLs are coupled cavities each powered by a 12 MW Klystron. The sequence of SCLs accelarates the H^- ions to an energy of 401 MeV [87].

The H^- ions are transported to the Booster for injection. The Booster is a 150 meter diameter synchotron. The ions pass through a foil during injection stripping away the electrons and leaving a proton beam. Over multiple circulations within the Booster, protons are accelerated to an energy of 8 GeV [88].

Once protons in the Booster reach 8 GeV in energy, they are ready for transfer to the Main Injector. For the purposes of injecting beam in the Main Injector with minimal losses and damage, a particular batch structure is enforced within the Booster. This structure is visible within the NuMI beamline, as shown in Figure 2.2 [88].

The Main Injector is a synchotron which accelerates protons intended for the NuMI beamline to an energy of 120 GeV [89]. Upon reaching 120 GeV of energy, protons are ready to be transfered to the NuMI beamline. Proton spills can be transfered to the NuMI beamline every 2.06 or 2.20 seconds during this run. Bunches are generally about 10 microseconds in width, which varies slightly depending upon whether the Recycler Accelerator for the Tevatron is running.

2.3 THE NUMI BEAMLINE

The NuMI beamline can be configured to produce muon neutrinos or muon anti-neutrinos. Additionally, the energy spectrum of the resulting neutrinos and anti-neutrinos can be modified by altering certain components of the beam. For this analysis, the Main Injector delivered up to 35×10^{12} protons on target (POT) per spill, which is close to the design maximum of 40×10^{12} POT. Here, POT refers to the number of protons delivered from the Main Injector to the NuMI target. The terms upstream and downstream are defined by the direction of the NuMI beam. Upstream refers to something being closer to the source of the beam and downstream refers to something further

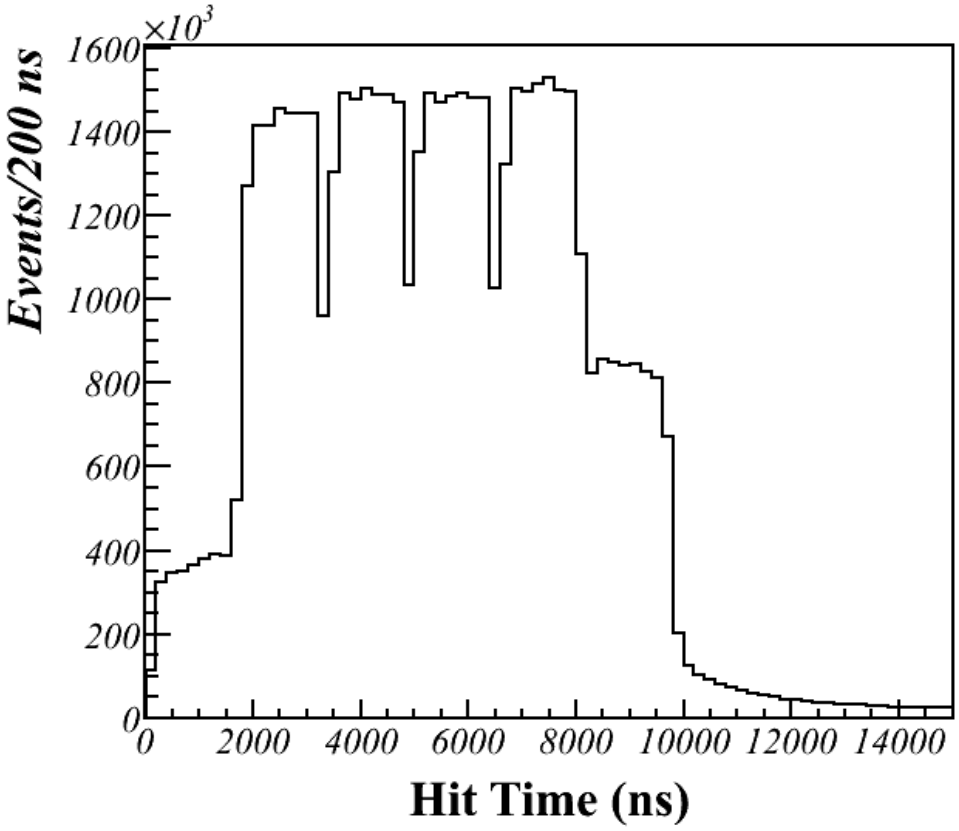

Figure 2.2: Distribution of MINERνA hits demonstrating bunch structure for the NuMI beamline. A portion of the tail in the plot is from particle decays within the detector.

from the source of the beam. A step by step description of this beamline follows.

Protons for the NuMI beamline are extracted from the Main Injector and directed downward at an angle of 58 milliradians. This angle was selected to facilitate MINOS [90], a long baseline neutrino oscillation experiment. This angle is accounted for at the analysis stage and has a minor impact on acceptance.

After protons are injected into the NuMI beam, they pass through a baffle that acts as a collimator before colliding with the NuMI target [91]. The NuMI target is a water cooled graphite (carbon) cylinder roughly two interactions lengths (approximately one meter) long and 6.4 mm in diameter [92]. The proton beam is about 1 mm in diamter [93] when it collides with the NuMI target with a maximum divergence of 60 microradians [94]. Proton interactions with the nuclei of the target create pions and kaons which can subsequently reinteract within the target. The target diameter is thin to minimize this reinteraction. Reinteractions change the resulting spectrum of the pions and kaons. Modeling reinteractions is difficult and is consequently a large source of systematic error.

The resulting spray of pions and kaons as well as any left over protons then travel toward the NuMI horns, which are depicted in Figure 2.3. The NuMI horns are two toroidal electromagnets with parabolic curvature. Together, the two horns act as a lens system. The focusing of the horn system can be modified by changing the current applied to the horns including reversing the polarity of that current. Changing the polarity flips the sign of the magnetic field and consequently changes which type of charge is focused or defocused. The magnitude of the current changes the size of the magnetic field within the horns which determines the focal point of the system. The focal point is also dependent upon the momentum of the pion or kaon.

Pions and kaons with too low of momentum will not be sufficiently focused to contribute to the flux. Since very high energy pions and kaons are over-focused if they pass through the horns, these too will not contribute to the flux. However, some pions and kaons can pass through an aperature in the center of the horns, which we refer to as the ”neck.” This includes very high energy pions and kaons which consequently contribute to a high energy tail in the neutrino and anti-neutrino energy spectrum. The particular spectrum of pions and kaons focused by the horns can also be modified by changing the spacing between the target and the horn system. Last, the spacing between the two horns can be adjusted although in practice this is never varied. If no current is passing through

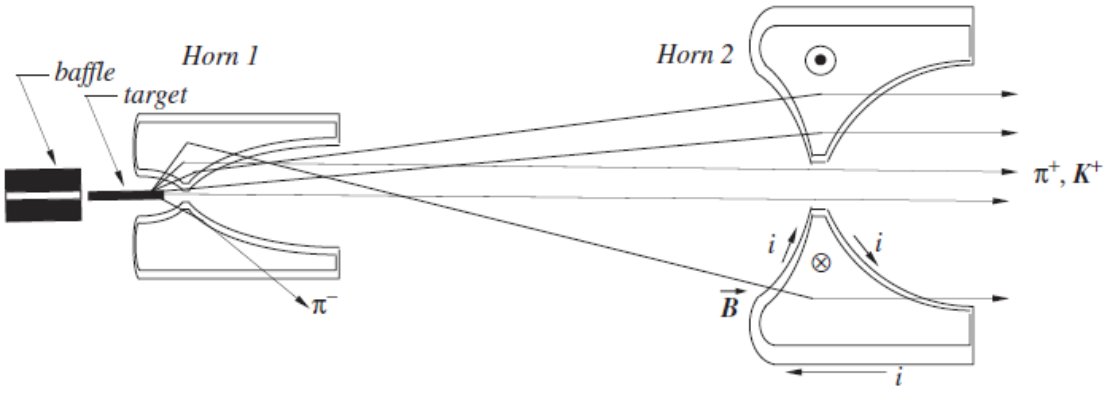

Figure 2.3: A schematic of the two magnetized parabolic NuMI horns used to focus the pions and kaons prior to their decay. Distances in the figure are for illustrative purposes. [95].

the horns, no focusing occurs [95]. An illustration of pions and kaons passing through the horn system is in Figure 2.3.

For this analysis, a horn-target spacing of 10 cm and horn current of -185 kA was used. The 10 cm spacing corresponds to roughly 25 cm of the target lying within the horn system. We refer to this configuration as Reverse Horn Current (RHC) Low Energy (LE) running. Note that there are several configurations that are refered to as LE running. In typical Forward Horn Current (FHC) LE running, accounting for cross-sections, we expect roughly 91.7% ν_μ, 7.0% $\overline{\nu}_\mu$, and 1.3% ν_e and $\overline{\nu}_e$ [40]. The RHC mode, which is ran nominally as an anti-neutrino beam, has siginificant amounts of neutrinos and anti-neutrinos. In the RHC beam, again accounting for cross-sections, we expect 58.1% ν_μ, 39.9% $\overline{\nu}_\mu$, and 2.0% ν_e, and $\overline{\nu}_e$ [40]. The muon neutrinos form a broad high energy tail for the overall RHC spectrum while the muon anti-neutrinos are peaked around an energy of a few GeV.

After passing through the horn system, the pions and kaons, along with any protons left over from the original beam, enter a 675 m decay pipe, which is depicted in Figure 2.4. This pipe is 2 meters in diameter and has been evacuated and then filled with 13.2 PSI of helium. This pressure increases slightly during beam operation due to heating of the helium by particle interactions with the helium [96]. The presence of helium is to minimize pion absorption and pion interactions which would occur more frequently in the presence of air. Most pions and kaons decay to neutrinos and

muons through the following decays modes: $\pi^+ \rightarrow \mu^+ + \nu_\mu$, $\mathrm{K}^+ \rightarrow \mu^+ + \nu_\mu$, $\pi^- \rightarrow \mu^- + \overline{\nu}_\mu$, and $\mathrm{K}^- \rightarrow \mu^- + \overline{\nu}_\mu$. Protons, undecayed pions and kaons, and muons pass through a Hadron Monitor at the end of the decay pipe. The Hadron Montior is an array of small helium ionization chambers which measure the amount of ionization created by charged particles along with the spatial distribution of those particles. This detector is in place to monitor that the beam is functioning properly [97]. These particles then pass into the Hadron Absorber. The Hadron Absorber is a large mass of concrete blocks with enough material to fully stop most hadronic particles in the beam.

Since muons in the few GeV energy range are minimum ionizing particles, most pass through the Hadron Absorber without being stopped. Directly after the Hadron Abosrber is the first of three Muon Monitors. Figure 2.5 illustrates the location of each monitor. These monitors use the same ionization chambers as the Hadron Monitor, but are spread out over a larger area. This is to account for the divergence of the muons as they travel. The two other Muon Monitors are placed within alcoves drilled into the dolomite rock present at that depth. Each of the three Muon Monitors is beam centered. Since muons must pass through increasing amount of rock to reach the two successive Muon Monitors, the energy threshold for a muon increases for each successive monitor. The threshold allows for a measurement of the muon energy spectrum. This information is currently being used to constrain the prediction of the pion and kaon spectrum and consequently the expected neutrino and anti-neutrino energy spectrum. In total, 240 meters of dolomite separate the decay pipe and the Near Detector Hall. This amount of material is sufficient to range out all muons originating from the NuMI beamline. The neutrinos pass through the Hadron Absorber and rock unattenuated to the Near Detector Hall.

The Booster is a synchrotron accelerator with a radius of 75 m. It accelerates the protons to 8 GeV in about 67 ms, requiring $\sim$40,000 laps around the ring. The protons are then injected into another synchrotron, called the Main Injector, that accelerates the protons to 120 GeV. While the Tevatron was operational, the Main Injector also served as a proton source for antiproton production and a storage ring for the antiprotons. It separates the proton beam into six groups called batches. The Tevatron only required one of the six batches; the remaining five were delivered to the NuMI beamline. After the Tevatron was decommissioned, all six batches were used by NuMI.

The protons are extracted to the NuMI target once every 2.2 seconds using a single turn extraction. Each extraction consists of one five or six batch beam spill. A five batch spill generally

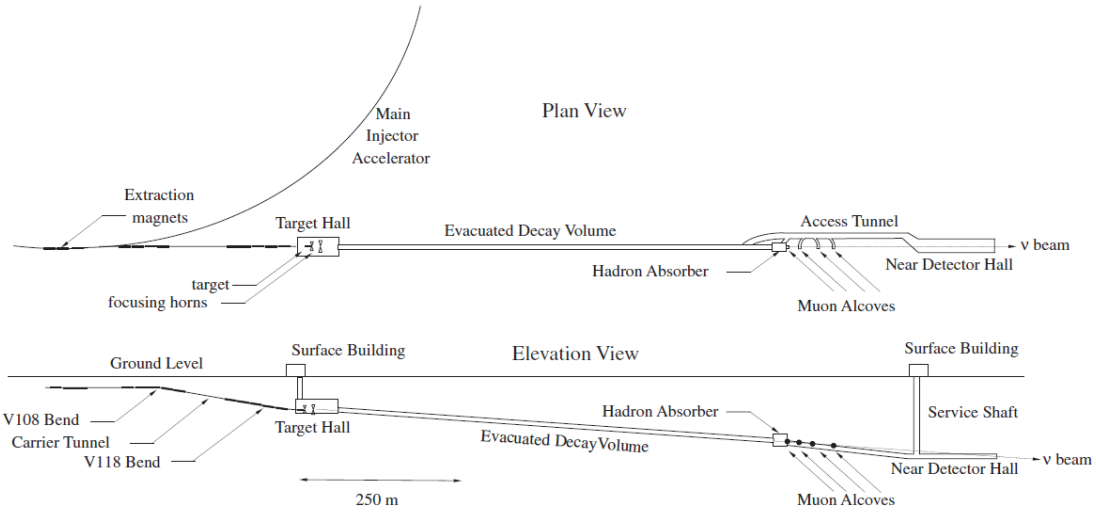

Figure 2.4: An overhead and cut-away view of the NuMI facility. Protons are extracted from the Main Injector and are directed toward a target producing pions and kaons. The pions and kaons are focused by a horn system after which they travel down a decay pipe. These pions and kaons decay overwhelmingly to muons and neutrinos. The Hadron Absorber stops pions, kaons, and protons. The muons and neutrinos then enter dolomite rock that extends for 240 meters. Muons range out within the rock and the neutrinos travel onward toward the Near Detector Hall. [95].

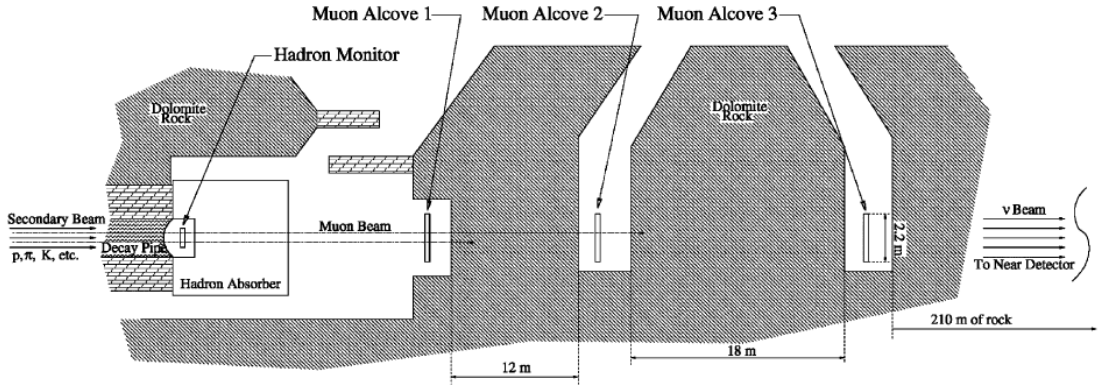

Figure 2.5: Locations of the Hadron Monitor and three Muon Monitors in the NuMI facility [97].

contains $\sim 3.5 \times 10^{13}$ protons and lasts 8.4 μs; a six batch spill is 10 μs and contains $\sim 4.2 \times 10^{13}$ protons. Before colliding with the NuMI target, the proton beam position is focused to a 1 mm profile by a baffle. The proton beam is monitored and its intensity is measured to 2%. The intensity measurement places a direct limit on how well the neutrino flux can be measured.

2.4 NUMI FLUX MEASUREMENT

One of the common notorious components of cross-section that all neutrino experiments shares is the measurement of the neutrino beam flux. The NuMI flux is measured using G4numi, a NuMI-specific implementation of Geant4 9.2.p03 [115], with external data constraints. G4numi contains a description of the NuMI beamline geometry and a map of the magnetic field generated by the focusing horns. Hadron production from 120 GeV p interactions on the graphite target is simulated using the FTFP_BERT model included in Geant4. FTFP_BERT uses the FTFP[31] model to simulate inelastic hadron-nucleus scattering above 4 GeV. In FTFP, QCD strings are formed between partons in the incoming hadron and target nucleus using the FRITIOF[31]model. The strings are hadronized according to the Lund fragmentation model [28] and the excited nucleus is de-excited by G4Precompound. The Bertini intranuclear cascade model[28] simulates interactions below 4 GeV.

The pC interaction products are propagated through the NuMI beamline geometry, subject to the magnetic field produced by the focusing horns, and allowed to reinteract in the beamline material. G4numi also simulates particle decay.

The FTFP_BERT prediction for 120 GeV pC interactions does not compare well with data; see, for example, the comparison of FTFP_BERT to NA49 data [117] in Figure 2.6. The relevant variables in these comparisons are:

- x_F – The Feynman scaling variable, $x_F = 2p_L/\sqrt{s}$, where p_L is the outgoing particle's longitudinal momentum and $\sqrt{s}$ is the total center of mass energy.
- p_T – The transverse momentum of the outgoing particle.
- $f(E, x_F, p_T)$ – The invariant production cross section, $f = Ed^3\sigma/dp^3$.

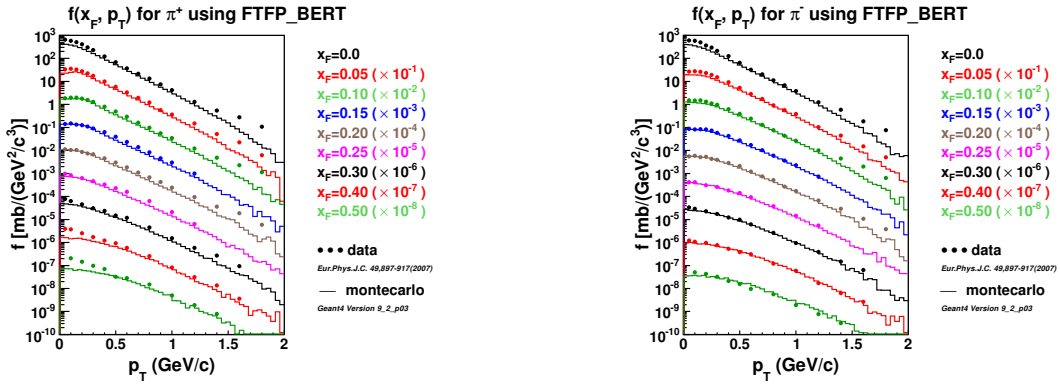

(a) $p\mathrm{C} \to \pi^{+}\mathrm{X}$ (b) $p\mathrm{C} \to \pi^{-}\mathrm{X}$

Figure 2.6: Comparisons of NA49 data and FTFP_BERT simulation of the cross sections for the process $p\mathrm{C} \to \pi^{+}\mathrm{X}$ (left) and $p\mathrm{C} \to \pi^{-}\mathrm{X}$ (right)

For the data analyzed in this thesis, pions focused by the magnetic horns generally fall within the range $p_T = (0.1 - 0.6)$ GeV$/c$ and $x_F = (0.05 - 0.15)$, while the higher momentum unfocused mesons have the kinematic range $p_T = (0 - 0.2)$ GeV$/c$ and $x_F = (0.2 - 0.5)$.

Data agreement is improved by reweighting the FTFP_BERT predictions to match external data from three experiments, summarized in Table 2.1. The weight applied to the simulation for data collected at energy E_{data} is

$$weight = C(E_{data}) \cdot \frac{f(E_{data}, x_F, p_T)_{data}}{f(E_{g4numi}, x_F, p_T)_{g4numi}}, \tag{2.1}$$

where $C(E_{data})$ is derived from an alternate hadron production simulation called FLUKA [**?**] and scales the data to the simulated energy $E_{g4numi} \sim 120GeV$:

$$C(E_{data}) = \frac{f(E_{g4numi}, x_F, p_t)_{fluka}}{f(E_{data}, x_F, p_t)_{fluka}}. \tag{2.2}$$

Simulated events that are not covered by the data in Table 2.1 are not reweighted. The proton production data is used to constrain simulation of the proton beam attenuation in the NuMI target. Figure 2.7 shows the ratio of weighted to unweighted simulation; the weights can be as large as

Table 2.1: A summary of data used to constrain the NuMI flux measurement.

Data	Process	Proton Energy (GeV)	Kinematics
NA49 [117]	$p\mathrm{C} \to \pi^{\pm}\mathrm{X}$	158	$x_F < 0.5$
NA49 [117]	$p\mathrm{C} \to K^{\pm}\mathrm{X}$	158	$x_F < 0.2$
NA49 [117]	$p\mathrm{C} \to p\mathrm{X}$	158	$x_F < 0.95$
MIPP	$p\mathrm{C} \to K^{\pm}\mathrm{X}$	120	$0.2 < x_F < 0.5$
Barton	$p\mathrm{C} \to \pi^{\pm}\mathrm{X}$	100	$x_F > 0.5$

50% at higher E_ν. Figure 2.8 shows the reweighted flux prediction used by the analysis in this thesis.

igure (2.9) shows the possible energy configurations of the NuMI beam: low energy (LE) and medium energy (ME). Different energies are achieved by changing the distance between the target and the second horn in a movement similar to the lenses of an optical system2. Pions and kaons of different momenta are selected and focused in the decay region resulting in different energy spectra.

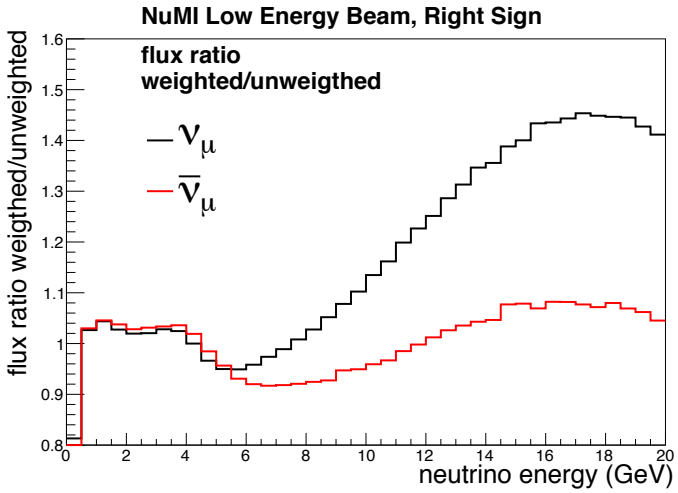

Figure 2.7: The ratio of weighted to unweighted flux as a function of neutrino energy. "Right sign" means that the neutrino is produced from a charged meson that is focused by the focusing horns.

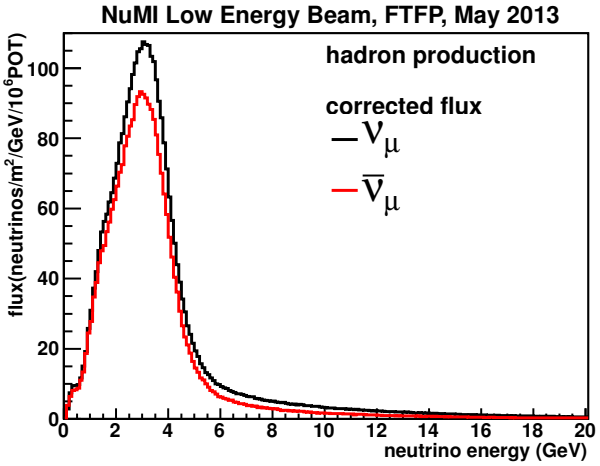

Figure 2.8: Prediction of flux for forward horn focus (black) and reversed horn focus used for this analyst (red)

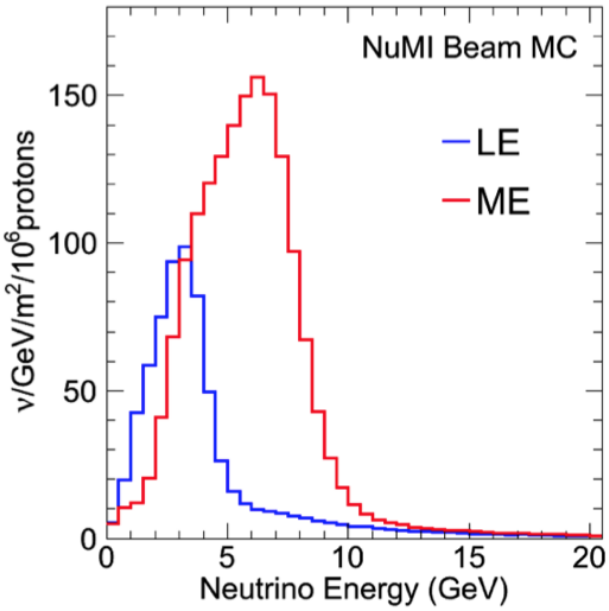

Figure 2.9: NuMI configurations. Low Energy and Medium Energy, plot generated witth [118]

3.0 THE MINERνA DETECTOR

MINERνA is by far the best position to do comprehensive measurements of neutrino interactions on multiple nuclei due to various a type of nuclear targets allows the collaborative environment of 65 nuclear and particle physicists from over 20 institutions (see Appendix A) around the world to study modeling of nuclear effects along side of neutrino cross-section measurements. The collaboration's goals include the measurement of inclusive and exclusive neutrino-nucleus cross sections and the study of nuclear and nucleon structure using neutrinos as a probe. The MINERνA detector, installed 100 meters underground in the NuMI beamline at Fermilab between 2009-2010, is designed with these goals in mind. This chapter describes the design and simulation of the MINERνA detector and its electronics. A full description o MINERνA detector and its performance has been published and can be found at [99, 103].

3.1 DETECTOR DESIGN

The physics goals of MINERνA [99] require a detector that can resolve multi-particle final states, identify the produced particles, track low energy charged particles (for energies greater than about 100 MeV), contain electromagnetic showers, contain high-energy (up to at least 10 GeV) final states, and resolve multiple interactions in a single beam spill. As shown in Figure 3.2, The main body of the detector is a regular hexagonal with a length of 5 m and an apothem of approximately 1.7 m. It composed of an inner detector of apothem 1.07 m that is radially enclosed by an outer detector. The central core of the inner detector is a fine-grained, fully-active scintillator tracker that is capable of resolving charged particle tracks in high multiplicity neutrino interactions. The upstream part of the detector (with respect to the direction of the neutrino beam) edge of the tracker

is adjacent to the nuclear target region, which contains a series of carbon, iron, lead targets that provide a means to study the nucleon number dependence of nuclear effects which will be used for this analysis. A water target reservoire is located between the third and the fourth target . Another additional liquid target which is a liquid helium target is located upstream of the nuclear target region. Most upstream of the detector is the veto wall to reject charged particle backgrounds that are brought together with the beam of neutrino and can enter the front of the detector. The remainder of the tracker and the sides of the nuclear target region are surrounded by electromagnetic and hadronic calorimeters (ECAL and HCAL respectively) for containment of electromagnetic and hadronic showers. Figure 3.1 a perspective of the entire detector.

MINERνA contains approximately 32000 active scintillator strips. The detector is located 2.1 meters upstream of the MINOS near detector, hereafter referred to as the MINOS detector or simply MINOS. The MINERνA detector is unmagnetized and incapable of containing most muons produced inside of it, so MINOS is used as a muon catcher and spectrometer.

3.1.1 Inner Detector

The inner detector consists of four regions, listed here in order from upstream to downstream: the nuclear target region, tracker, downstream ECAL, and downstream HCAL. Additionally, it contains the side ECAL, which is located between the edges of neighboring scintillator planes in the nuclear target and tracker regions. The inner detector is further subdivided along the z-axis into 120 units called modules. There are four types of modules: tracking modules, ECAL modules, HCAL modules, and passive nuclear targets. The tracker, downstream ECAL, and downstream HCAL are constructed exclusively from their respective module types and contain 62, 10, and 20 modules respectively. The nuclear target region contains 5 solid passive nuclear targets, a water target, and 22 tracking modules. The modules are installed orthogonal to the z-axis and there is a $\sim$2.5 mm air gap between each module.

3.1.1.1 Detector Modules A tracker module contains two hexagonal scintillator planes. Each scintillator plane is 1.7 cm thick and contains 127 triangular scintillator strips. Additionally, a hexagonal lead ring (otherwise known as the side ECAL) of thickness 2 mm, inner apothem 90 cm,

and outer apothem 105 cm is located upstream of each scintillator plane. Each plane is rotated in one of three orientations, called views, with respect to the coordinate system. The orientation of the strips in each view are shown in Figure 3.4. In the X view, the scintillator strips are parallel to the y-axis, thus providing position information along the x-axis. The U and V views are rotated in the x-y plane by 60° clockwise and counterclockwise, respectively, relative to the X view. The downstream plane in each tracker module is in the X view, while the upstream plane can be either U or V. The modules are ordered such that the planes alternate throughout the tracker region according to the pattern U X V X. The use of three views enables MINERνA to reconstruct certain track configurations that would be ambiguous in two views: for example, two tracks that have the same projection along the z-axis or overlap in one view.

3.1.2 MINERνA coordinate system

The coordinate system used in MINERνA reconstruction is right-handed which is an unusual orientation. Since the positive Z-direction is defined to be in the direction that neutrinos from NuMI travel and the positive Y-direction is defined to be up (away form the center of the Earth), this requires the positive X-direction to be to the left when looking in the positive Z direction. Although this orientation may appear unusual, it preserves the right-handedness of the coordinate system. See Figure 3.3 for a schematic depicting the MINER?A coordinate system.

Each module in the Tracker region is then composed of either a X and U plane or a X and V plane. Modules are then UX or VX in structure, where the X plane is always on the downstream end of the module. The modules then alternate between UX and VX structure. The positive z-axis lies along the detector's central symmetry axis and points towards MINOS, with the coordinate system origin defined such that z = 1200 cm is the front face of MINOS. The central axis of the NuMI beam lies in the y-z plane and is directed downward at an angle of 3.34° with respect to the z-axis

ECAL modules contain two scintillator planes in the same configuration as the tracker modules, but missing a side ECAL collar. Instead each a 2 mm thick hexagonal lead plane with apothem identical to the scintillator planes is installed upstream of each scintillator plane in the ECAl. The full lead planes help contain electromagnetic showers that would otherwise escape the downstream

end of the detector. The U X V X scintillator plane pattern is maintained in the ECAL.

HCAL modules contain an upstream hexagonal iron absorber of thickness 2.54 cm and a downstream scintillator plane. The modules are arranged so that the scintillator planes are ordered in an X U X V pattern. In the low energy NuMI beam configuration, most hadrons that originate from neutrino interactions in the tracker region are contained by the HCAL.

3.1.2.1 The solid nuclear targets of MINERνA The nuclear target region is unique in that it contains more than one type of detector module. Lead, iron, water, and carbon targets are separated by tracker modules as shown in Figure 3.5. The analysis presented in this thesis does use fully the nuclear target region. MINERνA nuclear targets of Fe, C, Pb, He (table 3.1). Iron is a common absorber used in neutrino experiments. Ideally the nuclear targets should consist of many thin targets interleaved with tracking layers so as to allow the determination of the multiplicity of final states and the energy of each low energy particle. However, several factors limit the size and number of targets and tracking layers. The intrinsic detector spatial resolution is of the order of 1 cm in the z direction (the beam direction) making thiner targets ineffective.

The nuclear target region contains 22 tracking modules and 5 solid passive targets. There are four tracking modules between targets, which improves the reconstruction of tracks and showers. A view of the nuclear targets region is shown in figure (3.5). Passive targets are numbered upstream to downstream 1 to 5. The targets are built out of transverse segments of carbon, iron and lead. The mass of each nucleus is spread around the detector in both the longitudinal and transverse direction to reduce systematic errors from both the event rate and the development of showers originating in upstream targets. Thicker targets are the most upstream, so that they interfere with fewer final state products from interactions in other targets. Targets 1,2 and 5 contain iron and lead, which are divided diagonally on a 20.5 cm offset from the center of the hexagon. Target 3 is made of carbon, iron and lead which occupy $\frac{1}{2}$,$\frac{1}{3}$ and $\frac{1}{6}$ of the are of the target respectively. Target 4 contains only lead. Some features from the targets are:

- Target 1: The most upstream target. Difficult to analyze due to the small number of tracking planes which can be used to identify particles produced outside of MINERνA.
- Target 2: Orientation of iron and lead is flipped horizontally from that of Target 1.
- Target 3: The carbon slice is three times as thick as the iron and lead, which are the same

thickness as the iron and lead in Targets 1 and 2. All materials are flushed at the upstream end, so that there is an air gap downstream of the iron and lead.

- Target 4: Much thinner than the other targets. It is intended to induce electromagnetic interactions of particles from the upstream targets before they enter the low Z tracking region.
- Target 5: Has the same shape as Target 1 but is half the thickness. As the large, fully active tracking region is inmediately downstream of this target, the tracking is a bit more precise than in the other targets.

Each detector module includes six trapezoidal outer detector frames, to be described in more detail in Sec. 3.1.5 . The frames are attached to the module in the pattern shown in figure 3.2, maintaining the hexagonal shape. With the exception of the thickness, the frames are identical across all regions of the detector. Downstream HCAL frames are slightly thicker than the others due to the thickness of the iron absorber.

3.1.2.2 Scintillator Planes Each scintillator plane is a 1.7 cm thick regular hexagon with a 107 cm apothem. The planes are composed of 127 scintillator strips glued together with 3M-DP190 translucent epoxy. Sheets of Lexan are attached to each plane with 3M-DP190 gray epoxy to increase rigidity and reduce exposure to ambient light. Black PVC electrical tape is used to seal joints in the Lexan and cover any remaining light leaks, allowing MINERνA to be sensitive to single photons generated in the scintillator. Figure 3.6 shows an edgewise view of a scintillator plane and demonstrates how the strips are fitted together. The triangular shape ensures that every particle that crosses a scintillator plane will intersect at least two strips. This configuration improves position resolution relative to equally-sized rectangular strips by comparing the amount of scintillation light produced in each strip intersected by the particle.

The scintillator strips vary in length according to their position in the plane, and have a triangular cross section with a base of 3.3 cm and height of 1.7 cm. The scintillator is Dow Styron 663 W polystyrene ($(C_8H_8)_n$) doped with 1% 2,5-diphenyloxazole (PPO) and 0.03% 1,4-bis(5-phenyloxazole-2-yl) benzene (POPOP) by weight. The strips are co-extruded with a 0.25 mm reflective coating of polystyrene and 15% (by weight) TiO_2. For readout, each strip contains a 2.6 mm diameter hole that runs the length of the strip. The hole is centered on the base and is located at a height of 0.85 cm above the base. A 1.2 mm diameter green wavelength shifting (WLS) fiber

is put in the hole and fixed in place by optical epoxy (Epon Resin 815C and Epicure 3234).

The WLS fiber is a 175 ppm Y-11 doped, S-35, multiclad fiber made by the Kuraray Corporation. It shifts the blue scintillation light to green in order to best match the photosensitivity of the MINERνA photomultiplier tubes (PMTs). Only one end of the fiber is read out. The other end is mirrored via an "ice-polishing" technique [119], followed by the deposition of aluminum and Red Spot UV Epoxy layers. The mirroring directs additional light to the readout end of the fiber.

The material composition of the planes must be well understood in order to interpret cross section results on scintillator. The fractional mass density of elements in each material is determined through direct measurement (pure scintillator and coated strips), assayed compositions (coated strips and epoxy), and manufacturer data sheets (Lexan and electrical tape). Table 3.2 summarizes each material's fractional mass density and Table 3.3 summarizes the material assay for a single MINERνA scintillator plane.

3.1.3 The ECAL

The ECAL modules are very similar to the Tracker modules, but with 1 mm lead sheets on the downstream edge of each plane in the module. Modules in the ECAL have an alternating UX and VX modules like in the Tracker region. In total, there are 10 modules in the ECAL. The ECAL causes photons and electrons to shower in a predictable way.

3.1.4 The HCAL

Modules in the HCAL have a fundamentally different structure from modules in the Tracker or the ECAL. Each module contains a 1 inch thick steel absorber and a scintillator plane downstream of the steel. The scintillator planes that compose the HCAL modules alternate in view, having a repeating pattern of XVXU. In total, the HCAL is made of 20 modules. The large mass of the HCAL generally helps contain particles originating from the tracker region in the ID with the exception of energetic muons.

3.1.5 The MINERνA OD

The OD is composed of scintillator strips embedded in steel frames. These are visible as the outermost layer in Figure 3.6. The OD is present to range out particles that escape the sides of the detector. We do not use information from the outer detector for the analysis presented in this dissertation.

3.1.6 The Mirror Plane

A steel plane is installed just downstream of the last HCAL planes. This plane spans only a portion of the detector in the horizontal direction, but provides complete coverage in the vertical direction. This plane is positioned to provide shielding for the HCAL from the magnetic field generated by the MINOS coil.

3.1.7 Plane Composition

Although modules differ by detector region, all planes have the same basic structure regardless of view. Each plane contains 127 alternating triangular scintillator strips. These strips are arranged in a saw-tooth pattern shown in Figure 3.6. The alternating pattern of strips allows for very precise position measurements. A particle that traverses a plane will most likely deposit energy in two strips. The proportion deposited in each strip can be used to form an energy weighted position measurement. This configuration of strips yields a position resolutions of roughly 3 mm.

Each plane is sealed by Lexan ($C_{10}H_{12}O_3$) and electrical tape (undisclosed by manufacturer, most likely PVC (C_2H_3Cl)). This is to ensure that ambient light does not drown out any signals coming from a particle interaction. This is a source of passive material and is accounted for.

3.1.8 MINERνA Strips

MINERνA strips are triangular shaped scintillator bars of varying length. Strip lengths depend on a particular strip's position within a plane. Taking a cross-sectional view, the strips are isosceles triangles 3.3 cm in width and 1.7 cm in height with the 3.3 cm base being the longest side of the triangle.

The scintillator is composed of Dow Styron 663 (W) polystyrene ($(C_8H_8)_n$) [98]. Within this plastic are two dopants. One dopant, 2,5-diphenyloxazole ($C_{15}H_{11}NO$), or PPO for short, comprises roughly 1% of the scintillator mass. The other dopant, 1,4-bis(5-Phenyloxazole-2-yl) benzene ($C_{24}H_{16}N_2O_2$), known as POPOP, is present at about the 0.03% level. The two dopants convert energy from particle interactions within the scintillator to wavelengths of light that can be transmitted by the Wave Length Shifting (WLS) fiber [100].

Each strip contains a 2.6 mm diameter hole running the entire length of the strip. The hole is centered along the 3.3 cm base with the center of the hole lying 0.85 cm above the base. Each hole is filled with WLS optical fiber. The WLS fiber is held in place by optically clear epoxy.

A 0.25 mm layer of Capstock, composed of polystyrene and titanium dioxide (TiO_2), covers each strip. The TiO_2 comprises 15% of the Capstock by mass. This material is applied during the coextrusion step during the manufacturing process of a strip. This material has high reflectivity; this is necessary because light can undergo multiple reflections within a strip before being captured by the WLS fiber.

3.1.9 Helium Target and Veto Wall

From upstream to downstream, the veto wall consists of a 5 cm thick steel plate, a 1.9 cm thick scintillator plane, a 2.5 cm thick steel plate, and another 1.9 cm thick scintillator plane. It is designed to shield the detector from low energy hadrons and tag muons created by neutrino interactions in the surrounding cavern rock (such particles are referred to as "rock muons" in this thesis). The helium target is a 2300 liter aluminum cryostat located between the veto wall and detector. Ref. [99] contains a more detailed description of the helium target.

3.1.10 Light Collection

The WLS fibers are fed into Fujikura-DDK connectors in groups of eight. Each connector is matched to a bundle of eight clear optical fibers that are sealed in light tight material and also terminated by DDK connectors. The clear optical fibers are used to transport scintillation light to the PMTs. The fibers are 1.2 mm diameter S-35 multiclad clear optical fiber manufactured by Kuraray and each bundle is cut to one of four lengths: 1.08 m, 1.38 m, 3.13 m, or 6 m. The length

of the bundle is determined by the location of the WLS fiber connector on the detector. The clear optical fiber attenuation length and mean DDK connector transparency (the percentage of incident light transmitted by the connector) are measured to be 7.83 m and 87.0% respectively.

MINERνA uses 507 Hamamatsu Photonics H8804MOD-2 multi-anode PMTs to amplify the scintillation light. These are essentially the same PMTs used by MINOS [111]. Each multi-anode PMT is a collection of 64 individual PMTs distributed in an 8x8 grid measuring 4 cm^2. Henceforth, the multi-anode PMT will be referred to as PMT and the component channels will be called pixels. The pixels consist of a bialkali photocathode with a borosilicate glass window and a twelve stage dynode amplification chain. The photocathode quantum efficiency is required to be at least 12% at 520 nm and the maximum to minimum pixel gain ratio can be no more than three. The gain of the dynode chain, defined as the number of electrons collected at the anode divided by the number of photoelectrons arriving at the first dynode, is $\sim 5 \times 10^5$. The scintillation light from a minimum ionizing particle typically produces a few photoelectrons at the photocathode, resulting in a few-hundred fC electrical signal at the anode.

Each PMT is mounted onto a base circuit board that contains the Cockroft-Walton high voltage (HV) power source. The operating high voltage is generally between 750-850 V and is distributed amongst the dynodes and anode according to the ratios 3:2:2:1:1:1:1:1:1:1:1:2:5, where the first 12 numbers correspond to the 12 dynodes and the last number refers to the anode. The PMT and base circuit board are installed inside a 2.36 mm thick steel cylindrical box that provides protection from ambient light, dust, and residual magnetic fields. The PMT boxes are mounted onto racks directly above the detector.

Eight clear optical fiber bundles, numbering 64 fibers total, are connected to the faceplate of each PMT box. In the interior of the box, the light is delivered from the faceplate connector to each pixel by clear optical fibers. An 8x8 "cookie", mounted onto the face of the PMT, ensures the alignment of each fiber with its corresponding pixel. The fibers are mapped such that the light from adjacent scintillator strips is not fed to adjacent pixels in the PMT. This minimizes the effect of PMT cross talk, the process by which signal in one pixel can induce a signal in neighboring pixels, on event reconstruction. Figure 3.7 diagrams the fiber mapping.

The PMT boxes also have two optical fiber ports with diffusers on the front face plate. These ports are used to inject a calibration light source into the PMT; see Sec. 4.1.3. In this case, the

light is not transported directly to the pixels by fibers; rather, the light is spread by polypropylene diffusers and arrives at the pixels through spaces in the cookie.

The MINOS detector magnetic coil creates magnetic fields in the vicinity of MINERνA that can be as large as 30 gauss. The performance of the PMTs is adversely affected by magnetic fields higher than 5 gauss, so shielding is necessary. The PMT box itself provides some magnetic shielding. Additionally, the PMTs are oriented perpendicular to the residual field and the 40 PMT boxes closest to the MINOS detector are fitted with a high permeability metal shielding. Finally, a steel "mirror" plane, installed between the MINOS and MINERνA detectors, provides additional shielding.

3.1.11 MINOS Detector

The MINOS Near Detector is a magnetized sampling detector located approximately two meters downstream from the MINERνA detector [112]. The MINOS Near Detector is part of a larger neutrino oscillation experiment with a far detector located in a mine in Northern Minnesota. The MINOS Near Detector, hereafter referred to simply as MINOS, is composed of alternating planes of steel and scintillator. The first MINOS plane after the air gap between MINOS and MINERνA is a 2.54 cm steel plane. The MINOS detector has a tracking region and a calorimeter region following this. In all regions, MINOS scintillator planes are 1 cm thick while steel planes are 2.54 cm thick. MINOS scintillator planes have the same composition as MINERνA scintillator. MINOS planes have an irregular shape as shown in figure 3.8 . Each plane has a hole for the coil that creates the magnetic field within MINOS. In the upstream tracking portion of the detector, each steel plane has a scintillator plane affixed to its upstream edge with a total of 120 such planes. These planes alternate in view, but with only two unique views, U and V. MINOS U and V planes do not have the same orientation as MINERνA U and V planes. MINOS U and V planes are rotated 45^0 clockwise and counterclockwise from the vertical axis. Planes in this upstream region are either partially instrumented or fully instrumented. These terms refer to the fraction of the plane the scintillator covers, with partially instrumented planes having a smaller fraction of coverage of the steel plane. Following this region only one of every five of the remaining 141 steel planes has a an instrumented scintillator plane attached to the upstream edge to the steel . In this region only fully instrumented

plane are used. Fewer instrumented planes are included in this region since trajectory information of a track is not as important as in the upstream regions of the detector. A coil running through the center of MINOS and back along the edge of the detector generates a toroidal magnetic field with an average strength of 1.28 T in the steel planes. A current of 40 kA is used to generate this field. Due to resistive heating from this large current, the coil is water cooled to maintain a safe operating temperature. The purpose of the coil is to make momentum and charge measurements of particles that traverse the detector. The polarity of the current in the field can be switched, so as to better contain either positive or negative muons. This polarity is changed depending on whether FHC or RHC running is taking place. Examining which direction a particle curves in the magnetic field allows an accurate method of assessing the charge. In measuring the curvature of the track, one can also find the momentum of the particle. These details were extracted from the published paper listed at [112]

3.2 DETECTOR READOUT

The raw data retrived from the detector consists of the timing and magnitude of the charges collected at the PMT anode during each beam spill for each of the ∼32000 channels. Each PMT is serviced by a front end board (FEB), mounted directly onto the PMT that is tasked with organizing and collecting data from the PMT. The FEBs are read out by a computer-based data acquisition system (DAQ), facilitated by rack-mounted electronics that handle communications between the DAQ computers and the FEBs. Ref. [103] contains more details and a summary in a big picture of the DAQ is shown on figure (3.9).

3.2.1 MINERνA WLS and Clear Optical Fiber

3.2.1.1 WLS Fiber Each MINERνA strip has a WLS 1.2 mm diameter, 175 ppm (Y-11), S-35, multi-clad fiber made by Kuraray. Multiclad refers to multiple layers of material around a central core of material within the fiber [101]. This design leads to lower attenuation as light travels along the fiber than if a single core were used [101]. The other specifications refer to the chemical

composition of the fiber, which Kuraray does not disclose. WLS fiber is used to shift wavelengths of light from those created within a strip to a spectrum that is suitable for the Photomultiplier Tubes (PMT).

The end of each fiber that is inserted into a strip has a diamond polish to ensure the end of the fiber is flat. A mirror finish is applied to the end of the fiber by vacuum sputtering of Aluminum. Since light can travel in either direction, toward or away from the PMT, having a mirror finish increases the total amount of light yield by reflecting light back toward the PMT tube.

The WLS fiber varies in length depending upon the lengths and position of a strip, but fibers are on average 2.7 m in length. Outside of a strip, the WLS fiber mates to a clear fiber optical cable. Both WLS and clear optical fibers are wrapped in a covering to shield from ambient light.

3.2.1.2 Clear Optical Fiber

Kuraray also manufactures the clear optical fiber. These fibers are 1.2 mm diameter, S-35 Kuraray multi-clad optical fiber. Clear optical fibers in the ID are typically about 1.4 m for ID strips. For OD strips, the length is generally 1.2 m. Clear fibers are then bundled together into eight-fiber connectors that mate to a connector on a PMT box.

3.2.2 Material Composition of the Tracker

To make cross-section measurements using the tracker as a target, we must have a full accounting of all material present in each tracker plane. The scintillator is composed primarily of carbon (C) and hydrogen (H) in nearly equal amounts, but other elements are present in the amounts listed in Table 3.4. These elements are contained in the optical fiber, epoxy, and light sealing materials used in construction of each plane. A careful study was done to assess the relative abundance of each element. A total estimate for each is found in Table 3.4.

3.3 MINERνA PMTS

MINERνA uses 64-anode Hamamatsu R5900-00-m64 PMTs. Each PMT is housed in a PMT box, like the one depicted in Figure 3.10. A PMT box contains eight connectors, each of which can

mate to an eight-fiber connector allowing for a total of 64 fiber connections. Inside the box is a weave of 64 fibers that mate to a cookie, which is a plastic component that aligns the fibers. The weave is arranged in such a way to mitigate optical cross-talk between neighboring channels. The cookie mates fibers to individual PMT pixels. These pixels are arranged in a 8×8 grid with 2mm pitch.

Light from a fiber illuminates a pixel, which can in turn liberate electrons from the anode via the photoelectric effect. The PMT has 12 stages; in each stage electrons are accelerated across a voltage gradient and directed upon an additional anode. This has the effect of multiplying the initial signal by a factor on the order of 10^5 to 10^6 per single photoelectron [102]. The ratio of end number of electrons over the initial number of photoelectrons is refered to as the gain.

3.4 MINERνA ELECTRONICS AND DATA ACQUISITION

The MINERνA electronics and Data Acquisition (DAQ) systems control operations of the detector, readout neutrino interaction and calibration data, monitor data quality, and perform the initial event building. These systems ensure high live-time and quality data-taking.

Some differences exist between the DAQ systems used to take Frozen Detector data and the systems used to take data after the full build-out of the detector. The electronics used during the two run periods are the same. The DAQ software and operating systems differ between these periods. A comprehensive description of the LINUX-based DAQ system in use since the completion of the Frozen Detector run and a discussion of the MINERνA Front End Boards (FEBs) and rack mounted electronics can be found elsewhere [103].

3.4.1 MINERνA Front End Boards

Each PMT has a FEB mounted on the end of the PMT box opposite the clear fiber connectors. The FEBs serve several purposes. The FEBs each contain a Cockroft-Walton (CW) necessary to generate the high voltages that power the PMTs. A FEB also contains six Application-Specific Integrated Circuit (ASIC) chips referred to as TriP-t chips. The TriP-t chips integrate signal charge

from the PMT using 12-bit Analog-to-Digital Converter (ADC) units. The ADC is followed by a pipeline to store integrated charge. Each of the six TriP-t chips has 32 channels which service low, medium, and high gain channels. The high gain channels determine if a discriminator on the TriP-t passes the threshold. The threshold is a minimum amount of intergrated charge that must be surpassed for a channel to have a time associated with it. The initial signal is divided between each gain at input. This is to increase the total dynamic range of charge that can be measured by an FEB, which in turn increases the maximum amount of energy that can be measured on a channel while maintaining sensitivity to single photoelectrons. The number of fC/ADC count for the different gains is shown in Table 3.5.

Each FEB also houses a Spartan 3E Field-Programmable Gate Array (FPGA). This unit controls FEB behavior, timing, and communications with the exterior electronics. These communications are accomplished by bit-by-bit frame relay. Individual frames contain header information with FEB addresses, timing information, various commands, and data. The addresses are necessary to distinguish FEBs once they are daisy-chained together. Communications occur over these chains using Low Voltage Differential Signaling (LVDS) through UTP ethernet networking cables. The FEBs are directly connected to a VME module described in Section 3.4.2.

The smallest unit of time discernible within MINERνA is set by FEBs and a timing module described in Section 3.4.2. The FEBs use a unit of time referred to as a clock-tick. One clock-tick is 9.4 ns, controlled by an on-board crystal oscillator at 53 MHz, chosen to match electronics clock of the Main Injector. By examining the clock-phase, FPGA registers have an effective granularity of a quarter of a clock-tick giving an overall granularity of 2.4 ns for timing from the discriminators. The overall time is found by first initializing the internal clock counter on the FEB to a particular value. These values are set such that all FEBs have the same real start time. This is necessary since signals have different propagation times depending upon where a channel is in the detector. Different regions of the detector involve different pathlengths for a signal. The time of an interaction is then found by counting clock-ticks and taking into account the added granularity gained from the FPGA.

3.4.1.1 Multiple Interactions and Deadtime

Multiple interactions can be recorded on the same channel during any particular beam spill. Beam spills are roughly ten microseconds long,

but the integration gate extends 16 microseconds to capture post-spill muon decays. If a signal crosses the discriminator threshold on a particular channel, timing and ADC information must be pushed into the registers before additional interactions can be recorded. A particular channel, is serviced by two TriP-t chips, with high and medium gain channels serviced by one TriP-t chip and the low gain channel handled by a separate TriP-t chip. During this push all 32 channels on both TriP-t chips servicing a channel are unable to integrate charge. This process takes 20 clock ticks ($\approx$ 188 ns) to complete. We refer to this period where charge cannot be integrated as deadtime. If another interaction occurs on these channels during this deadtime, a fraction of or potentially none of the charge for a particular channel will be integrated.

Another form of deadtime can occur if too many interactions occur within a beam spill. The FEBs have a maximum number of times they can push data to the registers. This maximum number of pushes allows for five timed hits and one un-timed hit for Frozen Detector running and eight (seven plus one) for recent running. Any charge integrated after the maximum number of timed pushes occurs will not have timing information and is not used for this analysis.

3.4.2 Rack Mounted Electronics

Rack-mounted electronics serve as a bridge between the computer that runs the DAQ and the FEBs that readout the PMTs. A chain of FEBs connects to a Chain ReadOut Controller (CROC) module at both ends of the daisy chain [104]. The CROCs are installed within a VME crate [105]. Each CROC can connect to four chains of FEBs. Chains of FEBs typically contain 10 FEBs, but this number can vary slightly by detector region. CROCs contain 6 kB of dual-port memory for each chain. This memory stores frames that are exchanged between the DAQ and individual FEBs. Another module within the VME crate, the CROC Interface Module (CRIM), sends timing and trigger information to the CROCs. Each CRIM can be connected to four CROCs [106]. The VME crate contains a CAEN V2718 crate controller that controls the various modules within the crate [107]. In total, two VME crates, 8 CROCs, and 272 FEBs were active during the Frozen Detector analysis run.

A module within the VME crate, known as the MINERνA Timing Module (MvTM), sends trigger and gate information to the CRIM modules. This module is not controlled by the VME

crate and contains a 53.1 MHz crystal which is used as an internal clock for the module. A clock tick within the MvTM is ≈19 ns. This frequency is selected to match the length of a FEB clock tick, where a FEB clock tick is twice the period for this frequency, or 9.4 ns as described in Section 3.4.1. The MvTM, which uses a modified MINOS timing card [108], distributes the Main Injector timing signal.

During the Frozen Detector era of running, this module received information from the Main Injector regarding the start of a NuMI spill. It then sent a trigger to the CRIM, which sent a command to its CROCs to open the FEB integration gates so neutrino interactions could be recorded. See Section 2.3 for details on NuMI beam spills. The gate over which MINERνA records events opens 0.5 microseconds before the NuMI spill and remains open 5.5 microseconds after the spill. The gate is kept open for an extended amount of time to remain sensitive to Michel electrons from stopping muons and pions. A muon has a mean lifetime of 2.2 microseonds, meaning that activity can be present in the detector for many microseconds after the last neutrino interaction. A computer running the DAQ program reads out data from the CROC module.

3.4.3 The Data Acquistion Computer

The computer running the DAQ program is different for Frozen Detector running and running after completion of construction of the detector. During running for the Frozen Detector data set, data are taken with the DAQ program running on a computer using Windows Vista [109]. Since this period data are recorded using a computer running Fermi Linux [110].

Data runs and other special runs are initiated from a custom written DAQ program on the DAQ computer. An experimenter monitoring operation of the detector oversees the start of a run, data taking, the end of the run, and monitors the quality of the data.

3.4.4 Data Taking Procedures

At the completion of the gate, frames containing the voltage levels, timing, FPGA register information, and the charge recorded on low, medium, and high gain ADCs on a FEB are readout. For the Frozen Detector data set, all FEBs are readout. For the period after completion of construction of the detector, only FEBs where a discriminator threshold is crossed are readout.

A discriminator threshold is crossed when the integrated charge on a high-gain channel passes a set threshold. For Frozen Detector running, up to five different sets of time-stamped ADC activity on a given FEB are readout for a given gate. These frames are transferred from the FEBs to memory located in the CROC before being readout by the computer running the DAQ program.

Data from MINOS are taken and processed by the MINOS collaboration and later provided to MINERνA for offline processing. A description of MINOS electronics is given elsewhere [111].

3.4.5 Special Calibration Gates

During the Frozen Detector running, dedicated calibration runs were taken. These special runs included Light Injection (LI) runs as well as Pedestal runs. Due to the configuration of the DAQ at the time of this particular data run, these types of runs had to be taken in dedicated periods of running and more specifically, not concurrently with data running. These runs were often taken opportunistically, such as when the NuMI beam was not receiving protons from the Main Injector. At other times dedicated runs were taken even though beam was available.

3.4.5.1 Pedestal Gates Each channel has a low level of observable signal present, and this offset is commonly referred to as the pedestal. To properly measure the energy deposited in a channel, this pedestal must be subtracted. Because the level of the pedestal on different channels can drift over time, special runs are taken periodically to ensure that accurate information on the pedestal is available for use in later subtraction.

3.4.5.2 Light Injection Gates Special LI gates are used to ensure that each PMT voltage is properly calibrated. Since PMT gains may drift, periodic LI runs must be taken. A LI box sends signals from Light Emitting Diodes (LED) over a clear optical fiber to a special connection on the PMT box. Fits to LI data allow the gains to be extracted for a particular interval of time.

3.4.6 Nearline Data Monitoring

Data monitoring took place on a Near-Online (Nearline) system. This system involves low level, realtime data processing on a server running Fermi Linux. Low-level hit and timing information

are inspected to ensure that all channels are active and operating in the nominal way. This information includes maps of activity across electronics channels. Collaborators performing control shifts monitor these plots and look for problems such as a malfunctioning FEB or a PMT exhibiting hardware problems. Close monitoring is vital, particularly so during the Frozen Detector running. Seepage of water out of the rock in the ceiling of the cavern that is the Near Detector Hall would "rain" on the FEBs, which are exposed at the top of the detector. This caused occasional FEB malfunction, which a shifter could spot with the use of nearline monitoring plots.

Other monitoring plots include the average of PMT voltages, the distribution of all hits in time, and the average number of ADC counts on low, medium, and high gain channels. A PMT with a voltage too far from the average voltage can be an issue, as this can cause non-optimum gains or potentially damage to the PMT itself. The distribution of hits can be used to ensure that the interactions over time reflect the spill structure of the beam. This is essential to ensure that a MINERνA gate is properly aligned to a NuMI spill. Last, reasonable distributributions of ADC counts on low, medium, and high gain channels verify that activity in the detector is being properly measured.

3.5 DETECTOR SIMULATION

In order to understand backgrounds, detector resolutions and efficiencies, and sensitivity to the physics of interest, the detector simulation has a primordial importance. The MINERνA detector simulation has two components. The first is the simulation of particles traveling through the detector, which provides a prediction of the energy deposited in the active scintillator. The second component is a simulation of the detector optics and electronics read out. It converts energy deposited in the scintillator to light, propagates the light to the PMTs, and simulates the digitization of the electrical signal produced at the PMT anodes. A data overlay technique is used to simulate the effects of pile-up[1], unsimulated backgrounds, detector dead time, dead channels, and time-depedent detector effects.

[1] Pile-up refers to multiple neutrino interactions in the same read out gate.

3.5.1 Particle Propagation

Geant4 9.4.p02 [115] is used to simulate the propagation of particles through the MINERνA detector. However, Geant4 is not used to simulate the initial neutrino interaction. Instead, the GENIE neutrino event generator [114] simulates neutrino-nucleus interactions, including nuclear effects and final state interactions. Chapter 5 discusses the MINERνA implementation of GENIE, focusing on the physics models that it contains. GENIE outputs the particle species and 4-vectors seen in the final state, after final state interactions. Geant4 uses the GENIE output as its input and propagates the particles through the detector.

Geant4 propagates particles through MINERνA in discrete steps. After each step, it calculates the energy deposited in the detector due to ionization and radiation. Energy deposited in the active scintillator is converted to a digitized electric charge by the optical and electronics simulations. Additionally, after each step, Geant4 uses interaction models to determine whether any of the particles interacted in the detector. If an interaction occurs, Geant4 selects the outgoing particle species and 4-vectors according to the interaction model.

The QGSP_BERT model is used to simulate the strong inelastic interactions between hadrons and detector nuclei. It is an intranuclear cascade model that is most accurate for interactions at energies below 10 GeV. The analysis in this thesis is restricted to neutrino energies below 10 GeV and is therefore insensitive to inaccuracies in the QGSP_BERT model above 10 GeV. Standard Geant4 physics modules are used to simulate other physics interactions; some are listed in Table 3.6.

3.5.2 Data Overlay

The data overlay pairs each simulated event with a data gate from the run period that is simulated. Dead channel and electronics dead time information is applied to the simulated event, masking simulated activity that occurs in a dead channel. Certain time-dependent calibrations are also applied to the simulation, according to the time of the overlayed data. Additionally, some of the data activity, *i.e.* the times and energies of hits in the data gate, is added to the simulated event. Only the activity that occurs between the time of the first and last simulated hits is added. All overlayed data activity is propagated through the rest of the simulation in order to simulate its

effect on reconstruction and analysis.

3.5.3 Optical and Electronics Models

The MINERνA optical model converts energy deposited in the active scintillator to photons. Non-linearity is accounted for with Birks' law [125]:

$$N_\gamma = C\frac{dE}{1 + k_B dE/dx}. \tag{3.1}$$

N_γ is the number of photons produced in the scintillator, dE is the deposited energy in path length dx, C scales energy to number of photons, and k_B, called Birks' constant, determines the size of the non-linearity. k_B is set to 0.133 mm/MeV in the simulation, but is measured to be 0.0905$\pm$0.012 mm/MeV by the MINERνA test beam detector [**?**]. This difference is accounted for as a systematic uncertainty. Minimumly ionizing particles (MIP) in MINERνA scintillator lose energy at the rate of $\sim$2.5 MeV/cm, resulting in a $\sim$2% non-linearity. The effect is more noticeable for low energy charged hadrons, which can lose energy at a much higher rate than a MIP. A proton that stops in MINERνA loses 15 MeV/cm or more at the end of its path, resulting in a non-linearity greater than 10%.

The light N_γ is propagated along the WLS and clear optical fibers to the PMT, accounting for attenuation along the fibers and reflection from the mirrored end of the scintillator strip. The effect of scintillator aging is modeled by applying a time-dependent scale factor that forces the simulated distribution of photons to match data. The timing of simulated hits is initially determined by Geant4 and the light propagation time along the optical fibers. It is much narrower in the simulation than data, so a data-driven model is used to smear the simulated hit times.

The quantum efficiency of the PMT cathode is simulated by using a Poisson distribution to calculate the number of photoelectrons (PEs) produced by the cathode. The first two stages of the PMT dynode chain are modeled separately as amplifications with a Poisson width. The remaining stages are treated as a single amplification with Gaussian width. The PMT gains are drawn from the gain calibrations used in the overlayed data gate. The PMT model also includes optical cross talk. Hit digitization is handled by a simple model of the front end electronics.

3.5.4 MINOS Simulation

The positions and momenta of simulated particles that exit the back from MINERνA are fed into a MINOS-owned GEANT3 simulation of the MINOS near detector [112]. The simulation includes the passage of charged particles through the magnetic field and the readout of energy deposited in active elements. Reconstruction is then performed using the hits generated by these simulated particles. Hit and track information is retained from the MINOS gate that corresponds to the MINERνA gate used in the data overlay procedure. In doing so, the confusion during the process of matching a reconstructed track from MINERνA into MINOS that occurs due to event overlap is simulated. Note that overlap during track finding in MINOS is not simulated, because the reconstruction only considers the hits on generated particles.

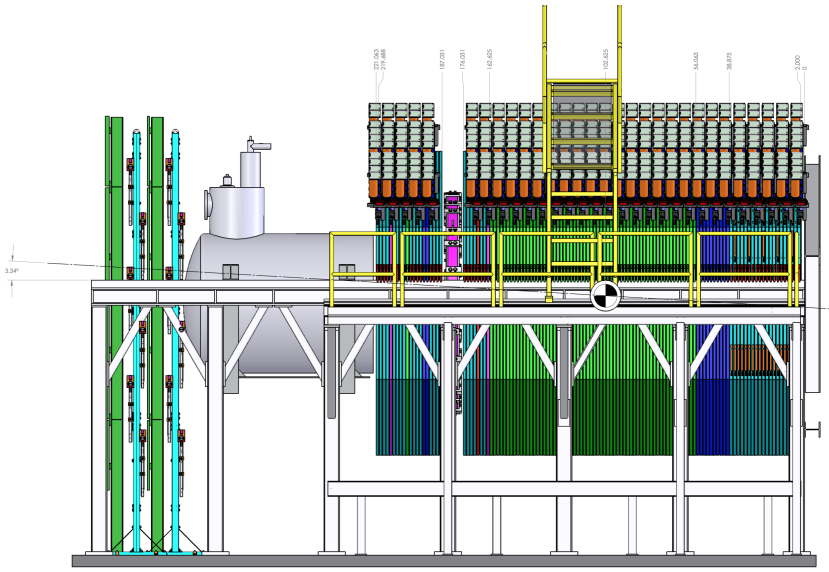

Figure 3.1: MINERνA detector from the veto wall upstream followed by the helium target tank, the main targets composed by the stacked nuclear targets of Carbon, Iron and Lead with the scintillator active materials. The main detector is surrounded by calorimeter (electromagnetic calorimeter and hadronic calorimeter.)

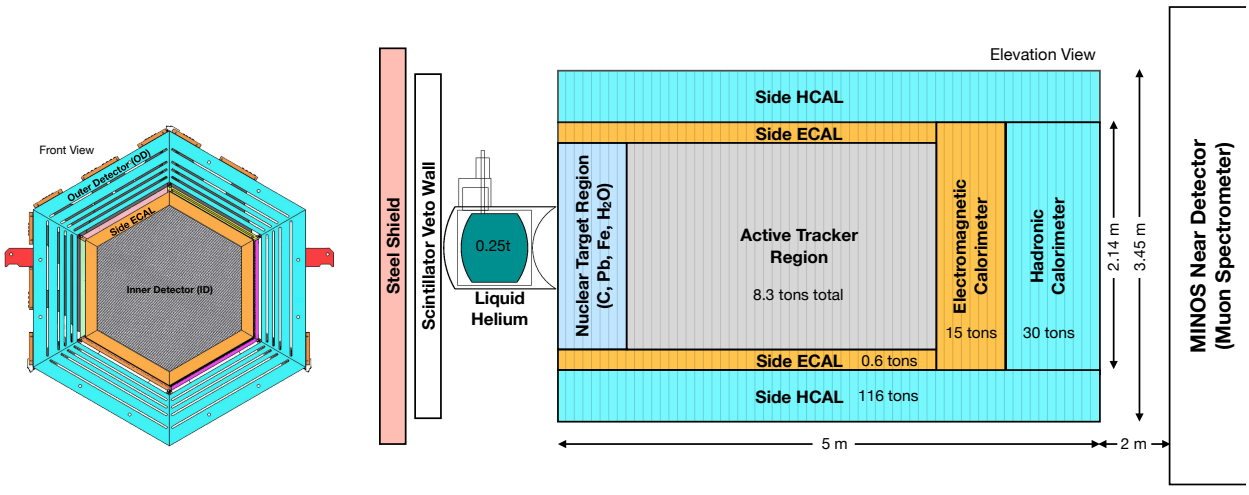

Figure 3.2: Left: front view of a single tracking module. Right: elevation view of the entire detector. Reprinted from [99], Copyright (2014) with permission from Elsevier.

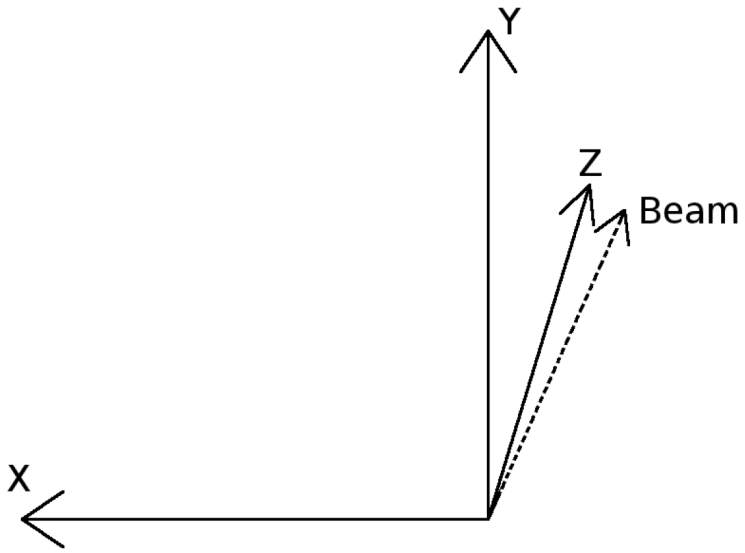

Figure 3.3: The schematic shows the MINERνA coordinate system. The Y-axis is defined to be away from the center of the Earth and the Z-axis is defined to be in the general direction of the beam. This requires that the X direction be to the left to retain a right handed coordinate system. The direction of the beam, which is at an angle 58 milliradians in the negative Y direction with respect to the Z axis in the YZ plane, is depicted as well

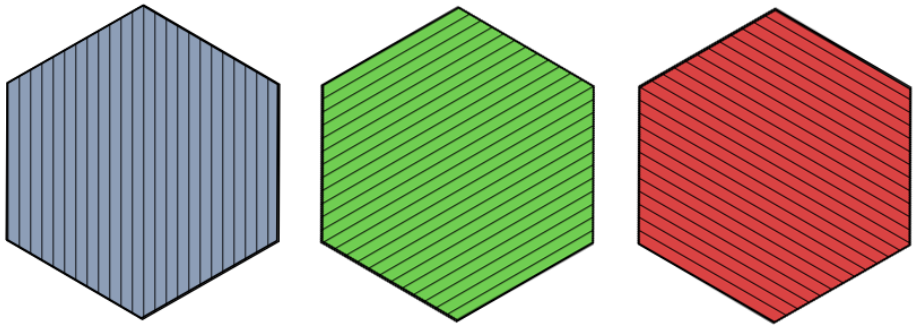

Figure 3.4: The X (left), U (center), and V (right) scintillator plane orientations as seen by an upstream observer. The inner lines show the direction of the scintillator strips. This figure is provided by Laura McCarthy.

Target material	Mass (ton)	Charged current sample (K)
Helium	0.25	14
Carbon	0.12	9.0
Iron	0.99	54
Lead	1.02	57
water	0.39	20

Table 3.1: Charged current events expected at each nuclear target.

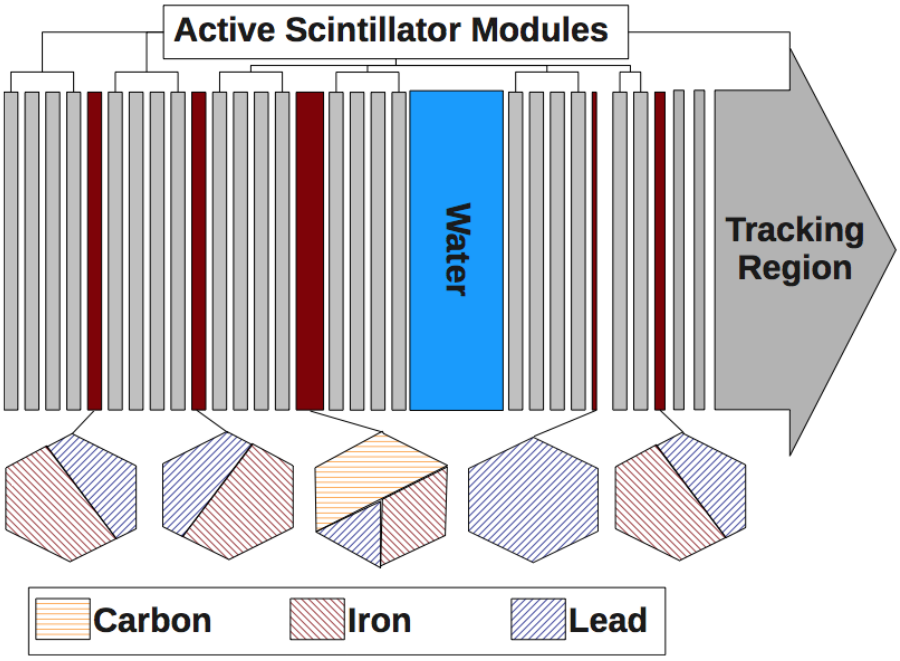

Figure 3.5: The MINERνA nuclear targets region. The beam direction is from left to right. Reprinted from [99], Copyright (2014) with permission from Elsevier.

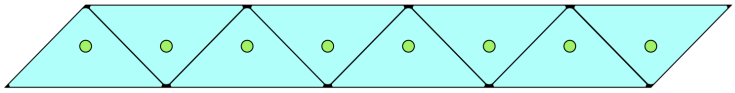

Figure 3.6: Edgewise view of the strips in a scintillator plane. Each plane contains 127 triangular scintillator strips fitted side by side as shown. This figure is provided by Laura McCarthy.

Table 3.2: Density and composition by mass percentage of scintillator plane materials [99].

Material	Density (g/cm^3)	H	C	N	O	Al	Si	Cl	Ti
Scintillator	1.043 ± 0.002	7.6	92.2	0.06	0.07	-	-	-	-
Coating	1.52	6.5	78.5	-	6.0	-	-	-	9.0
Lexan	1.2	6.7	66.7	-	26.7	-	-	-	-
PVC tape	1.2	4.8	38.7	-	-	-	-	56.5	-
Transl. Epoxy	1.32	10.0	69.0	2.6	17.0	-	-	0.5	-
Gray Epoxy	1.70	5.0	47.0	1.7	27.0	6.0	6.0	0.05	-

Table 3.3: Elemental composition of scintillator strips and planes by mass percentage [99].

Component	H	C	O	Al	Si	Cl	Ti
Strip	7.59%	91.9%	0.51%	-	-	-	0.77%
Plane	7.42%	87.6%	3.18%	0.26%	0.27%	0.55%	0.69%

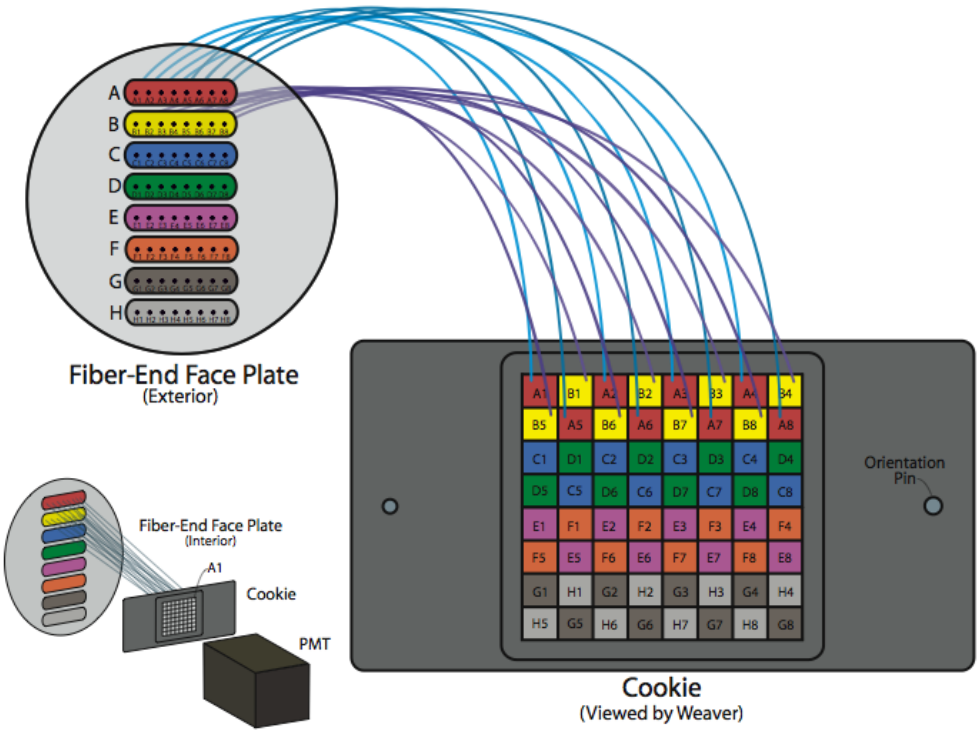

Figure 3.7: The MINERνA PMT fiber map. Clear optical fibers connect to the PMT face plate and interior fibers are routed to the cookie. The cookie is mounted on the face of the PMT pixel array. Reprinted from [99], Copyright (2014) with permission from Elsevier.

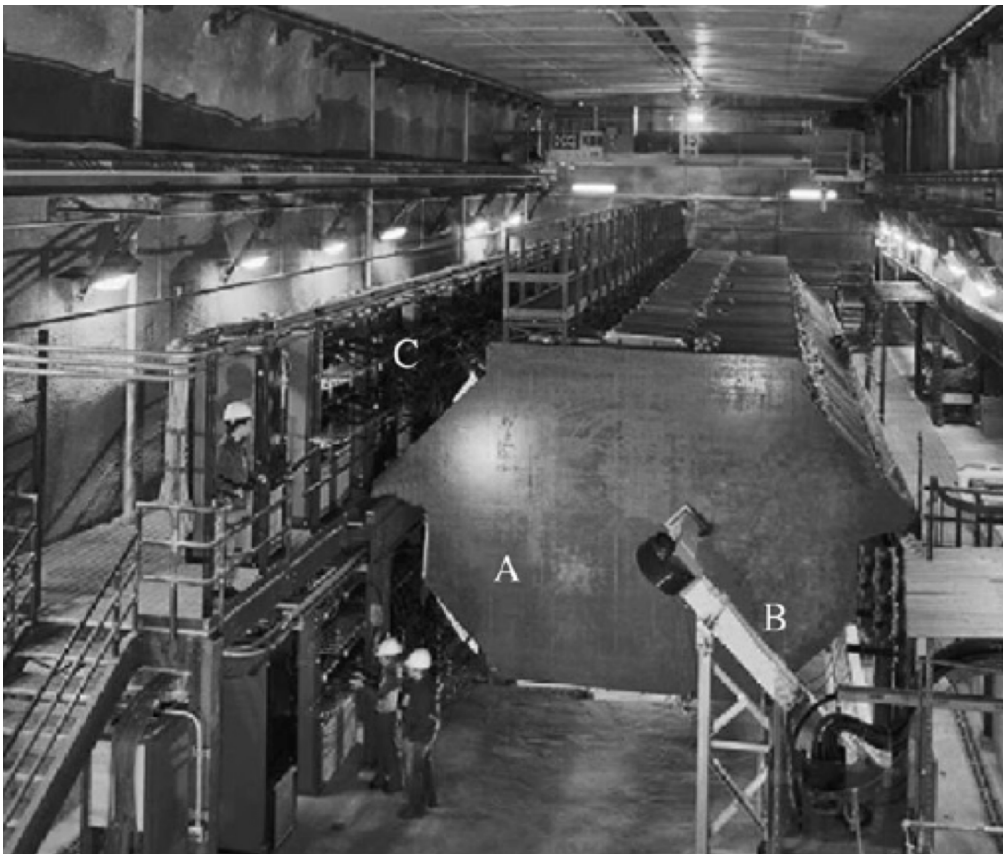

Figure 3.8: The MINOS Near Detector prior to installation of the MINERνA from [112]

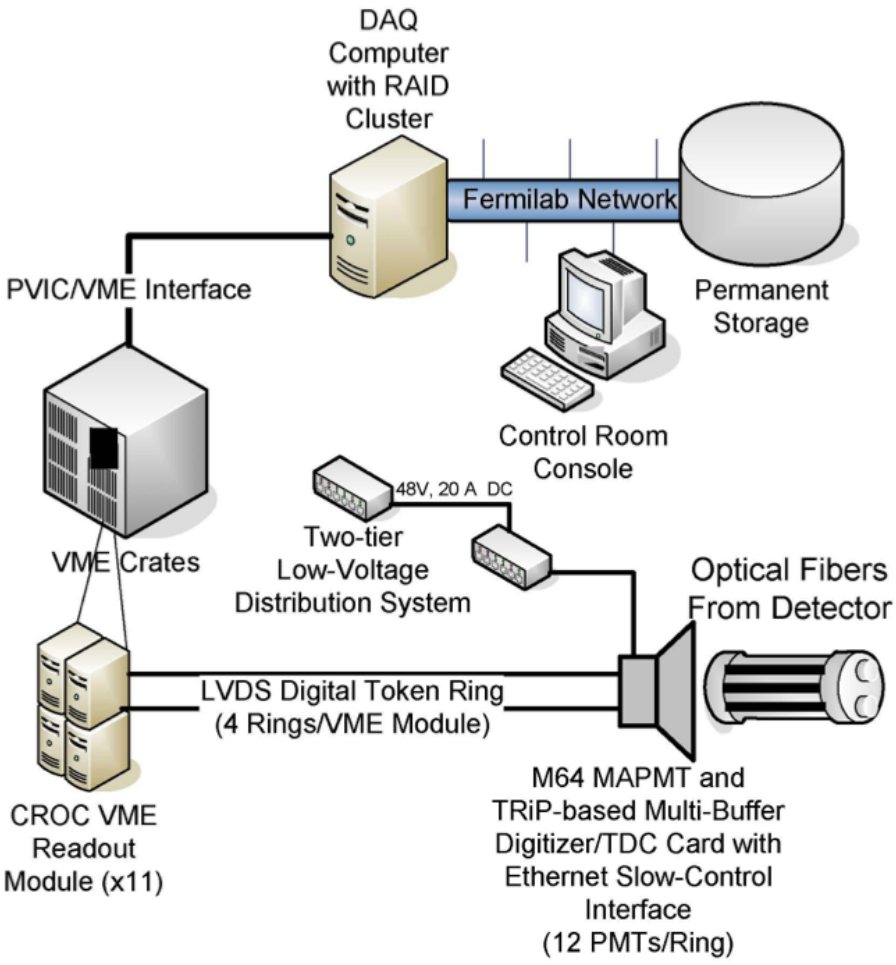

Figure 3.9: Schematic diagram of MINERνA data acquisition system.

Element	Atoms/cm^2/plane
C	0.889×10^{23}
H	0.903×10^{23}
O	0.024×10^{23}
Ti	1.76×10^{20}
Al	1.11×10^{20}
Si	1.29×10^{20}
Cl	1.89×10^{20}

Table 3.4: Number of atoms by type per cm^2 per plane in the fiducial volume.

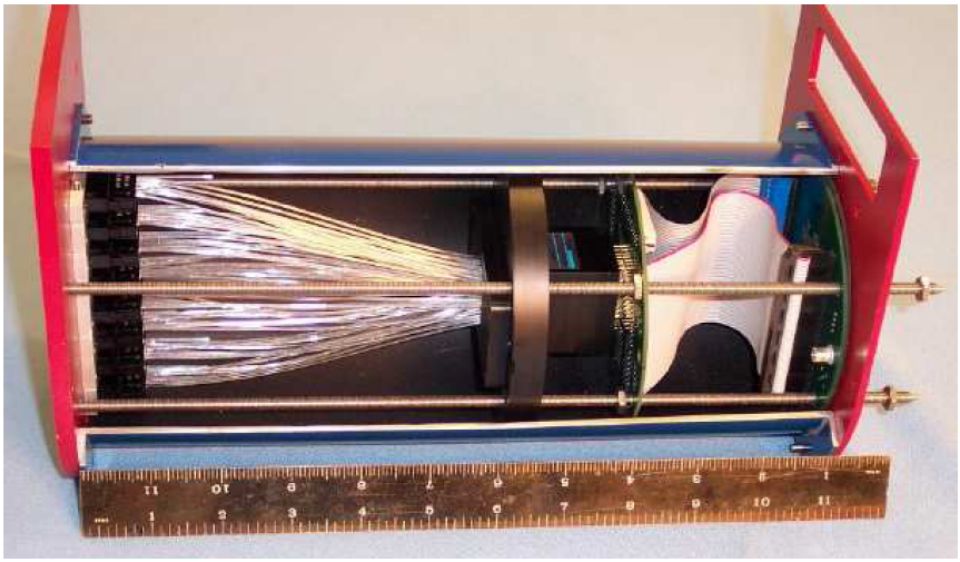

Figure 3.10: A PMT box containing a weave of fibers connecting to a 64-anode Hamamatsu PMT.

Gain	Charge/ADC
Low Gain	1.25 fC/ADC
Medium Gain	4 fC/ADC
High Gain	15.6 fC/ADC

Table 3.5: Number fC/ADC count for different FEB gains.

Table 3.6: Geant4 physics modules used by the MINERνA detector simulation.

Physics Process	Geant4 Module	Notes
Inelastic hadronic	QGSP_BERT	Intranuclear cascade, best below 10 GeV
Elastic hadronic	Hadron_Elastic	Glauber model [**?**] including multiple scattering
Electromagnetic	EmStandard	Bremsstrahlung, e^+e^- production, multiple scattering
Decays	DecayPhysics	-

4.0 CALIBRATION OF THE MINERνA DETECTOR

A full and detailed procedure and results of MINERνA calibration is published at [99].The information collected during a data taking are used to measure the position, energy, and time of charged particles traveling through the scintillator strips. The position is known from the location of scintillator strip that registers a hit. The energy is stored as a digitized PMT anode charge, and the time is an FEB clock tick relative to the start of the read out gate. The actual scintillation energy and its time must be calculated from the digitized data stored by the detector. Misalignments in detector modules must be accounted for when determining the position of the scintillator strips. Calibrating the detector is an important step that help to implements that corrections listed above. This chapter is a brief summary of various steps of calibration for MINERνA detector. [99].

4.1 ENERGY CALIBRATION

In order to convert the digitized PMT anode charge in channel i, denoted ADC_i[1] to to the energy E_i deposited in the scintillator strip. The series of effects that create the measured ADC_i are the following:

1. E_i is converted to scintillation light.
2. The scintillation light is attenuated as it travels along the WLS and clear optical fibers to the PMT. Discrete attenuation also occurs in the connectors that transfer light from one fiber to another.

[1] ADC refers to analog-to-digital conversion.

3. The PMT photocathode converts the scintillation light to photoelectrons (PEs), which are amplified to a measurable electric signal by the PMT dynode chain.
4. The charge at the PMT anode is digitized by the FEB to an ADC charge ADC_i

Figure 4.1 provides a visualization of this list. The energy calibration procedure corrects for these effects in reverse order. The full calibration chain is summarized by the following equation:

$$E_i = Q_i(ADC_i - ADC_i^0) \cdot \frac{1}{g_i(t)} \cdot e^{l_i/\lambda_{clear}} \cdot \eta_i^{att} \cdot S_i(t) \cdot C(t). \tag{4.1}$$

The components of Equation 4.1 are:

- $ADC_i^0(t)$ – The quantity registered by the FEB ADC for zero electric charge. This is called the electronics pedestal.
- $Q_i(ADC)$ – A function that converts a pedestal-subtracted ADC charge to electric charge measured at the PMT anode.
- $g_i(t)$ – The gain (amplification) of the PMT dynode chain. It converts the PMT anode charge to PEs. It is a time-dependent quantity.
- l_i – The clear optical fiber length from the PMT to the scintillator strip.
- λ_{clear} – The clear optical fiber attenuation length. It is measured to be 7.83 m by a dedicated test stand measurement described in Ref. [99].
- η_i^{att} – Attenuation within the scintillator strip. It is not initially known where the particle intersected the scintillator strip, so this correction is initially made to the center of the strip. Three dimensional tracking, described in **??**, provides the position along the strip. The attenuation correction is then adjusted accordingly.
- $S_i(t)$ – A relative time-dependent correction that normalizes the response of channel i to the other channels. This accounts for variations in channel response caused by factors not included in the other calibration corrections. It is only applied to inner detector channels.
- $C(t)$ – A time-dependent correction that converts the channel-to-channel normalized light to energy deposited in the scintillator strip.

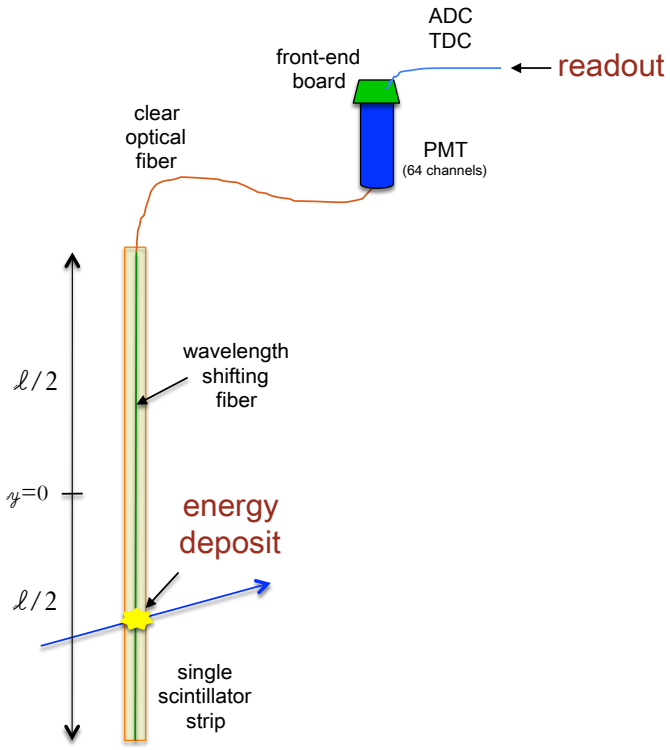

Figure 4.1: Schematic diagram of a MINERνA optical readout channel. The energy calibration procedure converts the ADC charge read out by the DAQ to the energy deposited in the scintillator strip. Reprinted from [99], Copyright (2014) with permission from Elsevier.

4.1.1 Electronic Pedestals

The FEB ADCs register a non-zero ADC value for an input of zero electric charge. This offset, $ADC_i^0(t)$, is the electronics pedestal and must be subtracted from the ADC measurement. The electronics pedestal for every channel on MINERνA is measured *in situ* every $\sim$10.5 hours using 750 empty gates collected between beam spills. Figure 4.2 is a histogram of pedestal data collected over $\sim$30 minutes in a single channel. The outliers in the pedestal distributions are created by discrete background processes such as cosmic rays and radioactivity. Outliers are removed using Peirce's Criterion[42]. The remaining distribution has a small width due to time variation in the channel's electronic noise. The mean and standard deviation of the outlier-subtracted pedestal distribution is measured for each channel. The measured mean is used as the pedestal correction $ADC_i^0(t)$ for data collected in the subsequent $\sim$10.5 hours until the next pedestal measurement. The standard deviation is used by the PMT gain measurement described in 4.1.3.

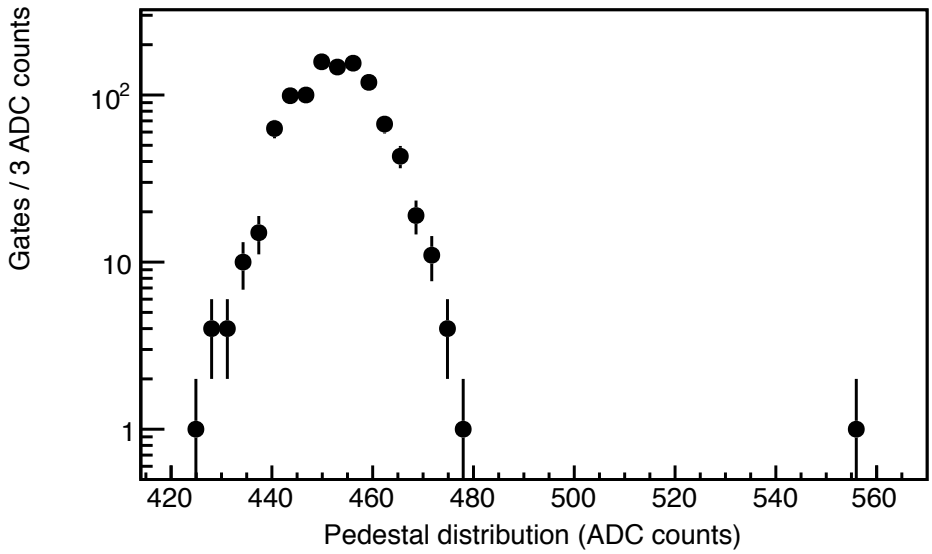

Figure 4.2: Pedestal gates collected in $\sim$30 minutes in a single channel. The outlier at $\sim$555 is removed by Peirce's Criterion before measuring the pedestal mean and RMS. Reprinted from [99], Copyright (2014) with permission from Elsevier.

4.1.2 FEB Calibration

The function $Q_i(ADC)$ is determined *ex situ* for the high, medium, and low gain ADCs of each FEB using data from a dedicated test stand at the University of Pittsburgh. A series of known electric charges were injected into each ADC and the corresponding ADC response was recorded. The response is not linear; this is accounted for by fitting the ADC vs. charge curves to a trilinear function[2]. The fit results reproduce the test stand data to within 1% over the dynamic range of the ADCs.

The trilinear fit parameters for each ADC are stored in an offline database and are used to construct the function $Q_i(ADC)$. The calculation first selects the highest gain ADC that is not saturated, maximizing charge resolution. Next, the pedestal for the chosen ADC is subtracted from the measured ADC value. Finally, the trilinear fit parameters are used to calculate the PMT anode charge.

4.1.3 PMT Gains

PMT response changes with time due to temperature fluctuations and aging. Additionally, the time dependence varies for each PMT. For these reasons, MINERνA monitors PMT response using *in situ* calibration data collected once per day. This is sufficient to monitor response variations; noticeable changes to the response occur over a span of weeks rather than days. PMT calibration data is collected between beam spills so that neutrino data collection is not interrupted.

LED light from a light injection (LI) system is the calibration source. The LI system pulses 23 blue (472 nm) LEDs when triggered by the DAQ system. Each LED flashes 50 optical fibers, and two fibers are routed to each PMT box. Sec. 3.1.10 describes the interface between the LI optical fibers and PMT. This system is sufficient to deliver at least a few PEs to most pixels, and the average light delivered to a pixel does not change significantly with time. However, the exact amount of light delivered is not known *a priori* and the pixel-to-pixel variation in the light is large, about 30%. This situation requires a calibration technique that is insensitive to the amount of calibration light delivered to the pixel.

[2]The trilinear function is three connected line segments. The free parameters are the slope and starting point of each line.

The PMT response that MINERνA measures is the PMT gain g, defined as

$$g = \frac{\overline{Q}}{\lambda e}, \tag{4.2}$$

where $\overline{Q}$ is the mean of the anode charge distribution, λ is the mean number of PEs arriving at the first dynode from the LI source, and e is the electron charge. The quantum efficiency of the photocathode and the collection efficiency of the first dynode are not included in this definition of the gain. These cannot be measured with LI data and are accounted for in the relative channel-to-channel ($S_i(t)$) and energy scale ($C(t)$) calibrations. By assuming that λ is constant in time and using the Rademacker model [**?**] for PMT dynode chain amplification, the gain is measured independent of λ with the following equation:

$$g = \frac{\sigma^2 - \sigma_p^2}{\overline{Q}(1 + w(g)^2)e}. \tag{4.3}$$

Here, σ and σ_p^2 are the standard deviations of the anode charge distribution and electronics pedestal, and $w(g)^2$ is a slowly-varying function of the gain.

The measured gains are used according to Equation 4.1. Figure 4.3 shows the measured distribution of gains in MINERνA for April 1, 2010; most gains are between 4×10^5 and 8×10^5 electrons per PE. Appendix **??** contains more detail on the gain calibration procedure, including the derivation and implementation of Equation 4.3.

4.1.4 Attenuation

The attenuation of light along the clear optical fibers is calculated using measured values of the fiber length l_i and the attenuation length λ_{clear}. The optical attenuation along the WLS fiber in each scintillator strip is measured *ex situ*. Before detector installation, each detector module was scanned with a Cs-137 source by the MINERνA "module mapper". The source was systematically moved along each scintillator strip in the module while a PMT recorded the response. This measured the attenuation as a function of longitudinal position along the strip and is used to calculate the η_i^{att} in Equation 4.1. An alternative *in situ* attenuation measurement using rock muons (see Sec. 3.1.9) agrees with the Cs-137 scan results, but is not as precise.

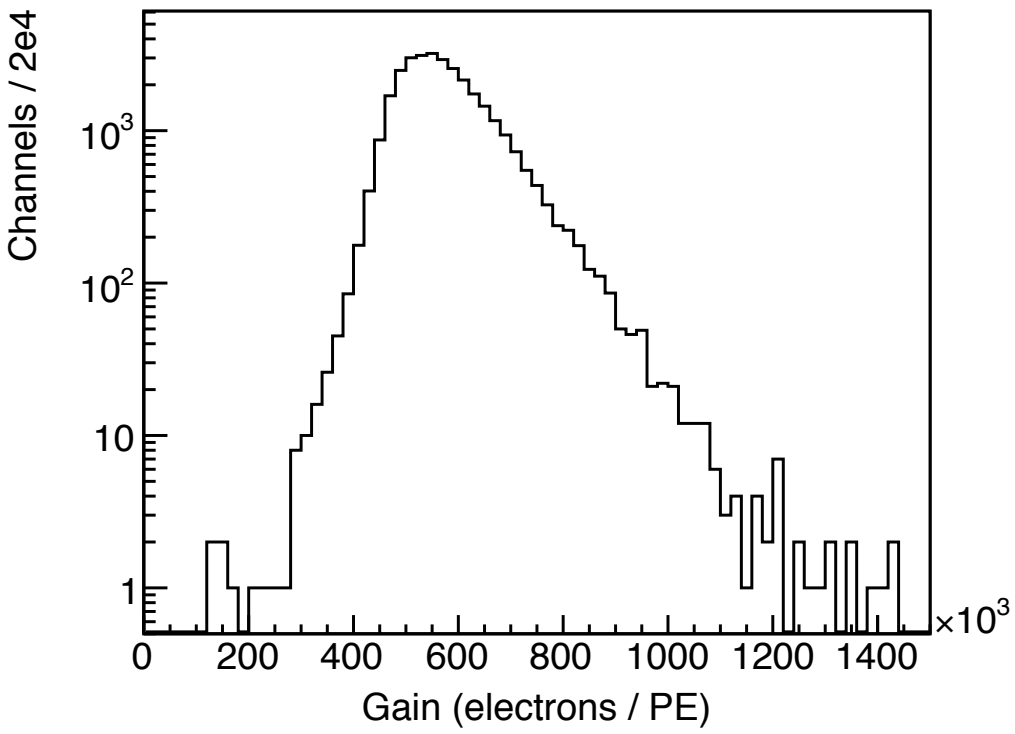

Figure 4.3: The gain measurement for every pixel using LI calibration data collected on April 1, 2010. Reprinted from [99], Copyright (2014) with permission from Elsevier.

4.1.5 Channel-to-Channel Variations

After applying the calibrations described above, there are still channel-to-channel variations in the measured light level. These variations are caused by effects not considered in the other calibrations; for example, the optical coupling between clear fiber connectors is not uniform across channels, and the scintillator composition can vary slightly from batch to batch. The remaining variations can also be time-dependent, *e.g.* changing the PMT installed on the detector changes the photocathode quantum efficiencies and the coupling between the clear optical fibers at the PMT face plate.

MINERνA uses a minimum-ionizing rock muon sample to normalize the channel-to-channel response in the inner detector. First, the plane alignment corrections described in Sec. 4.3 are applied. Next, the procedure calculates a tail-truncated mean energy, corrected for path length, deposited by the rock muons in each scintillator strip i. This quantity is represented as x_i. A calibration constant A_i defined as

$$A_i = \frac{\frac{1}{x_i}}{\frac{1}{u_i}} \tag{4.4}$$

is applied to each strip to remove variations in x_i. u_i is the mean value of x_i for all strips in the detector. If a strip registers zero light for more than 30% of the rock muons that pass through it, it is marked as "dead" and is not used to calculate u_i. Dead channels identified in this way are also not used by the neutrino event reconstruction in data and simulation. The definition of A_i is such that the average value of A_i is one, leaving the overall detector energy scale unchanged.

The desired result is that the path length-corrected peak energy, rather than x_i, is the same in each channel. This cannot be enforced directly because the rock muon statistics are too low to fit for the peak energy response in individual strips. Instead, the peak energy response is measured in each plane after applying the A_i factors to the individual strips. Another factor P_j is calculated for each plane j that normalizes the fitted peak energy response. P_j, like A_i, is constructed such that the overall detector energy scale does not change. The channel-to-channel calibration constant $S_i(t)$ from Equation 4.1 is the product of A_i and P_j. It is recalculated every time the detector hardware changes[3] to account for time-dependent variations in the relative response. Figure 4.4 shows the peak energy response to rock muons across all planes in the detector after applying the

[3]PMTs and FEBs occaisionally malfunction and must be replaced.

channel-to-channel calibrations.

4.1.6 Detector Energy Scale

The detector energy scale correction $C(t)$ is calculated from a rock muon sample by comparing the energy distribution, after all other energy calibrations are applied, in data and simulation. The reconstructed muon positions and momenta in the data sample are used to create the simulated sample in order to avoid kinematic differences. The data and simulated muon energy distributions are fitted to a fifth-order polynomial as shown in Figure 4.5. The physics that describes muon energy loss in scintillator is well-understood and well-simulated, so $C(t)$ is defined as the ratio of the simulated fitted peak to the data fitted peak. $C(t)$ is calculated in two-day intervals to account for scintillator aging.

4.2 TIMING CALIBRATION

Each energy deposit in a scintillator strip is time-stamped with an FEB clock tick that indicates the time at which the corresponding PMT anode charge triggered the channel's high gain discriminator. The timing calibration converts the clock tick to the time at which the energy was deposited in the strip. This correction must account for propagation time along the optical fibers, time slewing, and channel-to-channel timing offsets. The time slewing is primarily caused by variances in the time required to produce scintillation light and is a PE-dependent effect. The channel-to-channel offsets are mostly due to difference in propagation time along cables for FEBs on one chain and timing offsets between different chains. The timing calibration described below is redone after each hardware change to account for changes in the channel-to-channel offsets.

The optical fiber propagation time is calculated using the fiber lengths and the speed of light in the fiber. The time slewing and channel-to-channel offset effects are measured using a rock muon sample. The raw time of hits along each muon track are corrected for optical fiber propagation and muon time of flight. These corrected times are used to calculate a truncated mean time for each muon. The difference between each hit time and the truncated mean time of its muon is

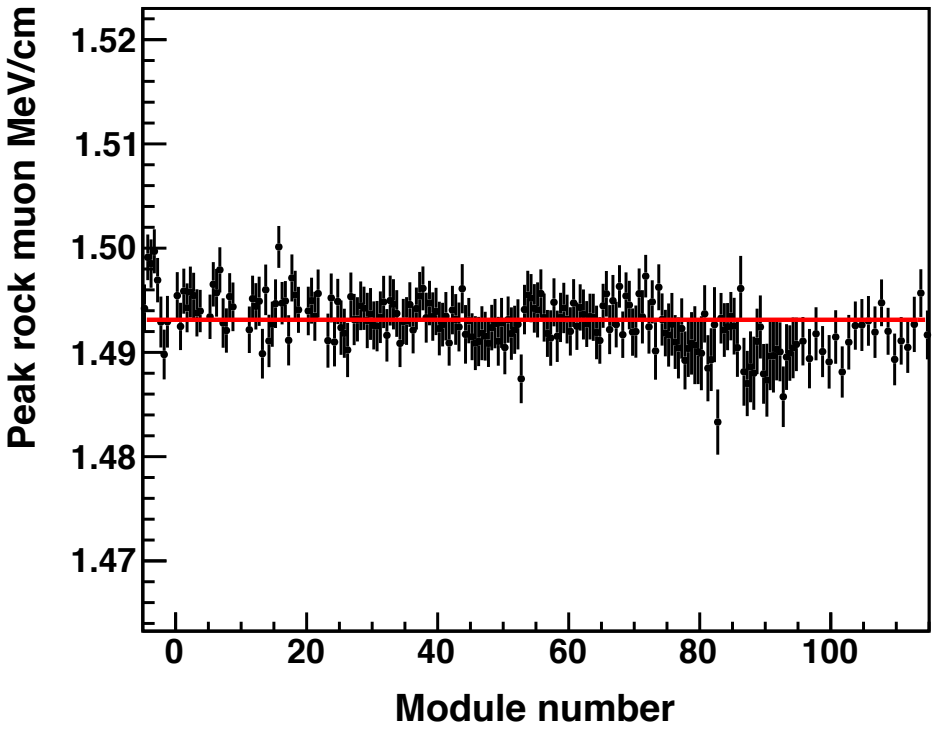

Figure 4.4: The fitted rock muon peak energy per length for each plane. The distribution is flat due to the channel-to-channel calibration. The non-statistical fluctuations, such as those in the ECAL, can be reduced by additional iterations on the fits that calculate P_j, but these fluctuations are already approximately the size of the statistical uncertainty after one iteration. Reprinted from [99], Copyright (2014) with permission from Elsevier.

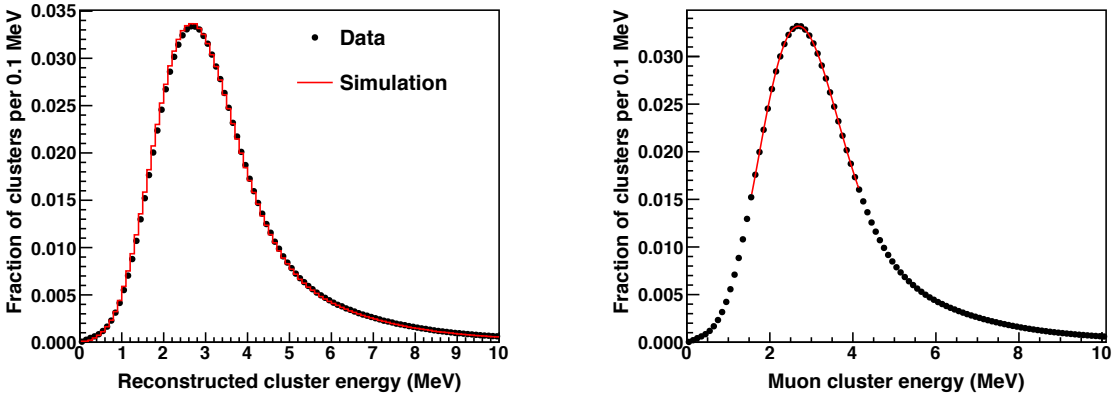

Figure 4.5: Comparison of muon energy in data and simulation (left) and the fit of a fifth-order polynomial to the peak in data (right). Reprinted from [99], Copyright (2014) with permission from Elsevier.

calculated and averaged over all muons as a function of number of PEs, shown in Figure 4.6. This distribution is fit to a polynomial and the fit result is used to apply a time slewing correction for each hit. The channel-to-channel offset is calculated for each group of channels read out by the same high gain TriP-t chip. The time slewing and channel-to-channel corrections are applied iteratively, calculating new truncated mean muon times with the corrections from the previous iteration, until convergence.

Figure 4.7 compares the calibrated hit time to the truncated mean time after the final iteration. The central peak is fitted to a Gaussian with a width of 3 ns. The non-Gaussian asymmetric tails are due to the variance in time slewing, which is a stochastic effect.

4.3 PLANE ALIGNMENT

Detector modules can be perturbed from their ideal position during installation, resulting in misalignment. The misalignments are small, generally a few mm translationally and a few mrad

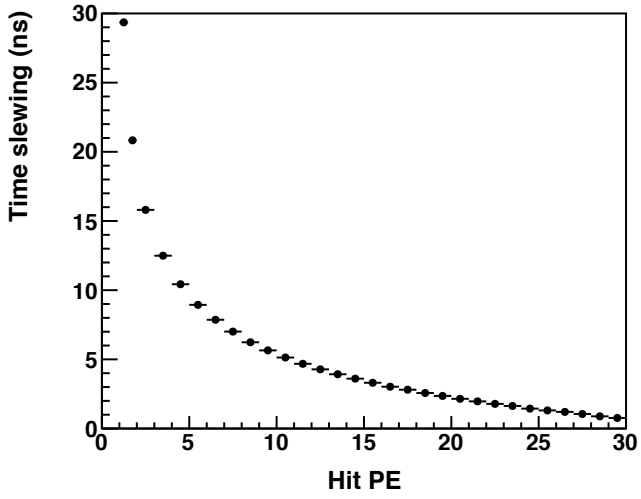

Figure 4.6: Time slewing vs. number of photoelectrons. This is fit to a polynomial to derive the time slewing correction. Reprinted from [99], Copyright (2014) with permission from Elsevier.

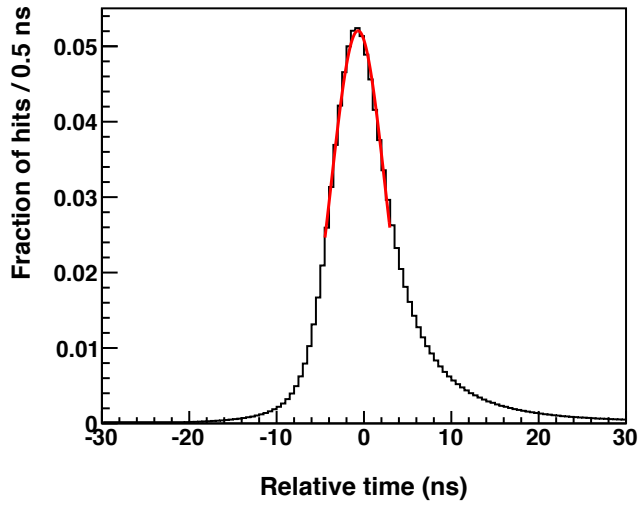

Figure 4.7: Time resolution after applying the timing calibration. Reprinted from [99], Copyright (2014) with permission from Elsevier.

rotationally. MINERνA uses rock muon tracks to measure the translational misalignment along each plane's measurement axis and the rotational misalignment about the z-axis, treating the scintillator strips in each plane as a rigid unit. The average energy deposited in each strip in a plane, corrected for normal incidence, is calculated as a function of the muon intersection point at the base of the strip. The resulting distribution is fitted to the triangular shape of the scintillator strip to find the peak energy. The peak offset from zero is the size of the translational shift for the plane. The peak offsets are then recalculated as a function of the longitudinal position along the strip. The slope indicates the rotational shift. Figure 4.8 shows the distributions used to extract the alignment parameters for two planes.

4.4 PMT CROSS TALK

Cross talk describes the process by which signal in one channel induces a response in another channel. There are three types of cross talk in MINERνA:

- **PMT optical cross talk** – PEs produced by a pixel's photocathode leak to another pixel's first dynode. This most commonly occurs for adjacent pixels.
- **PMT dynode cross talk** – Electrons produced from a dynode in one pixel leak to the dynode in a different pixel. Like optical cross talk, this is effect is strongest in neighboring pixels.
- **Electrical cross talk** – Cross talk between two channels on an FEB.

The two variations of PMT cross talk are by far the most significant seen by MINERνA. Ideally, PMT cross talk is measured on an *ex situ* test stand that systematically injects a known quantity of light into each pixel while measuring the response in the other pixels. This was not done before PMT installation, so instead a sample of rock muons is used to calculate an average cross talk fraction per PMT.

Each rock muon is associated with a time slice, defined in Sec. **??**, that groups the hits on the rock muon track with other hits that are coincident in time. Hits that are not on the rock muon track are considered to be cross talk candidates if they register in pixels that are on the same PMT as a rock muon track hit. This safely avoids confusion of cross talk with other muon-induced activity,

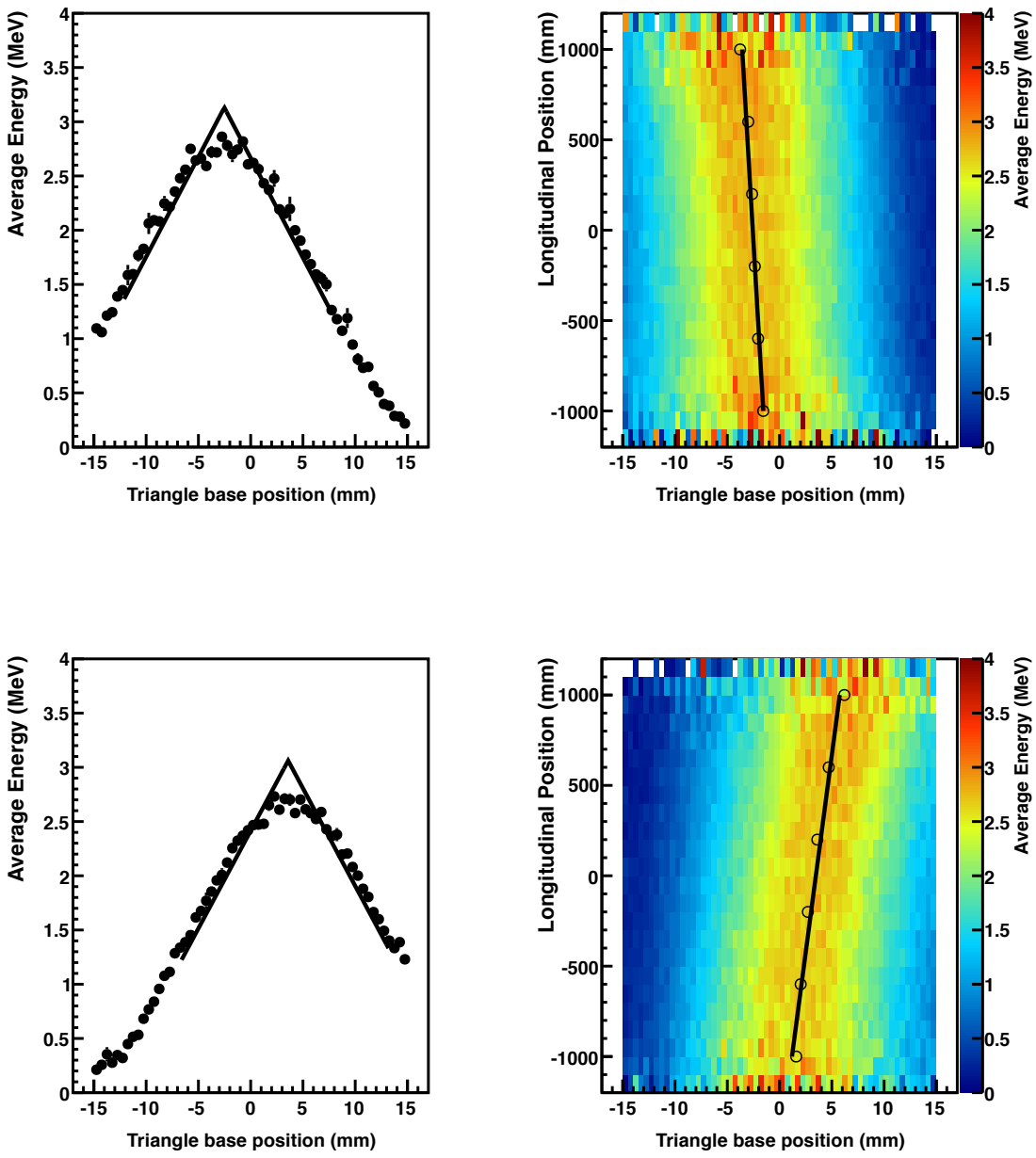

Figure 4.8: The distributions used to calculate the alignment shifts for module 50, plane 2 (top) and module 61, plane 1 (bottome). In the left plots, the offset of the peak in the triangular fit from zero indicates the translational shift in the plane. In the right plots, the rotational shift is calculated from the slope. Reprinted from [99], Copyright (2014) with permission from Elsevier.

like delta electrons, because the PMT fiber weave described in Sec. 3.1.10 ensures that neighboring scintillator strips are not serviced by neighboring PMT pixels. The PMT average cross talk fraction is defined as the ratio of the energy of cross talk candidate hits to the energy of on track hits. A version of this quantity for nearest-neighbor (adjacent) pixels, called $f_{xt,NN}$ is also calculated. $f_{xt,NN}$ is typically less than 4%; it is plotted for all PMTs and compared to the MINERνA optical cross talk simulation in Figure 4.9.

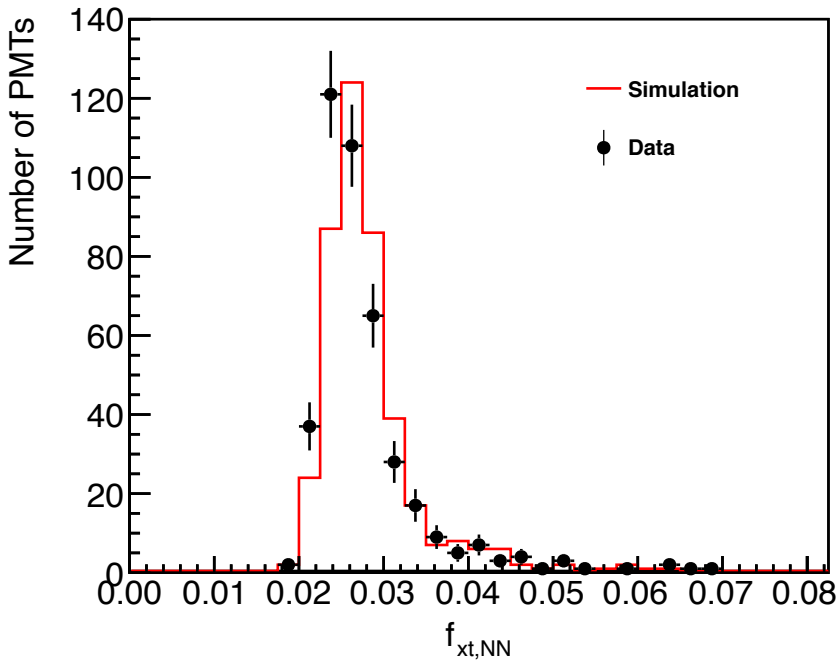

Figure 4.9: Data-simulation comparison of the nearest neighbor cross talk fraction. Reprinted from [99], Copyright (2014) with permission from Elsevier.

5.0 RECONSTRUCTING AND SIMULATING NEUTRINO INTERACTIONS IN MINERνA

MINERνA reconstruction can be characterized as either low level or high level reconstruction. Low level reconstruction is performed only for data. High level reconstruction is identical for data and the simulation. In addition to the reconstruction, each component of MINERνA is simulated including each step of processing. The simulation of the beam line is curtail.

5.1 LOW LEVEL DATA PROCESSING

The data that read out from the detector is initially in long unbroken frames of binary that need to be unpacked into a more readily usable structures. After this unpacking follows the assemblage of data objects corresponding to a particular channel. Any channel with integrated charge above the discriminator threshold for the high gain is referred as a hitThe time for a hit is found by looking at the time the discriminator threshold is passed. The next level of processing includes performing pedestal subtraction and applying all relevant calibrations to each channel.

Information are unpacked for the entire gate, which corresponds to a single NuMI spill. After unpacking, each gate contains all relevant MINERνA detector information for that spill. This includes a record of any hardware problems, information for each channel of the detector, and relevant timing information.

5.1.1 Pedestal Subtraction

The procedure for taking pedestal measurements is described in Section 4.1.1. Examples of high gain pedestals are shown in Figures 5.1 and 5.2, with the latter containing a background hit potentially from a cosmic ray. When subtracting pedestals, outliers that come from likely background activity are removed before finding the appropriate value for the pedestal to subtract. Since pedestals can potentially change over time, a search is performed to find pedestal data closest in time to the data. Pedestals are subtracted for low, medium, and high gain channels. This is performed prior to all other processing and calibrations.

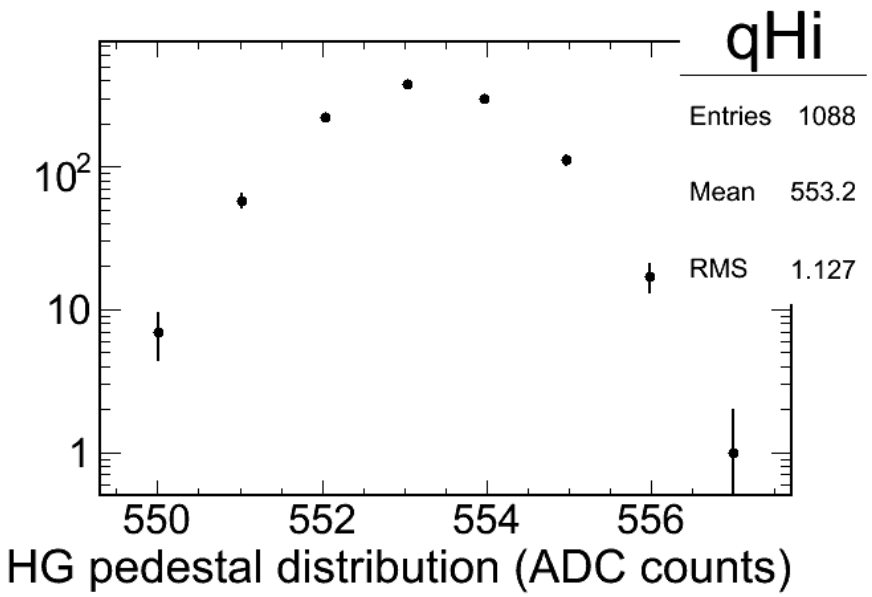

Figure 5.1: High gain pedestal. This plot was made by A. McGowan of the MINERνA collaboration.

5.1.2 Applying Calibrations

A variety of calibrations are applied to each channel which we access from a database. Here calibrations include the factor for converting ADC counts to energy. Calibrations for FEBs are applied as well, for different PMT gains, for variations between strips within the detector, for timing misalignment and smearing, and for variations in the observed strip response to muons (Muon Energy Unit, MEU).

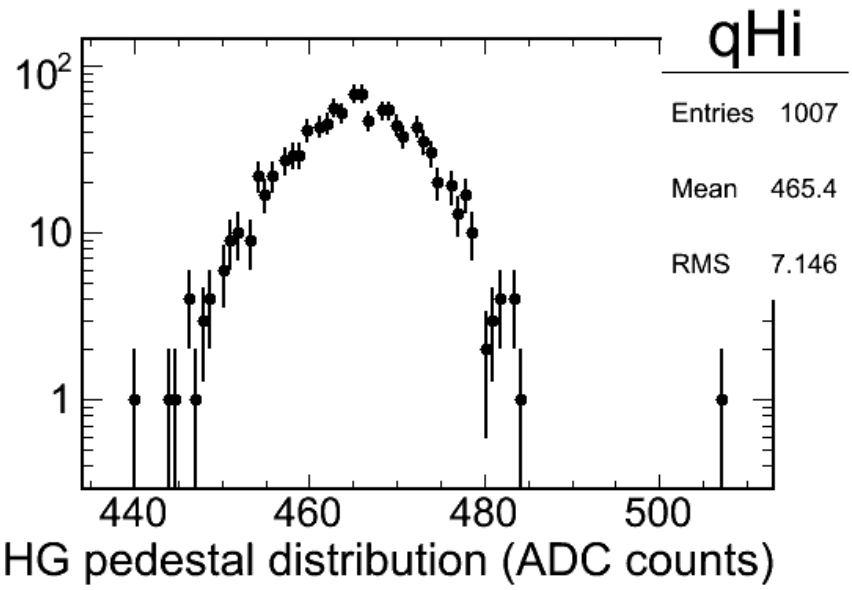

Figure 5.2: High gain pedestal with a background hit near 508 ADC count, which could potentially be from a cosmic ray. This plot was made by A. McGowan of the MINERνA collaboration.

5.1.2.1 FEB Calibrations Prior to installation, all FEBs undergo charge injection tests. This involves injecting known amounts of charge into each FEB and monitoring the response in the high, medium, and low gains for each channel. A fit is done using a tri-linear function to parameterize the response for each of the gains on each channel. A tri-linear fit is used since we observe up to three different linear regions with unique slopes when looking at the number of ADC counts as a function of charge. The linear regions are separated by sharp transitions or kinks. The fit returns both the slopes in units of ADC/fC and the locations of the kinks that are the boundaries between the different slopes. An example of a tri-linear fit for all 64 channels on an FEB is shown in Figure 5.3.

When performing these fits, care is taken to stay away from the saturation point. We apply these fitted parameters as calibrations to map the number of ADC counts to a particular charge. Since the slopes and the transition points, or kinks, can differ from channel to channel, this correction must be applied or non-linear effects could be observed in later steps of processing.

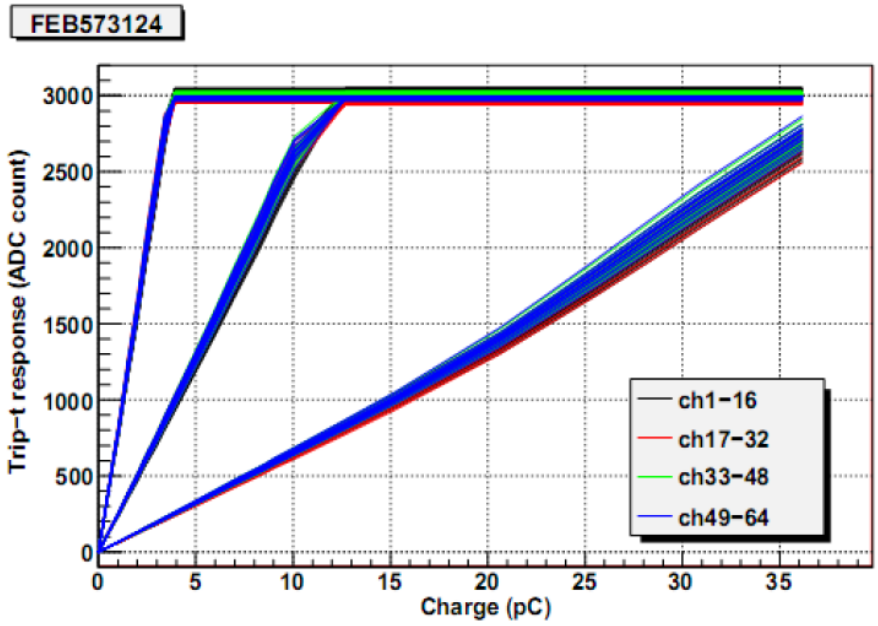

Figure 5.3: Tri-linear fits to characterize high, medium, and low gains for each channel on a particular FEB. This plot was made by I. Danko of the MINERνA collaboration.

5.1.2.2 PMT Gain Calibrations Gains for the PMT can very over time and with temperature. To account for this variation, frequent calibrations are applied. Calibrations are found for PMT gains by using light injection data which we take on the order of once per day. The gain are found for a channel by performing a fit using these data. The fit function, shown in Equation 5.1, incorporates σ_{Q}^2, the variance of the number of photoelectrons arriving at the first PMT dynode, σ_{p}^2, the variance of the single photoelectron peak, $\overline{\mathrm{Q}}$, the variance of the pedestal, and $\mathrm{w}^2(\mathrm{g})$ given in Equation 5.2, which is a function of the gains at each of the PMT stages. Note that the gain at each dynode stage is a function of the voltage at that stage, as shown in Equation 5.3.

$$\mathrm{g} = \frac{\sigma_{\mathrm{Q}}^2 - \sigma_{\mathrm{p}}^2}{\overline{\mathrm{Q}}(1 + \mathrm{w}^2(\mathrm{g}))}. \tag{5.1}$$

$$\mathrm{w}^2(\mathrm{g}) = \sum_{\mathrm{i}=1}^{12} \frac{1}{\prod_{\mathrm{k}=1}^{\mathrm{i}} \mathrm{g_k}}. \tag{5.2}$$

The value $\mathrm{g_k}$ in Equation 5.2 is the gain at a particular dynode stage of the PMT, and can be found by

$$\mathrm{g_i} = \mathrm{g_1} \left(\frac{\mathrm{V_i}}{\mathrm{V_1}} \right)^{\alpha}, \tag{5.3}$$

where $\mathrm{g_1}$ is the gain for the first dynode in the PMT, $\mathrm{V_i}$ is the voltage at stage i, $\mathrm{V_1}$ is the voltage at the first dynode stage, and α is 0.75 based on data from Hamamatsu [102]. We use PMT gains to convert from the amount of calibrated charge to the number of photoelectrons. The a distribution of PMT gains foud with the above method is shown in Figure 5.4.

5.1.2.3 Calibrating for Variations between Strips Some variations are expected to exist between strips. This could be due to variations in materials such as different batches of scintillator as well as other differences such as whether air bubbles exist in the epoxy used to fix the WLS fiber within the strip. A strip by strip correction is applied to account for this. The calibration is found by using rock muons, which are muons generated by neutrino interactions in material upstream of the detector. Only rock muons matched to a muon in MINOS are used. The procedure for matching muons that pass out of the MINERνA detector to muons found in MINOS is desribed in Section 5.3.6. The amount of energy a muon should deposit in a strip per cm traversed is easily

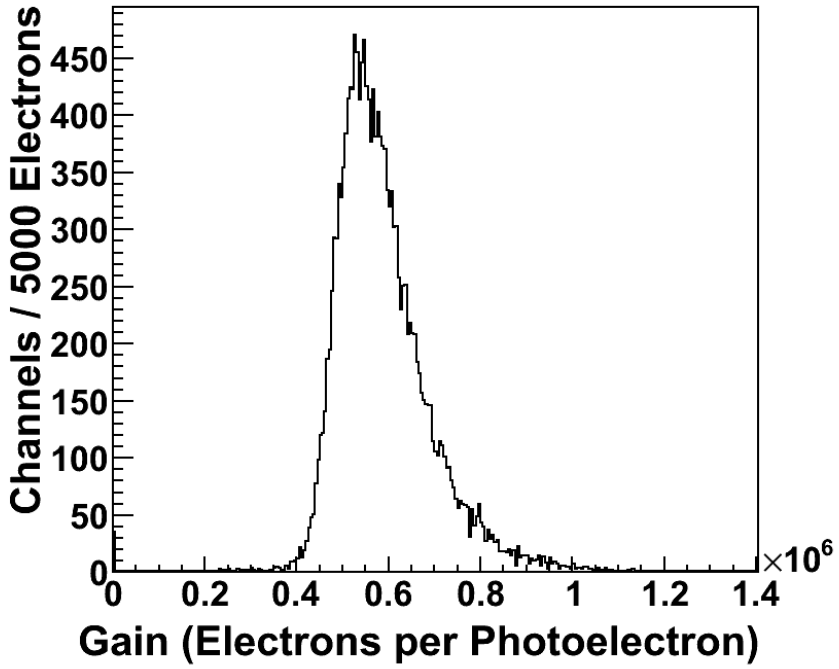

Figure 5.4: PMT gains for a particular time interval. This plot was made by B. Eberly of the MINERνA collaboration.

found. A multiplicative correction is applied to remove variations between strips in response to muons. Figure 5.5 shows the result of applying this calibration on observed value of $\frac{dE}{dx}$ in a strip.

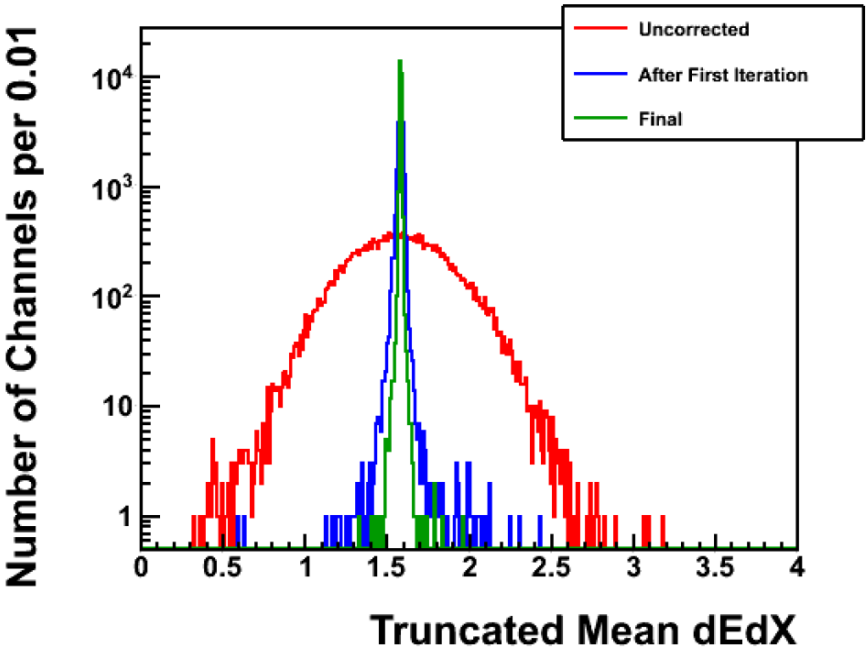

Figure 5.5: Result of applying the calibration for variatons between strips after the first and last iterations of this calibration compared to the uncalibrated distribution. This plot was made by C. Marshall of the MINERνA collaboration.

5.1.2.4 Timing Calibration Two different corrections for timing are made. Even after synchronizing FEBs, small timing offsets still exist between FEBs. The offsets are found and applied for each FEB.

In addition to FEB timing offsets, a correction for charge slewing is applied. Charge slewing occurs due variations in the time required to pass the discriminator threshold. Larger signals have a faster rising edge than smaller signals which results in large signals passing the discriminator threshold earlier than small signals would. This leads to systematic differences in time between small and large signals. The behavior of this timing offset as a function of charge is mapped out and used to apply a correction. Charge slewing also changes over time since the level of slewing is dependent on the gains for a particular channel, which also can vary with time. As a consequence, slewing corrections are found for particular intervals of time.

5.1.2.5 MEU Correction Although similar in some respect to the correction made for variations between strips, this accounts for other time dependent effects such as the level of scintillator response to a particle decaying over time. The Near Detector Hall temperature is consistently higher than design leading to some degradation of the scintillator response. As a consequence of this effect, the expected amount of light generated by a minimum ionizing particle will decline over time. Apart from the effects of scintillator degradation, we also expect the overall response to vary with temperature of the Near Detector Hall as well. The time dependence of muon response can be found in Figure 5.6. This is a step of muon equivalent units or MEU calibration.

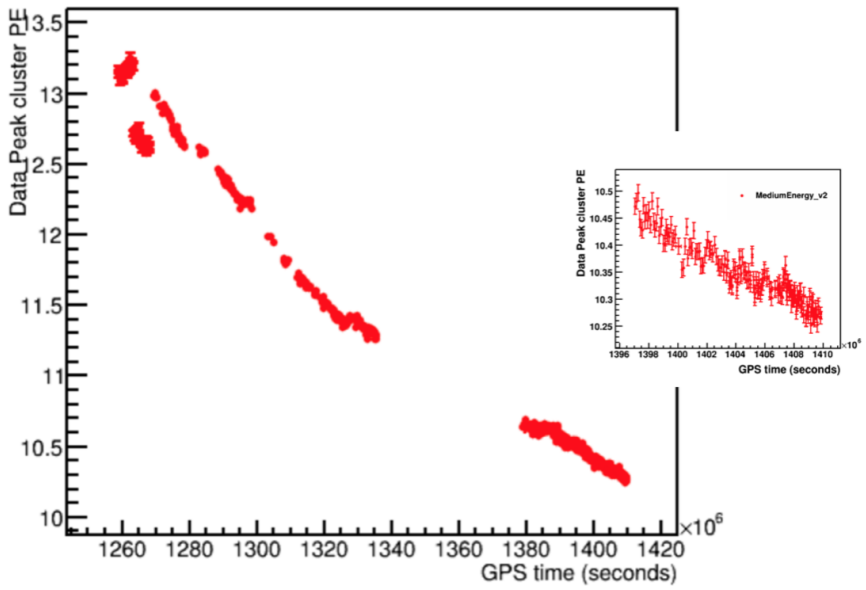

Figure 5.6: A plot of the peak number of photoelectrons for muons versus time. Note that two effects are present, temperature variations and degradation of the scintillator. The varying response to muons requires a time dependent MEU calibration to account for this. This plots is the most recent version including newly medium energy data set starting at $1380x10^6$ second and zoom at the smaller distribution.

To make a correction for the variations in response,rock muons with MINOS match are used . A fit is done for different intervals of time of the peak energy for a rock muon in data compared to simulation using a fifth order polynomial. The result of the fit is used to correct for the MEU response in data. Data and simulation overlays of muon cluster energy after the MEU calibration are shown in Figure 5.7.

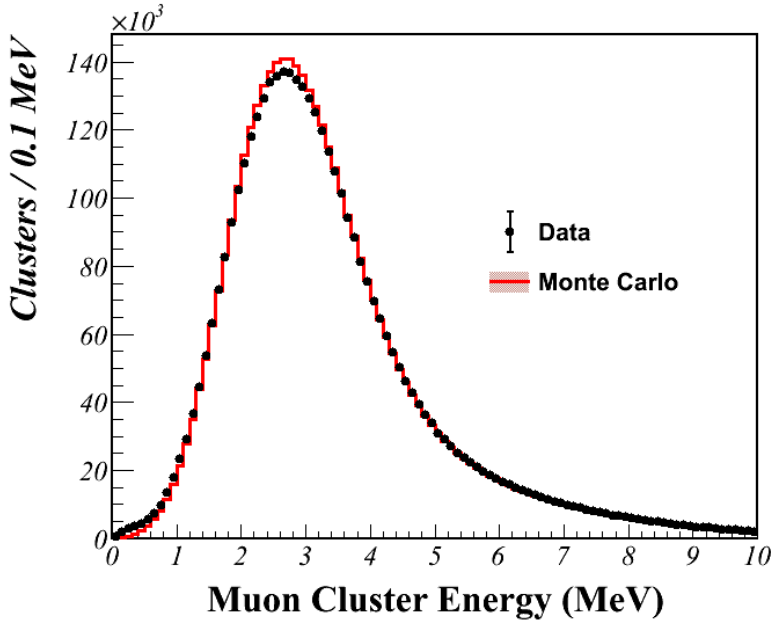

Figure 5.7: Data and simulation overlays of muon cluster energy after the MEU calibration is applied.

5.1.2.6 Converting from ADC Counts to Energy ADC counts from a FEB channel need to be converted into an energy. ADC counts for low, medium, and high gains are inspected and a particular gain is selected for conversion to energy. The gain that is used depends upon the particular value of the charge found on a channel as given by the FEB calibrations. Different gains saturate at different points and have general ranges where they are approximately linear. Once a gain is selected, the above calibrations are applied to map ADC counts to charge, then photoelectrons, and then to an energy.

5.1.3 Mapping Electronics Channels to Detector Channels

Electronics channels on a particular FEB need to be associated with a particular detector channel. This involves a complex mapping that requires detailed knowledge of fiber connections for all detector channels and the weave of fibers within a given PMT. A new hit is created for each unique signal associated with a particular detector strip.

5.1.4 Information from the NuMI Beam

As a last step of low level processing we match information gathered on each NuMI spill to each MINERνA gate. We access this information from a MINOS mysql database. This information includes the number of POT for that particular spill and various beam parameters such as the transverse width of the beam, the current on the horns, and the time of the spill. POT are the quantity in which we report the total beam exposure.

5.2 MINERνA MONTE CARLO

The simulation for our analysis involves several different Monte Carlo (MC) packages. We use the GENIE [114] package, version 2.6.2, to simulate neutrino interactions and final state interactions within the target nucleus. We use different Geant packages, Geant4 and GEANT3, to model several different systems. Geant4 is a C++ based, object oriented simulation package used to simulate the basic physical interactions of particles in matter [115]. The package allows flexible usage of interaction models and also allows tuning of some of those models. Geant4 is an integral part of the G4numi package that we use to simulate the neutrino and anti-neutrino fluxes. G4numi uses Geant4 version v9.2p03. Geant4 version 9.4.p02 is used to simulate particle interactions inside MINERνA as well as the behavior of different detector components such as the electronics. We use Geant4 version 9.3 to simulate the effect of the ArgoNeuT detector on reconstruction. An earlier Fortran version of Geant, GEANT3, version 21.14.a, is used to simulate the MINOS detector [116].

5.2.1 Simulation of the NuMI Beam

We simulate the target and horn systems to predict the spectrum of pions and kaons that create the neutrinos and anti-neutrinos that we observe in the MINERνA detector. The g4numi package is used for this purpose which makes use of QGSP physics lists in Geant4 9.2p03 [115] to model hadron production and reinteractions within the target system. This model is imperfect, which is why we apply a reweighting scheme to better reflect the flux. Reweighting involves applying

a multiplicative factor for particular events when populating distributions based on the weight a particular event should have. We describe this method in Section 5.2.2. This reweighting scheme cannot be applied for all simulated neutrino interactions. For those cases, we simulate the flux with other hadron models, namely QGSP_BERT, QGS_BIC, QGSC_BERT, FTFP_BERT, and FTF_BIC. We use the resulting spread of predictions in the "1000 universes" method described in the Section **??** on systematic errors stemming from the flux. In all cases, we simulate the decay of pions and kaons in flight to muons, neutrinos, and anti-neutrinos.

5.2.2 Central Value Reweighting

The g4numi simulation predicts pion and kaon production off of the graphite NuMI target; however, issues exist with the accuracy of the predicted pion and kaon production cross-sections. To address this, two exterior data sets are used to reweight the predicted pion and kaon distributions created by 120 GeV protons colliding with the NuMI target. For pions with $\mathrm{x_F} < 0.5$, NA49 data [117] is used to reweight pion production cross-sections, where $\mathrm{x_F}$ is Feynman x defined [6]

5.2.3 The GENIE Simulation

GENIE is a C++ and ROOT [120] based simulation package created for modeling neutrino interactions in matter. We use GENIE version 2.6.2 for this analysis. Various interaction models are used for predicting the cross-section for different types of processes. We use the formalism derived by Lewellyn Smith, which is discussed in Section **??**, to model the CCQE cross-section. We use the dipole approximation for the axial form factor discussed in Section **??** and given in Equation **??**. This form is motivated by assuming an exponential distribution of weak charge, the Fourier transform of which has a dipole form. The simulation uses a value of $\mathrm{M_A}$ of 0.99 GeV, which is similar to values found by many previous experiments [69]. Here, $\mathrm{g_A}$ = -1.267, which we also discuss in Section **??**. We use electromagnetic form factors outlined by R. Bradford, A. Bodek, H. Budd and J. Arrington [121], which are commonly refered to as BBBA form factors. The psuedo-scalar form factors are found using the PCAC also discussed in Section **??**.

Backgrounds are described by several models. The Rein-Seghal model [122] describes resonant pion production, which is the biggest background for the analysis presented in this disserta-

tion. Deep inelastic scattering is simulated using the Bodek-Yang model [123]. Neutral current scattering is modeled based on work by R. E. Hendrik and L. Li [124].

Although some interactions in this analysis are on free protons, most interactions are on nucleons contained within a carbon nucleus. We model that nucleus uisng the Relativistic Fermi Gas (RFG) Model which is discussed in Section 1.4.6. Nucleons have a high momentum tail described by Bodek and Ritchie [75]. The RFGM enforces Pauli blocking by requiring that a nucleon involved in an interaction contain more than the Fermi Momentum in the RFGM, or 221 MeV/c for the case of carbon. Final state effects are also modeled, which involves interactions of the final state nucleon as it exits the nucleus. GENIE uses the INTRANUKE package for this purpose.

We generate events using the GENIE simulation by acquiring an energy and neutrino flavor from the beam simulation. Using a random number seed, we then generate a particular interaction based upon that random number seed and the predicted likelihood for the different interactions.

5.2.4 Simulating MINERνA

The simulation in MINERνA involves several steps. In the first step, we use Geant4 to simulate the behavior of the final state particles predicted by the GENIE simulation. This involves simulating the amount of energy deposited in each step for a given particle as well as modeling any multiple scattering or secondary interactions that may occur.

The second step of the simulation involves modeling the actual detector components. The energy deposits predicted by Geant4 are converted into a prediction of the number of photons generated in the scintillator. This includes accounting for Birks' Law which describes how the light yield from energy deposited in scintillator saturates for larger energy deposits [125]. The capture of light by the WLS fiber and its path to the PMT are also simulated. We model the quantum efficiency of the anode on the PMT, which converts a percentage of light from the WLS fiber into electrons that can be accelerated in each stage of the PMTs. We simulate the first two dynode stages of the PMT. The remaining 10 stages are modeled with a Gaussian distribution the mean of which is the average gain for a single stage of the PMT. A simulation of the electronics is also put into practice. This yields simulated hits that can be processed in the same way as hits in data.

5.2.5 The MINOS Simulation

Muons that pass out of the back of MINERνA and are not found to stop in ArgoNeuT are passed to the MINOS simulation. This is done by passing the position of entry, the type of particle, and the four-momentum of that particle to the MINOS simulation. The MINOS simulation uses GEANT3 to model the MINOS detector and the magnetic field present within that detector. This simulation runs separately from the MINERνA simulation as well as the MINERνA software framework.

5.3 HIGH LEVEL DATA PROCESSING

The same high level processing steps are employed for data and the simulation. Several steps of processing occur. These are outlined below.

5.3.1 Matching MINOS and MINERνA Data Sets

One of the earliest stages of high level processing is combining MINOS and MINERνA detector information. This includes associating MINERνA gates and MINOS snarls with each other. A MINOS snarl is the analog of a MINERνA gate. In the case of data, gates and snarls are matched using GPS timing information. In the case of the simulation, a given MINERνA gate and MINOS snarl are known to be associated *a priori*.

For a given MINOS snarl, we run the full MINOS reconstruction prior to gate and snarl matching. This reconstruction includes a MINOS track finding algorithm, which uses a Kalman Filter and accounts for multiple scattering and deflection due to the magnetic field.

5.3.2 Forming Time Slices

Given the fine timing resolution of MINERνA and the timing calibrations that we apply, most neutrino interactions have a narrow time profile. Since multiple interactions can occur within the detector, separating interactions by their time offers an effective way of disentangling interactions that would otherwise overlap in space. To do this, hit times are sorted using a Heap Sort [128], which is known to be an efficient method [129].

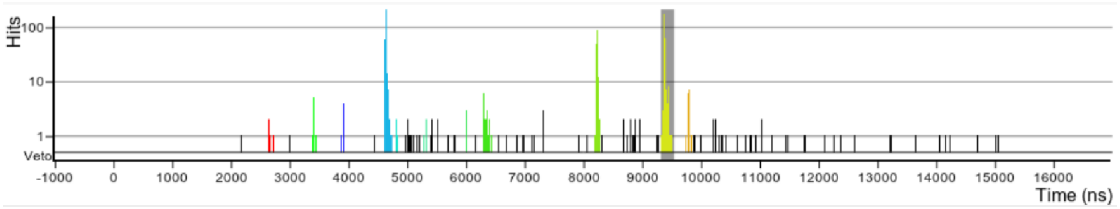

Figure 5.8: Histogram of hits as a function of time for a particular gate in data after it has been separated into time slices. The histogram comes from the Arachne event display [130]. Different time slices are represented by different colors while unused hits are depicted in black. Note that different peaks are correclty identified as unique time slices.

Once hits are sorted, a sweep begins to find concentrations of hits in time. If at least two hits with a minimum amount of charge associated with them are found within a particular window, the hits are grouped together as a time slice. Hits are then added to this time slice if they occurred close to the initial hits in the time slice. The length of time used for this window is driven by the integration time in the FEBs.

In this step, only hits that pass the discriminator threshold are used. After all such hits are considered, the remaining hits are then matched to time slices if they fall within the spread of times for a particular time slice. The time slice is then used as the basic unit in processing for the remainder of reconstruction. Figure 5.8 depicts all hits in a particular gate separated into time slices.

5.3.3 Forming Clusters

To form clusters, we look for groupings of hits directly adjacent to each other within a plane within a given time slice. Any space between hits leads to a new cluster being formed, where a space is a strip that did not register a hit. An isolated strip without neighbors that registered a hit is also promoted to a cluster. An illustration of clusters being formed from strips is shown in Figure 5.9.

A position is calculated for each cluster. The energy on each strip is considered and the energy-weighted position is then calculated using all hits contained within a cluster. A time is also found for a cluster, where the time from the hit with the most energy within the cluster is asigned as the cluster time.

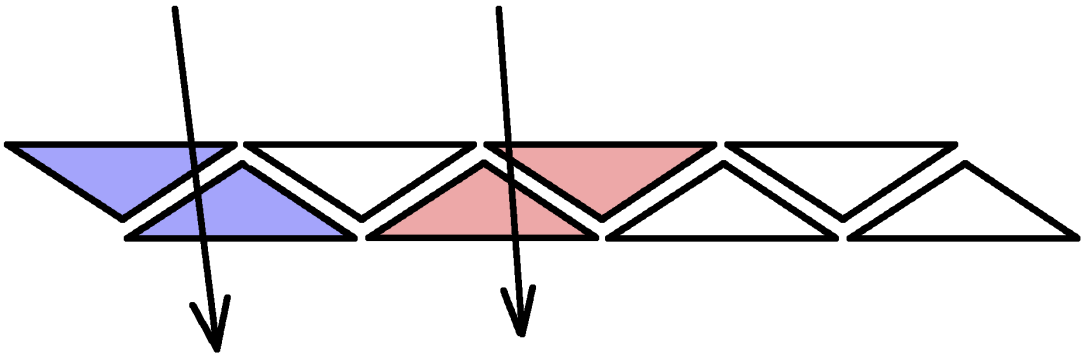

Figure 5.9: An illustration of clusters formed from MINERνA strips within a plane. Particles traversing the plane are depicted as black arrows. The strips that are traversed by the arrows are colored light blue and pink, which are intended to represent unique clusters. Two clusters are formed since a strip without a hit bisects them.

We classify the resulting clusters by their composition. We identify clusters as either low activity clusters, trackable clusters, heavy ioning clusters, superclusters, or cross-talk clusters. Clusters with less than 1 MeV are considered low activity clusters. The following requirements must be met for a cluster to be considered trackable.

- 1 MeV $\leq$ Total cluster Energy $<$ 12 MeV
- $\leq$ 4 hits
- Must have either one or two hits with hit Energy $\geq$ 0.5 MeV
- If two hits are present with hit Energy $\geq$ 0.5 MeV, they must be directly adjacent to each other

For a cluster to be considered a heavy ionizing cluster, it must meet similar criteria to trackable clusters.

- Total cluster Energy $\geq$ 1 MeV
- $\leq$ 4 hits
- Must have either one, two, or threes hits each with hit energy $\geq$ 0.5 MeV
- If two or threes hits are present with hit Energy $\geq$ 0.5 MeV, they must all be directly adjacent to each other
- Must not qualify as a trackable cluster

Heavy ionizing clusters are important in forming high angle tracks. Any cluster with more than 1 MeV in energy that does not meet the criteria for either trackable or heavy ionizing clusters is classified as a supercluster. Any cluster with five or more hits is automatically considered a supercluster.

A cluster is identified as a cross-talk cluster by inspecting the PMT pixels associated with hits within that cluster. The PMT pixels associated with that cluster are compared to PMT pixels associated with a particle interaction. If these cluster PMT pixels are found to be directly adjacent to the pixels related to the particle interaction, the cluster is considered to be a cross-talk cluster.

5.3.4 Tracking

Photons and charged particles generally deposit energy in each MINERνA plane they traverse. We identify these deposits and use them to reconstruct the particle trajectory. We refer to the resulting reconstructed object as a track.

The strategy we use for reconstructing tracks within a time slice involves first finding as many tracks as possible and out of those tracks identifying a muon track associated with a neutrino interaction. All other tracks are then deleted. Once the muon track has been identified, it can be further refined by picking up activity that may have been missed in the initial pass of tracking. The muon is identified first since it is one of the easiest particles in an interaction to find, removing activity associated with a muon generally improves the overall success rate of finding other tracks, and the start of the muon track is generally the vertex for the neutrino interaction that created the muon. After finding the muon we then search for any hadron tracks using the same tracking procedure we used to find the muon. We then attempt to connect events with a common vertex and then refit them using a Kalman filter [131, 132]. A search is then made for any other tracks from coincident activity within the event using the same tracking procedure as before. A description of the tracking algorithm used in each step follows below.

5.3.4.1 Making Track Seeds and Track Candidates The first step in the tracking process is making two dimensional track seeds. To make these seeds, we sort trackable and heavy ionizing clusters by their location along the Z-axis. Track seeds are then found by looking for clusters

within planes with the same view for three clusters that are in a line. A determination of linearity is made based on doing a least squares fit to a line and enforcing a minimum χ^2 value for the fit. Only tracks seeds that pass that linearity cut are considered in the next step of tracking. This process is illustrated in Figure 5.10.

Once we have created a set of track seeds, we combine track seeds into track candidates. We initiate this merging process in the downstream end of the detector and work upstream. This order is used since muons will generally traverse a large fraction of the detector and consequently are likely to be found by looking for tracks in the downstream end of the detector. Employing the reverse of this method by finding the vertex of the muon track and initiating the track from that point is difficult since high amounts of activity can be present near the vertex.

We combine track seeds by looking for track seeds that share a cluster and then comparing slopes of each. If the slopes are similar enough, the track seeds are combined into a track candidate. The result is two dimensional track candidates each composed of clusters in a single view. We then attempt to merge recently formed track candidates comparing the slope and slope intercepts of each. If the two are similar enough, we combine them into a single track candidate. When creating track candidates, we enforce that a track candidate contain no more than a single cluster per plane. The result is a number of track candidates each composed solely of clusters from a single detector view. An illustration of this is shown in Figure 5.11.

The next step of tracking involves taking two dimensional track candidates from different views and attempting to combine them into a three dimensional track. We first enforce that the tracks are colinear by cutting on the χ^2 value for a least squares fit of the three dimensional track to a straight line. We also check the amount of overlap in the Z-direction. If the track passes the χ^2 cut and sufficient overlap is found, the track candidates are combined into a track object.

We next check for tracks that have a kink. Occasionally, a particle can undergo a hard scatter resulting in a kink in two of the views while still appearing straight in the third view. In this case, overlap is inspected on each side of the kink separately. The two pieces on either side of the kink can then be formed into a single track object.

5.3.4.2 Kalman Filter We fit a track using a Kalman filter implementation that incorporates multiple scattering [131, 132]. The Kalman filter is a recursive method that takes input data to

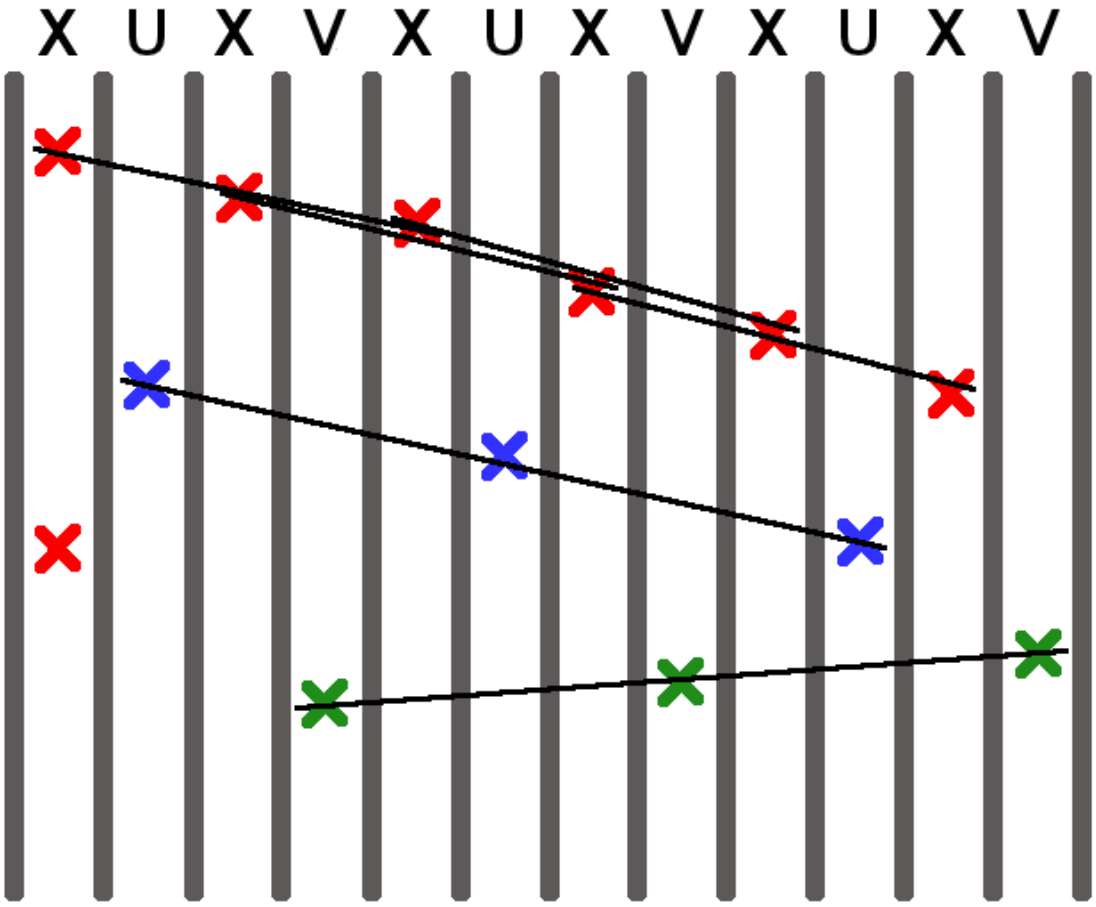

Figure 5.10: An illustration of track seed formation. Clusters are marked by a 'X' with a color that varies by plane type. Clusters within a particular view are formed into three cluster seeds. In cases where multiple tracking seeds are made, particular seeds may overlap. Some clusters cannot be used to successfully construct a track seed, such as one of the hits in the first X plane.

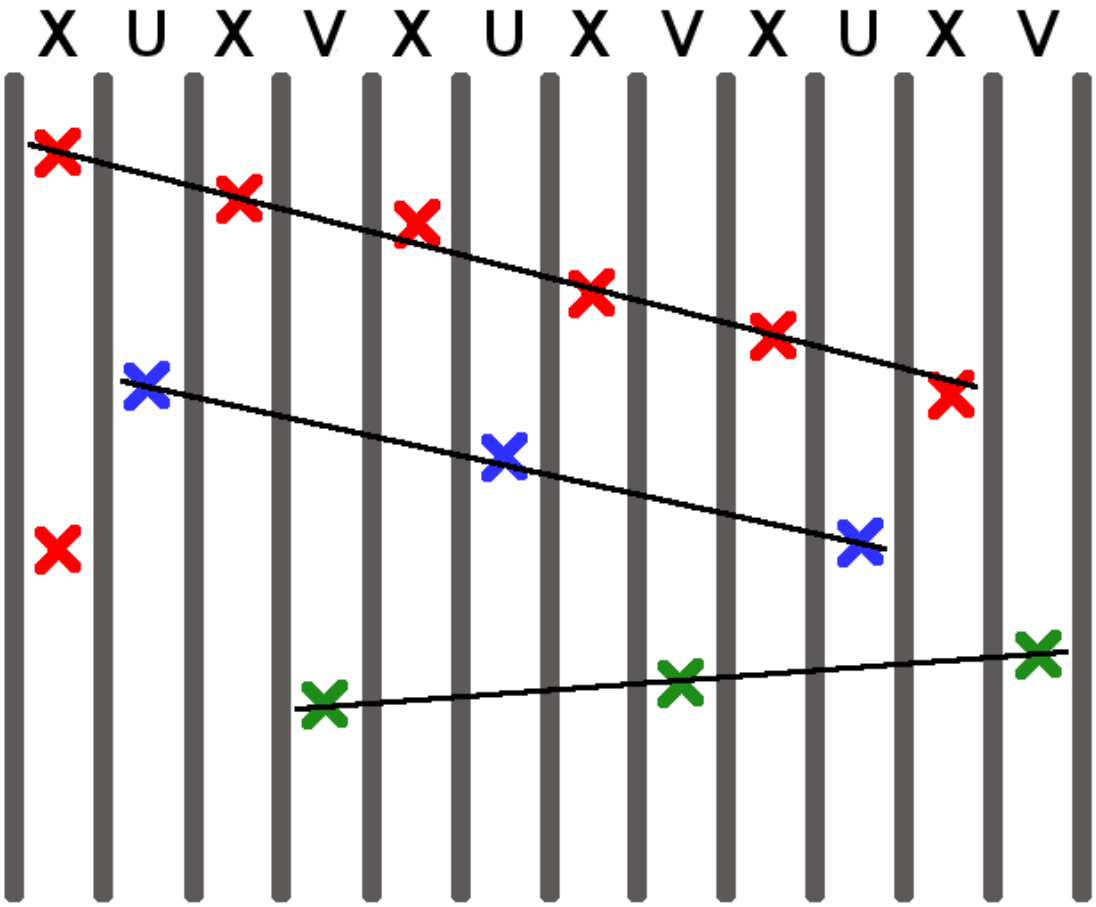

Figure 5.11: An illustration of track candidate formation. In the pictured scenario, track seeds in the U and V planes are promoted to track candidates. The track seeds in the X view are merged into a single track candidate.

make a statistically optimized prediction assuming a linear system which is then used as an input for the next iteration of the filter.

The multiple scattering calculation incorporates material information for the region of the detector the track is traversing as well as the mass of the particle. For the first round of tracking where we search for a muon track, we use the mass of the muon in calculating multiple scattering.

5.3.4.3 Using Track Projections to Extend and Populate Tracks We use the fit results to further extend and populate a track. This includes extending a track upstream and downstream as well as filling in any empty planes within the track object. For this procedure, we consider not just trackable and high ionizing clusters, but also low activity clusters and superclusters. For a particular cluster, we use the result of the Kalman filter fit for the location nearest the cluster in question. This gives local slope information and allows proper handling of multiple scattering. If this projection passes through any part of the cluster object, we prepare to add it the track. If a cluster is a low activity, trackable, or high ionizing cluster, we simply add it to the track. If the cluster is a supercluster, we break the supercluster into at least two pieces. One cluster consistent with a energy deposit from a minimum ionizing particle (MIP) in the path of the track is created. This cluster will have 2.25 MeV/cm of energy where the pathlength of the particle through a strip is considered in determining how much energy to allocate. The supercluster has the energy used to create the cluster for the track deducted from the relevant strips within the cluster. Note that if less than a MIP worth of energy is available, all energy in the path of the track is used to make the cluster that will be added to the track. In some cases, the supercluster is broken into three components one of which is added to a track.

This method accomplishes several important tasks. Filling in gaps on tracks helps ensure that energy that is properly associated with the track does not end up in the recoil energy calculation we make in Section **??**. The method ensures that the track is extended back to the true vertex of the neutrino interaction. The method also ensures the track is extended to the downstream end of the detector. This aids in correctly matching the track to a track in MINOS.

5.3.4.4 Track Cleanup After the above step of filling in gaps in tracks where possible, we inspect each track to determine if the object ought to be split into two pieces. Looser standards

regarding gaps along a track are initially used since some activity related to the track may be part of a supercluster and thus not available for forming a track. If no activity is found to fill in the empty spaces along a track, we find some tracks have large gaps of planes separating the upstream and downstream ends. If this gap is too great, we split the track into two separate pieces, considering them to be caused by separate particle interactions.

5.3.4.5 Applying the Tracking Algorithm As mentioned above, after reconstructing the muon track we search for hadronic particles. The track we consider most likely to be the muon is saved and all other tracks deleted. We then use the muon track as an anchor to find hadronic particles with the same vertex. We take the remaining trackable and high ionizing clusters and repeat the above tracking algorithm with the requirement that tracks must have a common vertex with the muon.

A Kalman filter fit is done to the track and vertex system. Any tracks that do not have a vertex consistent with the muon track are deleted. Track cleanup is peformed on the newly created tracks splitting them if large gaps exist within the track. We repeat this anchor-based tracking using the ends of all tracks as potential new vertices. We use the same tracking and anchoring method used for the muon track. After this search for secondary vertices, we search for tracks not associated with the reconstructed muon track. All remaining trackable and high ionizing clusters are used. Again, the same track procdure before is used, with a final cleanup step of splitting newly found tracks if appropriate.

5.3.5 Attenuation Correction

The size of the observed signal within a strip given a specific energy deposit by a traversing particle depends on the position along the strip that the particle interacted. The reason for this position dependence is the attenuation of light within the WLS fiber. Given a single hit within a strip and no other information, a correction for this attenuation cannot be made since there is no way to know where along the strip the hit occured. However, once tracks have been created, we know the three dimensional position of the various clusters that compose the track. Given the three dimensional information, we can account for the attenuation of signals that traveled longer or

shorter pathlengths. In earlier stages of processing, we calibrate cluster energy as if each one is in the center of the strip. For clusters where we have three dimensional information available, we calculate and apply a correction for how the signal differs from a hit that happens at the ceneter of the strip in the longitudinal direction.

5.3.6 Incorporating MINOS Reconstruction

We attempt to match MINERνA tracks that have a cluster in at least one of the last five modules in the detector to tracks in MINOS. The resulting object we refer to as a prong. To qualify as a match, the MINOS track must start within the first four planes of MINOS. We only consider matching MINOS and MINERνA tracks if they are within 200 ns of each other. Figure 5.12 shows the time difference between all matched tracks for Frozen Detector data. To make a match, we use a track projection method. We project the MINOS track across the two meters separating the two detectors to the plane that contains the last cluster on a MINERνA track and we project the MINERνA track to the plane that contains the vertex of the MINOS track. For MINERνA, we compare the position of the last cluster on a track with the projection of the MINOS track. We refer to the distance between these two points as the match residual. We also look at the analagous quantity in MINOS, where we find the residual of the projection from MINERνA and the vertex of the MINOS track. We look at the size of the match residuals at both faces to assess whether the two tracks are likely to have been created by the same particle. If both match residuals are less than 40 cm, we consider them to be matching tracks. If multiple potential matches exist, we take the match with the smallest match residual.

If no matches have been found for a MINERνA track, we also attempt matching using a closest approach method. We project the MINOS track toward MINERνA and the MINERνA track toward MINOS and look for the two tracks to cross close to a common point in space. This method can be useful for the case where ArgoNeuT is present between the two detectors. In that instance, a muon could undergo a hard scatter within ArgoNeuT and still potentially get matched. Figure 5.13 shows both match residuals and the result of the closest approach method.

The MINOS track has a charge associated with it which is found by examining the direction of curvature in the MINOS magnetic field. We use energy found by MINOS reconstruction. Energy

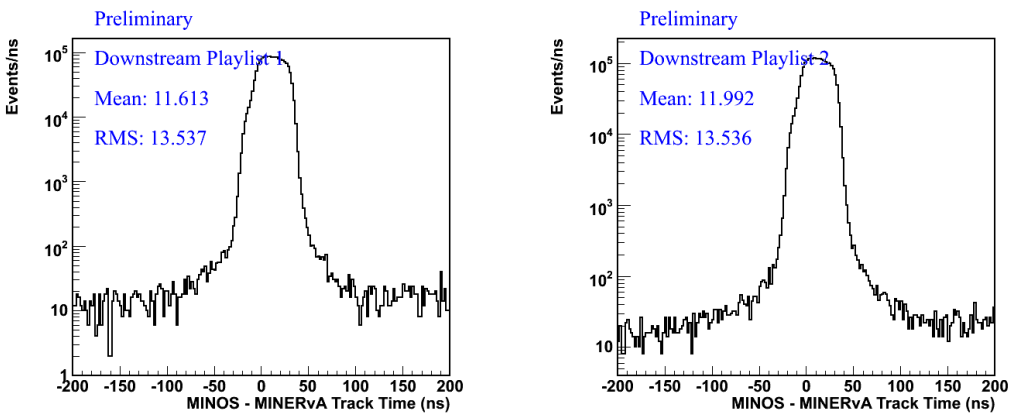

Figure 5.12: Plots of the time difference between matching MINOS and MINERνA tracks for the Frozen Detector data sets. The data set labeled as Downstream Playlist 1 is for the period where no construction was occurring and Downstream Playlist 2 is for data after the resumption of construction. Most events are sharply peaked close to 13 ns. Note that no correction is made for the time of flight of the muons.

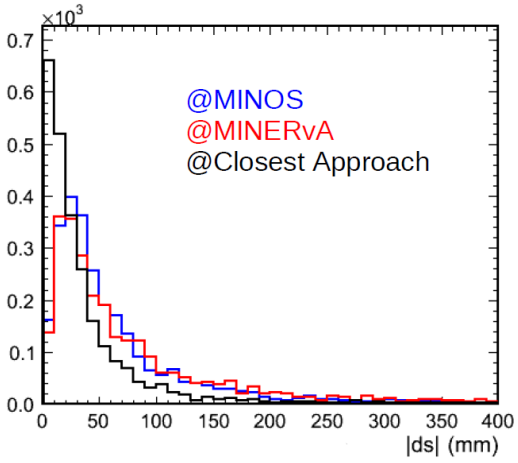

Figure 5.13: The match residual at the MINOS and MINERνA faces as well as the value for the closest approach method for matching tracks. This plot was made by M. Kordosky of the MINERνA collaboration.

can be found in one of two ways in MINOS. In one case, range of the track is used to estimate its initial energy. The curvature of the track in the magnetic field is also used to make an energy measurment. We use range or curvature for energy reconstruction depending upon where the track begins or ends. This includes whether the track passes into region containing non-instrumented planes, in which case we use curvature for reconstruction. If the track is contained within a particular volume that is fully instrumented, we use range for the momentum measurement. In all other cases, we use the result of the curvature measurement.

We find that tracks matched to a MINOS track are almost exclusively muons giving a high level of confidence to our particle identification for such tracks.

5.3.7 Muon Energy Reconstruction

As mentioned in Section 5.3.6, we use the MINOS reconstruction to find the energy of the muon while it is in MINOS. To find the energy of a muon at its vertex in MINERνA, we must account for the energy lost by that muon as it travels in the MINERνA detector. We also account for energy lost in the first steel plane of MINOS and the steel mirror plane at the backend of MINERνA. To account for this energy loss, we use the Bethe-Bloch formula [6] which gives the energy loss at each step,

$$-\frac{\mathrm{dE}}{\mathrm{dx}} = \mathrm{Kz}^2\frac{\mathrm{Z}}{\mathrm{A}}\left[\frac{1}{2}\ln\frac{2\mathrm{m_e c}^2\beta^2\gamma^2\mathrm{T_{max}}}{\mathrm{I}^2} - \beta^2 - \frac{\delta(\beta\gamma)}{2}\right], \tag{5.4}$$

where K is a constant, z is the magnitude of the charge of the incident particle, A is the atomic mass, Z the atomic number, I is the mean excitation energy, $\mathrm{m_e}$ is the mass of the electron, $\delta(\beta\gamma)$ is a density effect correction to ionization energy loss, c is the speed of light, and we use the relativistic variables β and γ. $\mathrm{T_{max}}$ is the maximum amount of energy that can be imparted to an electron [6], given by

$$\mathrm{T_{max}} = \frac{2\mathrm{m_e c}^2\beta^2\gamma^2}{1 + 2\gamma\mathrm{m_e}/\mathrm{M} + (\mathrm{m_e}/\mathrm{M})^2}, \tag{5.5}$$

with M being the mass of the particle for which $\mathrm{T_{max}}$ is being calculated. To apply this formula, we incrementally step along a track assessing the amount and types of material along it. Then starting from the downstream end of the track and using the energy found for the muon in MINOS where we account for steel between MINOS and MINERνA, we find the amount energy loss expected based on the amount of material at that point. This energy is then added on to the muon. This new

energy for the muon is used in the next calculation of the energy loss in the subsequent upstream step. This process is repeated until the energy of the muon has been reconstructed back to the vertex.

5.4 BLOB FORMATION

We reconstruct three different types of blobs: vertex blobs, isolated blobs, and dispersed blobs. Blobs are composed of clusters and are constructed to capture different types of topologies.

Vertex blobs capture all cluster energy near the vertex, specifically within a 10 cm sphere around the vertex of the muon. We consider trackable clusters, high ionizing clusters, and super-clusters, but not low activity or cross-talk clusters when creating this object. We use the same criteria for cross-talk clusters as Section 5.3.3.

We also construct isolated blob objects which are composed of contiguous areas of energy deposit. To find them, we look for clusters that are adjacent to each other in different views and that form a consistent three dimensional object. We consider all clusters except ones that contain less than 1 MeV of energy, cross-talk clusters, clusters that have a time more than 25 ns away from the track time, and any cluster in the OD or HCAL regions of the detector.

Last, we construct a dispersed blob which contains all clusters that are not associated with a track or that are part of a vertex blob or isolated blob. We consider the same classes of clusters for dispersed blobs as are used for isolated blobs.

6.0 CHARGE CURRENT INCLUSIVE USING ANTINEUTRINOS ON CARBON, IRON, LEAD AND SCINTILLATOR

This chapter describes an analysis of $\overline{\nu}_\mu$ charged current inclusive in the MINERνA scintillator tracker and most importantly charge current inclusive at the nuclear passive targets upstream of the scintillator tracker. The goal is the make a ratio of cross-section as function of Bjorken x of each nuclei (C-Pb-Fe) divided by the scintillator CH. The analysis is restricted to interactions with 2GeV$<E_\nu<$20 GeV and the muon theta angle θ_μ between 0^o and 17^o. The data used for this analysis were collected from October 2010 until February 2011. The total proton on target for antineutrino mode collected were 1.06x 10^20 P.O.T and fully used to make this ratio calculation. The analysis signal is defined as

$$\overline{\nu}_\mu + A \rightarrow \mu^+ + +X, \tag{6.1}$$

where A is a nucleus either it is carbon, iron or lear or any material in the tracker (composition defined in Tables 3.2) . The $\rightarrow$ symbol represents the primary neutrino-nucleon interaction leading to the recoil shower called X which is the remaining hadron and nuclear recoil other than the μ^+. The μ^+ is required to have a MINOS match which is another way of confirming the limitation of MINOS spectrometer. There is no requirement on the that recoil system.

6.1 EVENT SELECTION

Events are selected from 1.06×10^{20} protons on target of $\overline{\nu}_\mu$-mode[1]. A Charged current neutrino events are differentiated by the productions of a charged lepton in the final state. All selected events are required to have a μ^+, which tags charged current $\overline{\nu}_\mu$ interactions and that has a match in MINOS but no requirements on the recoil system. The primary constrains are related to vertex selection, vertices have to be within the passive targets materials for carbon-iron and lead and within the scintillator tracker for scintillator events. The geometry requirements are the same as the neutrino mode of this analysis that can be found at [21]

6.1.1 Muon Selection

A long track pattern recognition algorithm based on an implementation of the Kalman filter that incorporates multiple scattering is used to find long (more than 9 modules) tracks in the MINER?A detector. Long tracks found in MINERνA are then projected into the MINOS near detector in an attempt to find a matching MINOS track. If found, both tracks, the one in MINERνA and the one in MINOS, are merged and called a MINOS match track. All MINOS match tracks are assumed to be muons. The interaction′s reconstructed vertex is located at the beginning of the muon track. Figure 6.1 shows a charged current event with a fully reconstructed muon using the MINERνA event display. The track curvature in association with the magnetic field produced by MINOS magnetic coil allows the reconstruction of the muon charge and energy. The energy of muons that stop in the MINOS near detector can also be reconstructed by the range method that uses the Bethe-Bloch equation [[137]] to calculate the total energy loss during the passage of the muon trough the MINERνA and MINOS detectors. The muon energy resolution is 10% for muons reconstructed by curvature and 5% when reconstructed by the range method. Muons that do not reach MINOS, either because they exit at a high angle or stop in the MINERνA detector, can not have the charge reconstructed and are not used in this analysis. It is hard to differentiate muon from pions if there is no MINOS match, so it is not used for this analysis. A muon is identified as a single track that exits the downstream end of MINERνA and is matched to a reconstructed track in the MINOS detector.

[1] In $\overline{\nu}_\mu$-mode, the NuMI focusing magnets focus negatively-charged mesons, resulting in a $\overline{\nu}_\mu$-dominated neutrino beam.

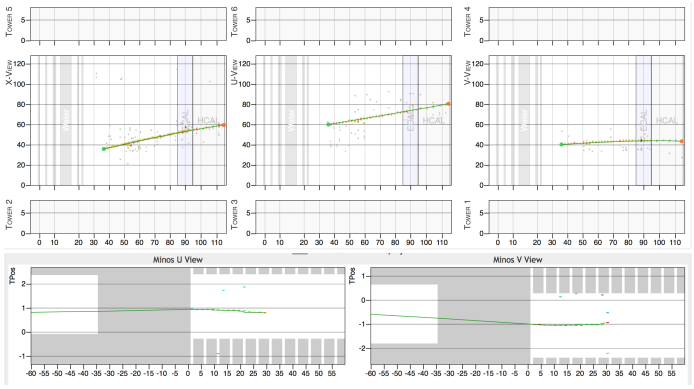

Figure 6.1: a charged current neutrino event in the tracker region with a reconstructed positive muon exiting from the back (reconstructed track is shown as a green line) in the three views of the MINERνA detector. Bottom: the same event whose muon is exiting MINERνA and entering MINOS. This muon has been reconstructed by both detectors and the resulting tracks merged.

The MINOS-matching requirements are described in Sec. **??**. This analysis requires exactly one MINOS-matched muon track attached to the interaction vertex which are already assume to start of one of the passive materials. Having that MINOS match will allow a charge and momentum analyze of the muon to differentiate from μ^+ to μ^-.

In addition to the track selection, this analysis requires that the reconstructed muon charge significance, q/p, is more than zero. This selects positive-charged muons, corresponding to a charged current $\overline{\nu}_\mu$ interaction.

6.1.2 Rock muon contamination

Neutrinos interact quiet often with the underground rock and produce muon that enter the front of the detector and exit MINERνA by having a MINOS match. These rock muon may be very useful in calibration process as well as calculation of overall detector efficiency but their are considered as contamination for this analysis. Since rock muons are final state muons externally produce outside of MINERνA, they are removed by just requiring the vertex of the events of interest to be within the detector, in this case, events vertex from carbon-iron-lead or the active tracker region. Vertex

requirements are fully described at 6.1.4

6.1.3 Muon acceptance

Due to geometrical position between both detector MINERνA and MINOS and the tracking threshold of MINOS(unable to track muons with momentum less than 150 MeV/c [**?**]). Because MINERνA is located upstream of MINOS and is smaller compare to MINOS, the μ^+ from antineutrino scattering occurring inside MINERνA with larger scattering angles are less likely to have a MINOS match. The more the vertices are upstream of MINERνA which mean far from MINOS, the lower the angular threshold for acceptance is. With respect to the beam direction and to perform adequate measures of events coming from the nuclear targets upstream of MINERνA, the analysis is restricted with muon angle less or equal than 17^o. The MINOS-match requirement imposes strict limits on the muon acceptance. muon acceptance as function of the angle, and the z position but especially the energy of the neutrino has been perfumed and details on section.

This analysis requires a signal event to have a minimum neutrino energy of 2 GeV and a maximum energy of 20GeV, which implies a range of muon momentum with adequate acceptance of 0.2 to 1.2 GeV/c. Muons that originate near the upstream region of the detector will lose more energy through dE/dx processes and thus have a higher momentum threshold. The MINOS tracking efficiency for muons entering the front plane of MINOS is shown in Table 6.1.

Only events with $2 < E_\nu < 20$ GeV are used in this analysis. The lower limit implies a minimum momentum for the muon, which ensures adequate acceptance. Cutting directly on the muon momentum is not done because it would complicate the calculation of cross sections as a function of the neutrino energy. The upper limit is used because a selection of very high energy ν_μ events will have a larger contamination of $\overline{\nu}_\mu$ events. This decrease in ν_μ purity occurs because the flux at these higher energies consists of many neutrinos produced by the decay of unfocused mesons, which have not been charge-selected.

6.1.4 Vertex Selection

A nuclear target can be one of the 5 solid passive targets or a group of tracker modules. MINERνA tracker region have been heavily studied. The event vertex of the fiducial volume which define as a

Momentum Bin Low Edge (GeV/c)	0.00	0.15	0.25	0.50	0.75	1.00	1.25
Efficiency	0.00	0.55	0.60	0.60	0.80	0.90	1.00

Table 6.1: Approximation of MINOS tracking efficiency for muons that enter the front of MINOS as a function of momentum. Efficiency is the fraction of muons entering the detector that are tracked [**?**].

regular hexagonal area with apothem 850 mm. This ensures that the event did not occur in the lead of the electromagnetic calorimetry that surrounds the perimeter of the detector. The areal cut also restricts the fiducial area to a region where the acceptance into MINOS changes less rapidly than at the outer edges of the detector. Scintillator events are those with a vertex in the fully active central tracking region.The fiducial volume consists of modules 27–80, inclusive.The full tracking region spans modules 23–84 but there is limitation of the fiducial region to modules 27–80 provides a sufficient buffer to eliminate events originating in the iron and lead of the passive targets region (upstream of tracker), and lead of the electromagnetic calorimetry (downstream of tracker).

o select events on carbon, iron or lead, the requirement on z which is the longitudinal position is the primary cut. The vertices are required to be identifies occurring on target 2-3-4 and 5. Since these planes of passive targets contains multiples nucleus as described on 3.1.2.1 except for target 4 which is composed only by a thin liar of lead, a transverse position is then needed to differentiate the nucleus within the target assembly with which the interaction occurred. In contract of the active target in which the collect of deposition of energy is obvious, a passive target is a passive material from which no direct deposit of energy can be observed. The collect of energy recorded come from the first module of scintillator downstream of the passive target. When only one track is reconstructed, which is usually the μ^+, the events from the passive material can not be distinguished to the events originating from the scintillator downstream. Events that have a vertex in the module downstream of a passive target are assumed to be from the passive target. Because the passive targets are more dense than a scintillator module, this assumption is usually correct. (6.3) This selection also allows interactions actually in the scintillator, and

the procedure for substracting the contribution from these scintillator events is described in Sec. 6.1.6. If indeed the events truly occurs in the target assembly, the muon track is projected along its trajectory using a Kalman filter [**?**]. The muon energy is adjusted using dE/dx for the material traversed according to the propagation. More than one track can be reconstructed, if two or more are reconstructed, a fit is apply to find the three-dimensional vertex which may be inside the passive material (Fig. 6.5). However, the resolution of the vertex reconstruction is not sufficient to prevent smearing of scintillator interactions into passive material, and vice versa. The same selection criteria are applied to events with fitted vertices and one track events. Any gains in purity by applying a stricter criterion would be more than compensated by loss of efficiency, because there are a significant number of interactions in passive material whose vertex is reconstructed in scintillator. The selection criterion for passive target events is that the vertex is between one plane upstream and one module downstream of the target. The selected event sample of each target is roughly 70% one track, 10% fitted vertices in the target, 20% multi-track events that do not have a vertex in the passive target. Figure (6.2) shows number of events from each vertex type.

1. One Track The vertex has only one outgoing track so a fit is not possible.
2. Exact fit is where he vertex has more than one outgoing track and has a good fit. The vertex position is exactly in the passive nuclear target material.
3. Nearby Fit The vertex has more than one outgoing track and has a good fit. The vertex position is between the first plane upstream of the nuclear target or the second plane downstream, but it is not exactly in the passive material.
4. Bad Fit The vertex has more than one outgoing track and has a bad fit. ...

The transverse position of the vertex is compared with the orientation of the carbon, iron, and/or lead of the target assembly. e.g. for targets with multiple nuclei, the vertex is in the area occupied by iron, the event goes into the iron sample. The vertex is required to be more than 2.5 cm away from any seams between the passive materials (e.g. where iron meets lead). There is welding and some overlap of different materials at the seam, which would lead to ambiguity in the assignment of interaction nucleus. This requirement also serves to reduce the number of events with misidentification of interaction nucleus due to transverse smearing to the point where this background is negligible. This is the same procedure found at the Ref. ([21])

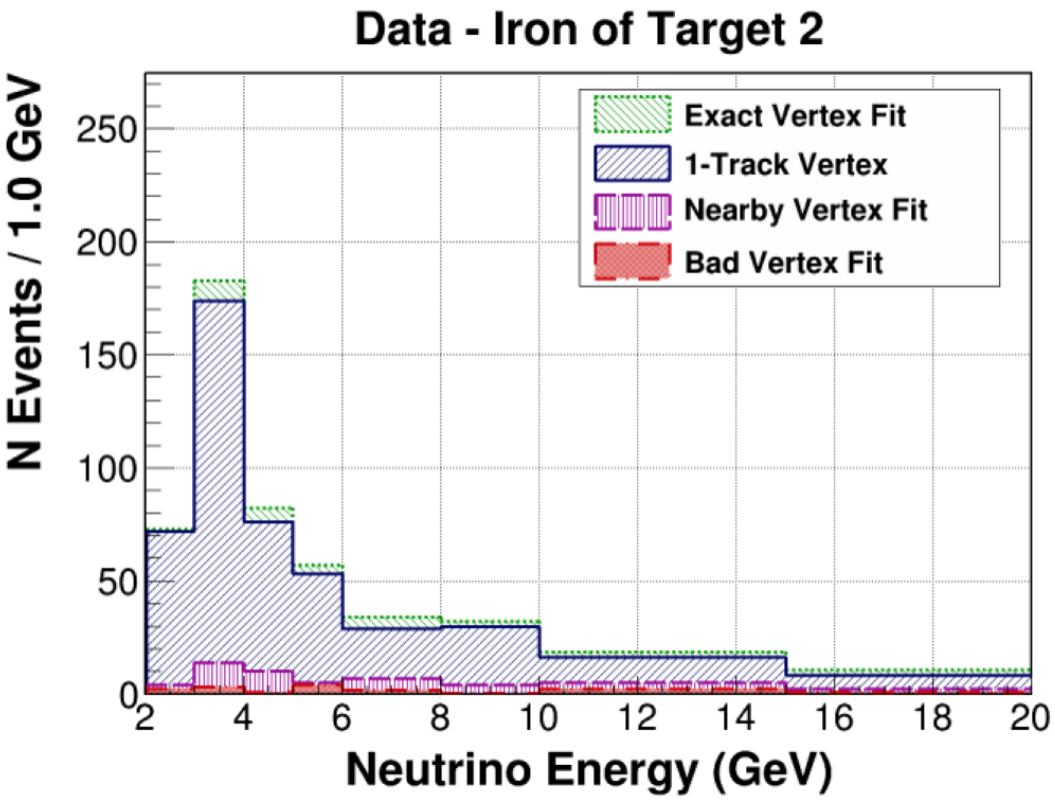

Figure 6.2: Number of events from each vertex type in Data for target 2

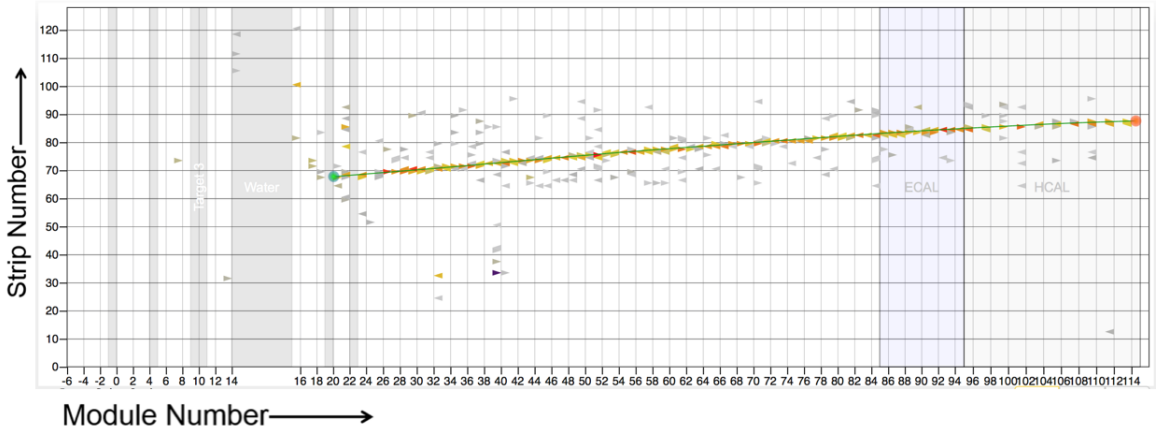

Figure 6.3: A data lead of target 4 event candidate with only one reconstructed track (run 2776-subrun 42- gate 120 slice 4). The beam enters from the left and MINOS sits to the right of the event display. Passive targets are shown as shaded rectangles in the upstream region of the display. Only the x view is shown. The reconstructed vertex is in the first plane downstream of the passive lead target.

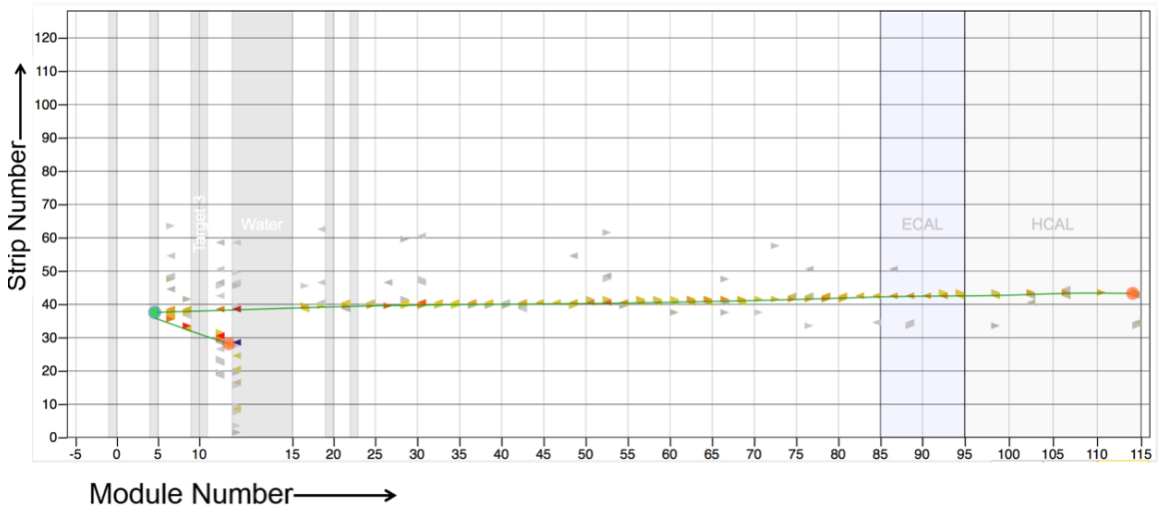

Figure 6.4: A data iron of target 2 event candidate with 2 reconstructed tracks (run 2459-subrun 12- gate 110 slice 1). Only the x view is shown. The reconstructed vertex is in the fitted to a 3D vertex in iron of target 2.

6.1.4.1 Scintillator Faux Targets The passive nuclear targets are segmented in the transverse direction into different materials, as shown in Fig.3.5. Throughout this analysis, sections of tracker are used as references for these target sections. A *faux target* is defined as the scintillator contained in a group of 6 contiguous tracker modules within a transverse region similar to the passive target section being referenced. ([21]) For example, one faux target for the iron of Target 2 is the transverse area of modules 27–32 that resembles the iron of Target 2. The first faux target begins with module 27; the last ends with module 80.

6.1.4.2 Number of Scatterers Table 6.2 shows the mass and target number of the fiducial regions.

Being able to differentiate and identify the correct interaction nucleus is crucial for this measurements so to ensure the reliability of the reconstruction vertex, event with poor reconstruction are rejected. All events with vertices classified as bad in the list above are through away. In oder to rejecting bad reconstructed vertex, a proper tracking of the muon is required. In some case, muon

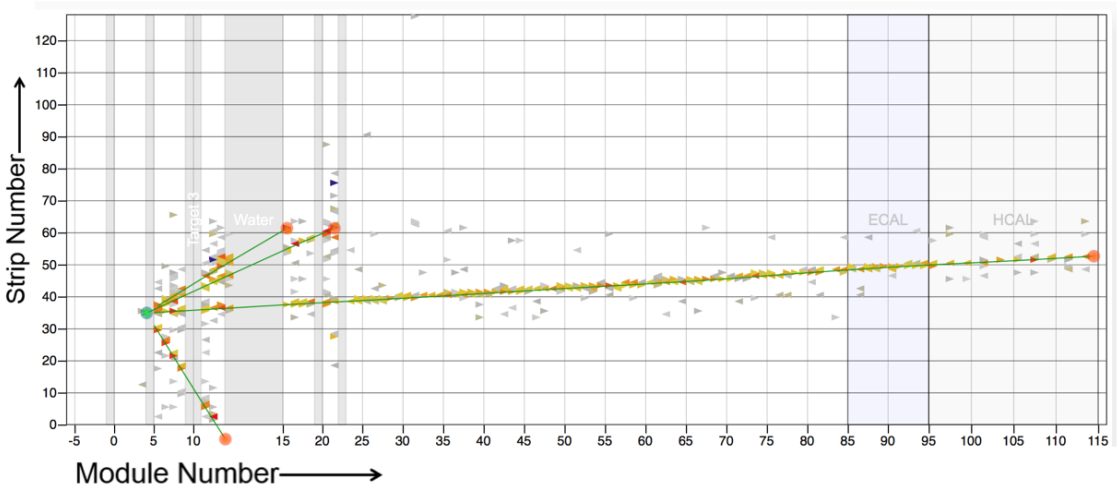

Figure 6.5: A data iron of target 2 event candidate with multiple reconstructed tracks (run 2930-subrun 52- gate 90 slice 3). Only the x view is shown. The reconstructed vertex is in the fitted to a 3D vertex in iron of target 2.

Nucleus	Mass (ton)	N Protons (E30)	N Neutrons (E30)	N Nucleons (E30)
Carbon	0.159	0.048	0.048	0.096
Iron	0.628	0.176	0.203	0.379
Lead	0.711	0.169	0.258	0.427
Scintillator	5.476	1.760	1.534	3.294

Table 6.2: Mass and number of scatterers in the fiducial volume of each target material.

Target	N Carbon	N Iron	N Lead	N Scintillator
Total	692	1923	2342	32485

Table 6.3: Neutrino events selected in the carbon, iron, lead, and scintillator charged-current sample.

track overlap with hadronic system, which can cause hits generated by the muon near the vertex to not be accounted as energy deposited by the muon. In such events, the muon is tracked starting from the downstream end and stops short of reaching the interaction vertex. A similar topology occurs when one or more scintillator planes traversed by the muon fails to record hits. Readout inefficiency may happen due to dead time or dead channels. The procedure for identifying all of these problems is to look for muon-like activity that is upstream of the vertex. Events were rejected if they fit any of the following criteria:

- Hits were recorded in eight or more planes in the muon's projected upstream path, and the average energy of the hits was between 1.5 and 6.5 MeV per plane.
- Hits were recorded in six or more consecutive planes in the muon's projected upstream path, and the average energy of the hits was above 1.5 MeV per plane.
- More than one TriP-t associated with strips upstream of the muon track were dead. This indicates that some activity associated with the track may not have been observed.

6.1.5 Selected events

By applying these requirements, the following charge current event samples are summarized on the table 6.3.

As function of neutrino energy which is the sum of muon energy and hadronic energy, distribution of the selected charged current events $\overline{\nu}_{\mu}$ are shown on Figure 6.7. Data are represented with the black dotes including with the statistical uncertainty and the monte carlo simulation is split into stacked histograms based on the interaction type as follows:

- CC-QE — blue — Charged current quasi-elastic.
- $W < 1.3(\text{GeV})$ inelastic — Orange — Resonances with low invariant mass.
- $1.3 < W < 2(\text{GeV})$ — red — The transition region from resonance to deep inelastic scattering.
- $Q^2 < 1(\text{GeV}/c^2), W > (2\text{GeV})$ — light purple — Not-so-deep inelastic scattering (non-perturbaitve DIS).
- $Q^2 > 1(\text{GeV}/c^2), W > (2\text{GeV})$ — violet — Safe deep inelastic scattering (DIS).
- Neutral current
- Neutrino wrong sign events

The simulation has been area-normalized by the number of events which pass the event selection. The following distribution are shown with area normalization

- Area Normalized: the MC shape normalization

$$\frac{N_{data}}{N_{MC}} \tag{6.2}$$

where N_{data} is the number of events in data and N_{MC} the total number events of MC simulation regardless the interaction type.

6.1.6 Backgrounds

Since the channel of interest is charge current inclusive for antineutrino interaction without requirements on the hadronic system, the primary excepted background are neutral current events. Wrong sign remaining ν_μ are also accounted as background. Rock muons as well are classified as background and the large contribution of background are the event reconstructed with the wrong nucleus. A wrong sign (WS) event can be falsely accepted in the event sample when a ν_μ charged-current interaction produces a muon whose charge is reconstructed as positive which is very small ($< 0.4\%$). Neutral current (NC) events do not produce a charged lepton in the final state.The NC background also is very small ($< 0.1\%$). Figure 6.10 shows the fraction of these background presented into log scale value. Misidentified nucleus are found when selecting events from passive targets due to contamination from scintillator. The fractional contribution of the scintillator background is roughly proportional to the ratio of areal mass of the passive target to nearby scintillator,

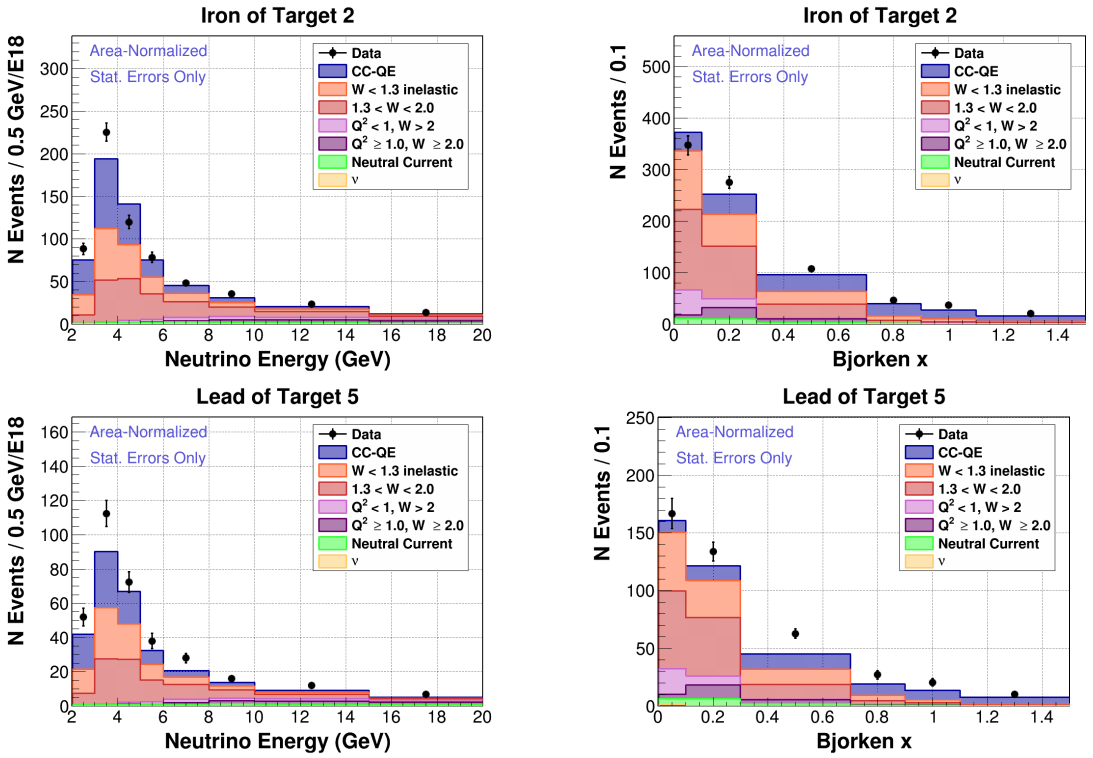

Figure 6.6: Kinematic distributions of selected events for iron of target 2 and lead of target 5

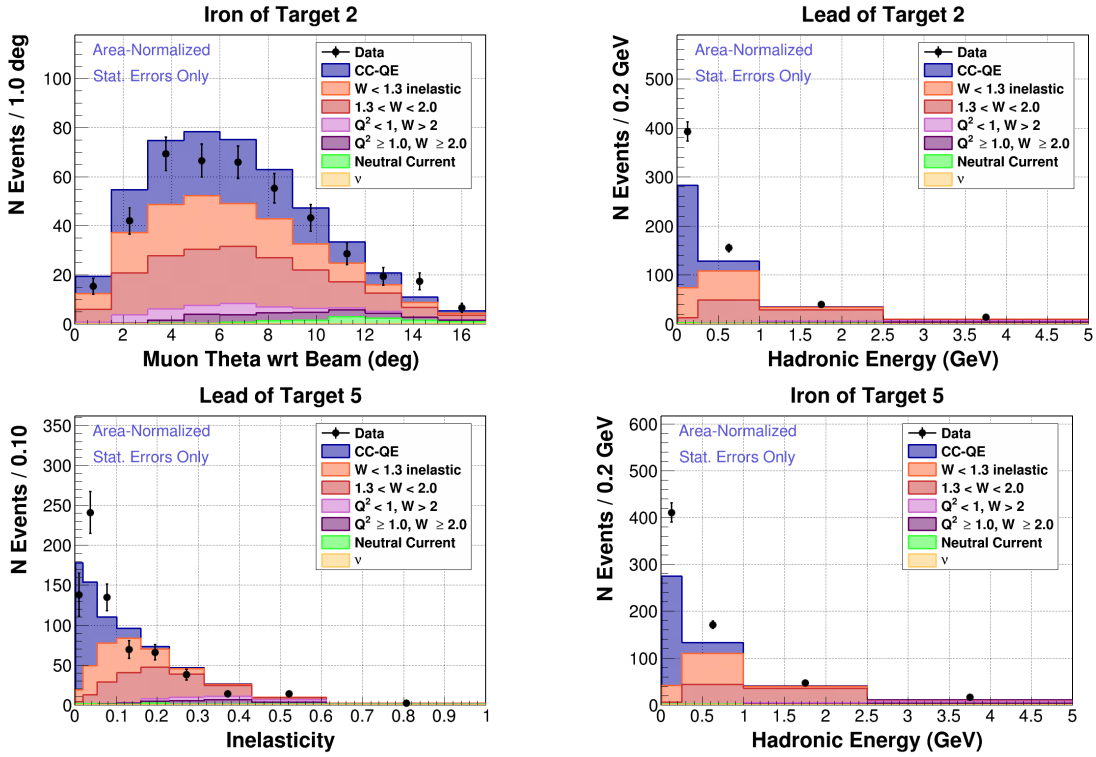

Figure 6.7: Kinematic distributions of selected events for iron of target 2 and lead of target 5 as function of inelasticity and hadronic energy

which has a range of 20–40%.

Figure 6.8 shows MC predictions for the backgrounds from misidentified nucleus for the iron of Target 2. Figure 6.9 another way of looking at the vertex origin using MC.

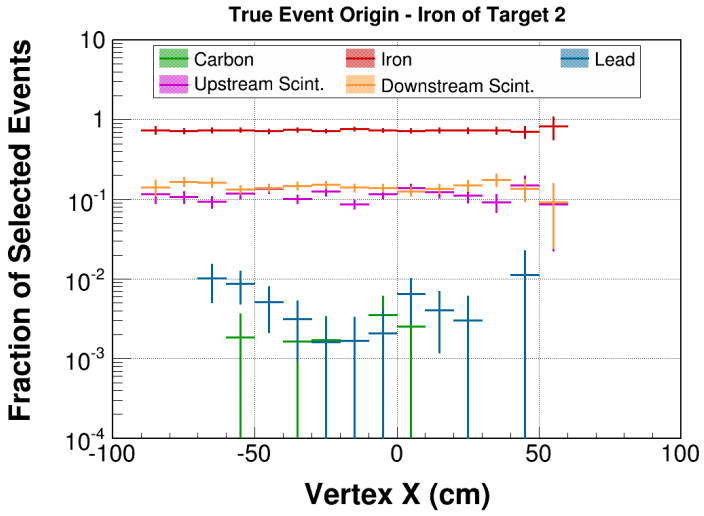

Figure 6.8: MC prediction for the fraction of events in the Target 2 iron sample that has a true nucleus of interaction in carbon (green), iron (red), lead (blue), and scintillator (purple and orange).

6.1.7 Substract plastic backgrounds

The background that has to be extracted in the plastic background as shown in two different ways on Figure 6.8 and Figure 6.9 since the goal is to make a measurements of cross-section of passive targets only. The tracking and nuclear target regions occupy different areas, and, therefore, have different acceptance into MINOS .The data-driven background substraction procedure described below uses efficiency and acceptance corrections from two separate MC samples to minimize systematic uncertainties. This method has been used for the neutrino mode analysis and has been successful on substracting plastic contamination. The following steps has to be followed. From [21]

- Since there is many data on the active scintillator of MINERνA, a sample of that scintillator events is selected from the data using the procedure described in Sec. 6.1.

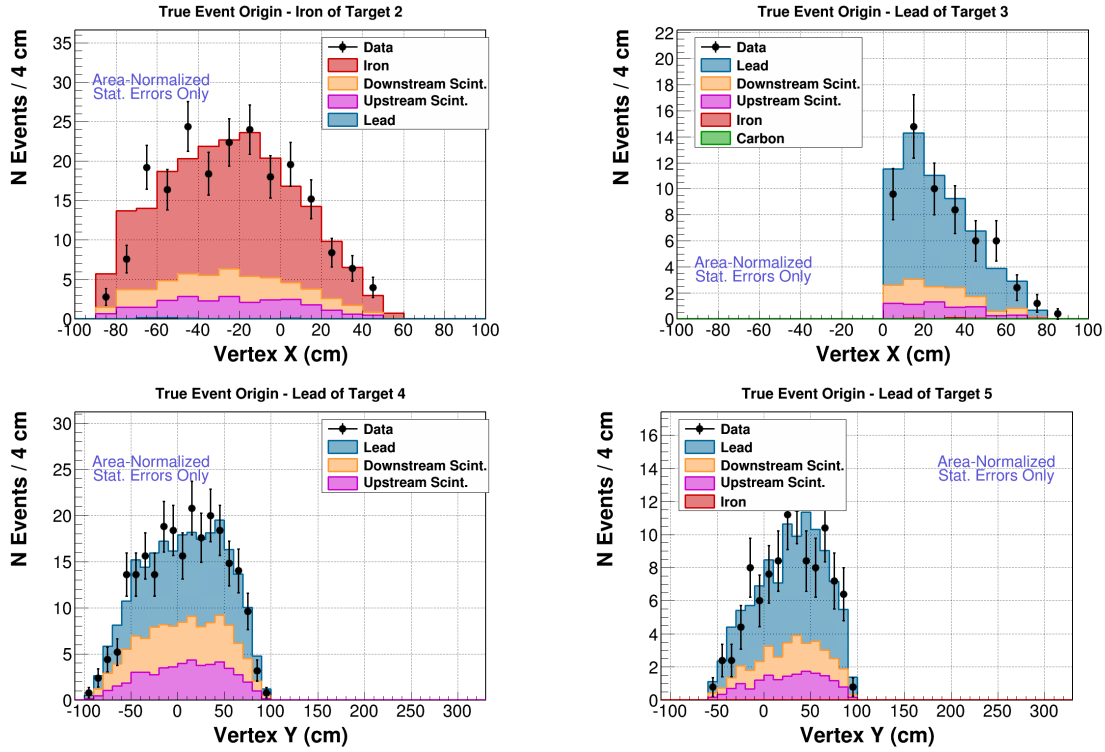

Figure 6.9: MC prediction fColored histogram stack shows the true vertex material

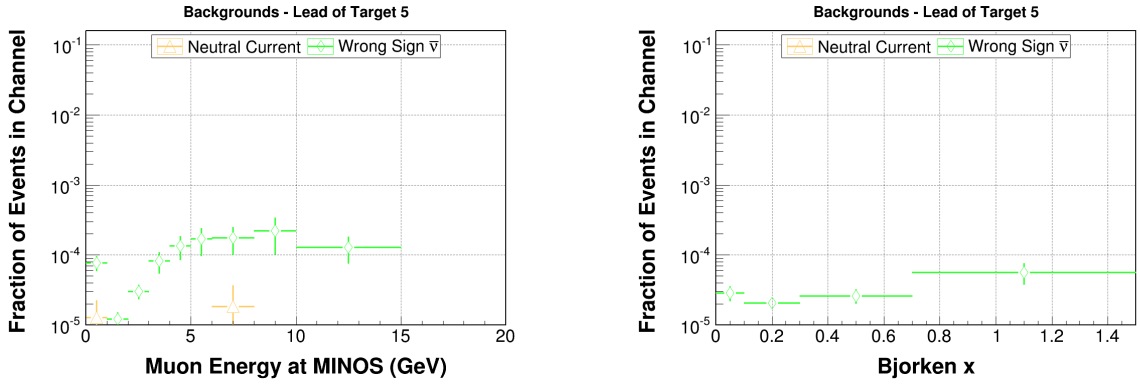

Figure 6.10: MC prediction for the fraction of neutral current and wrong sign events in the lead sample from Target 4.

- Next, the difference in geometric acceptance between events in the tracking region and events in the passive targets is accounted for using a muon-only MC. The location of the vertex within MINERνA affect the acceptance which the fractions of muons with a given energy and position that enter in MINOS. Figure 6.12 a slope on the tracker sample which is mainly due to detector acceptance. The acceptance in calculated at points every 200 cm in the longitudinal direction, 5 cm in the transverse directions, 0.2 GeV in muon energy, and 1in muon polar angle. At each of these points, three muons are generated at each degree of ϕ for a total of 1080 muons. The muons has to reach the back of MINERνA and exit from the regular hexagon with apothem 1.07m which is the inner detector but not at the side which are the calorimeter. The muons are required to make it until MINOS with at least 60cm distance from the first plan of MINOS. The muon must have sufficient momentum when it enters MINOS. MINOS tracking efficiency weight is applied. Figure 6.11 shows the fraction of accepted muons that fulfill the previous requierements, the distribution shows different targets with very distinct location, with theta angle varying from low angle of $\theta_\mu = 3^\circ$ to mid angle of $\theta_\mu = 6^\circ$ and high angle of $\theta_\mu = 12^\circ$. The energy of the muons for these plots are all 3 GeV Acceptance falls in regions that are far from the MINOS fiducial area, which is generally the outer edges of MINERνA. The fiducial region of MINOS is most apparent in the plots at $\theta_\mu = 6^\circ$ in the upstream region (middle left) and $\theta_\mu = 12^\circ$ in the downstream region (lower right).

- The deposition of energy within a passive targets such as carbon- iron and lead are different, a correction on hadronic energy also need to be added. efficiency differences that depend on the hadronic energy are accounted for using simulated neutrino events to derive an efficiency correction.

- Finally, the efficiency-corrected distribution is scaled so that the integrated number of events in the true background and predicted background are equal. The accuracy of the plastic background prediction as function of energy for lead of target 4 is shows as example. Figure (6.17)

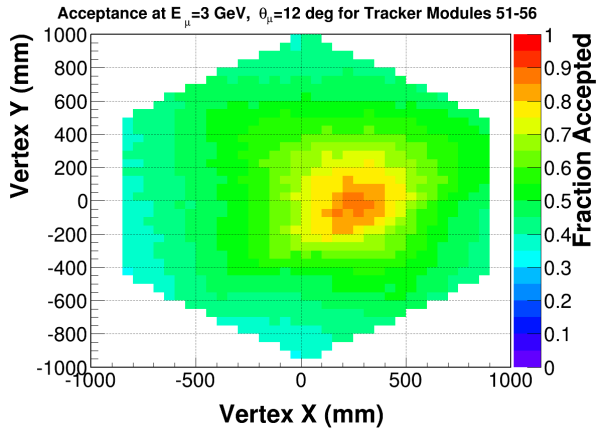

(a) $\theta_\mu = 12°$, 7.3m from MINOS

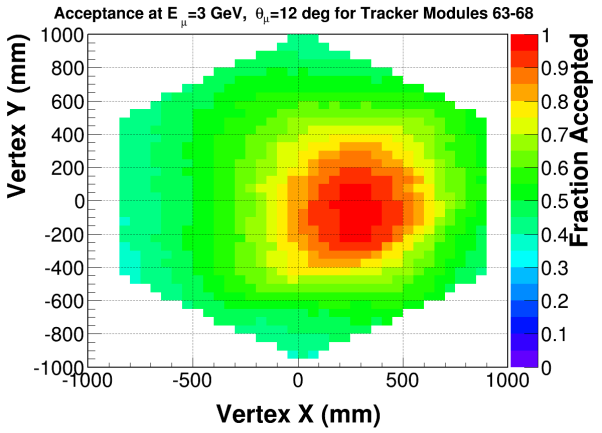

(b) $\theta_\mu = 12°$,, 4,2 m from MINOS

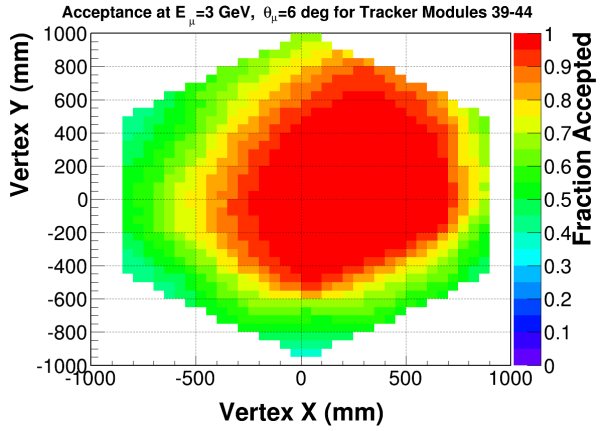

(c) $\theta_\mu = 6°$,, 6.4 m from MINOS

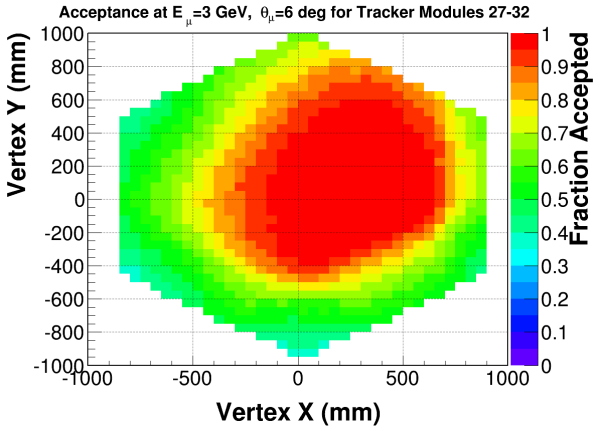

(d) $\theta_\mu = 6°$,, 3.4 m from MINOS

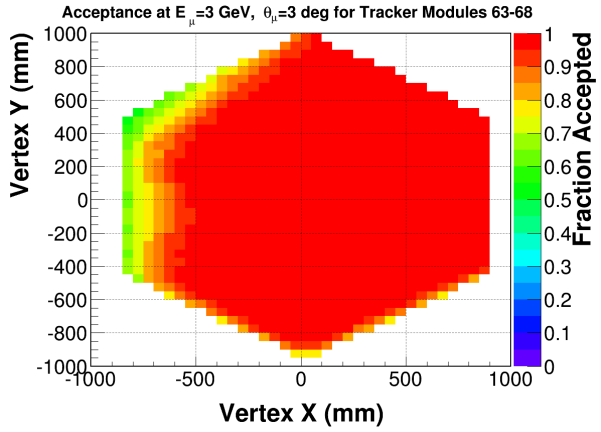

(e) $\theta_\mu = 3°$, 6.4 m from MINOS

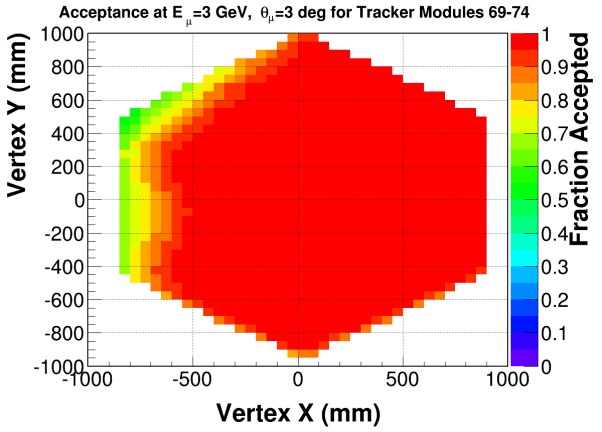

(f) $\theta_\mu = 3°$, 3.4 m from MINOS

Figure 6.11: Muon acceptance as a function of transverse position shown for two longitudinal regions of the detector and three angles

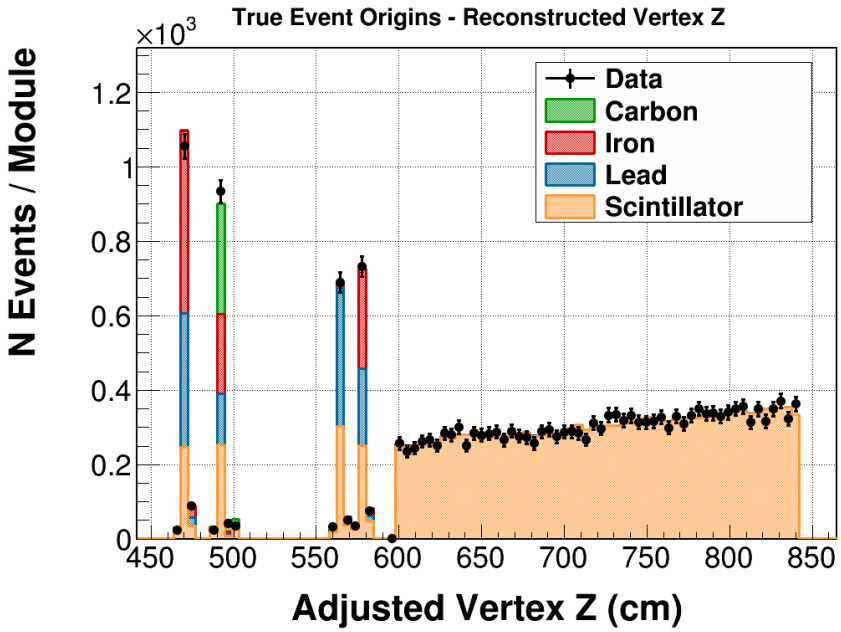

Figure 6.12: Distribution of the z coordinate of the vertex showing misidentification of the interaction nucleus. Data is shown in black points with statistical error. The MC event sample is shown as stacked histograms which are color-coded by the true interaction nucleus. Passive carbon, iron, and lead targets are located at the large spikes in the nuclear targets region (450–600 cm). The upward slope throughout the tracker region (600–840 cm) is an effect of the acceptance in MINOS. The number of MC events in each target has been scaled to the number of data events. The error bars of the data are due to statistical limitation.

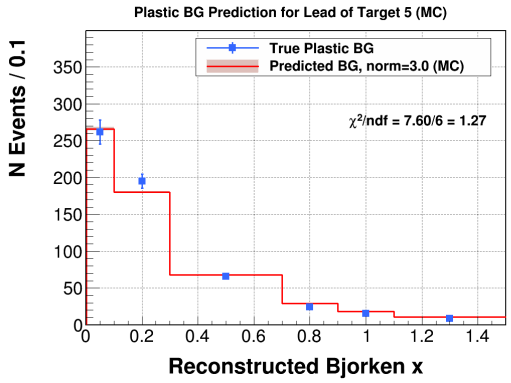

(a) Background as function of the x_{bj} for lead of target 5

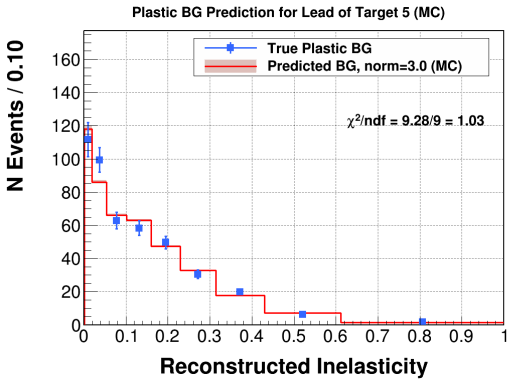

(b) Background as function of the y for lead of target 5

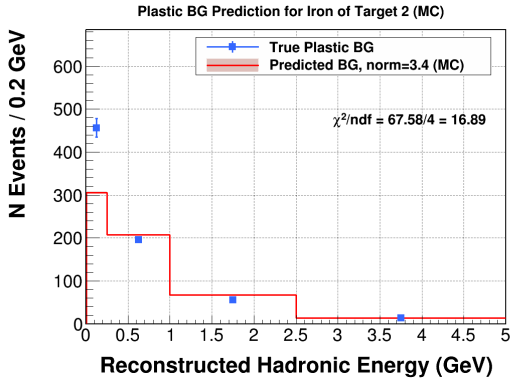

(c) Background as function of the hadronic energy for iron of target 2

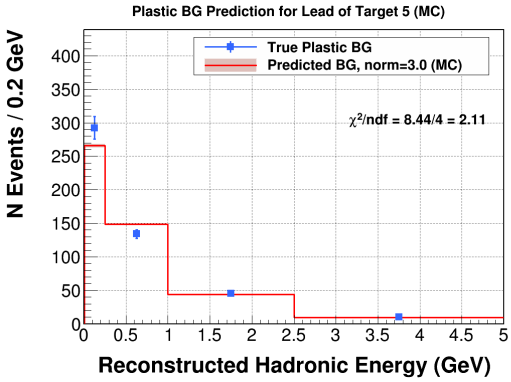

(d) Background as function of the hadronic energy for lead of target 5

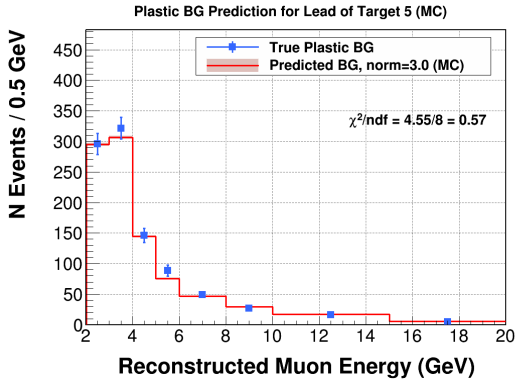

(e) Background as function of Emu for lead of target 5

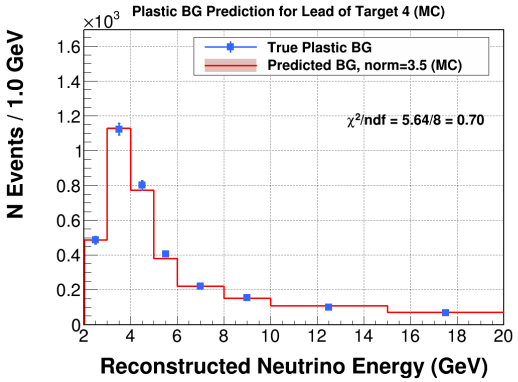

(f) Background as function of Enu for lead of target 4

Figure 6.13: Plastic background prediction compare to true background as shown by the MC,correction on hadronic energy is applied

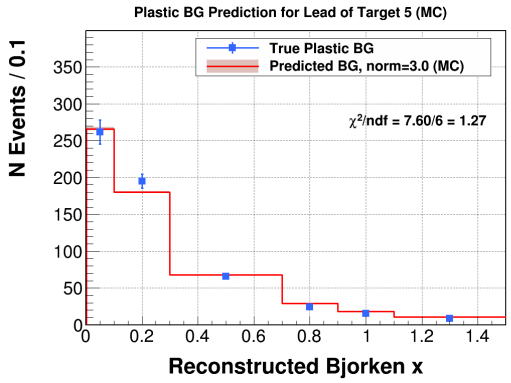

(a) Background as function of the x_{bj} for lead of target 5

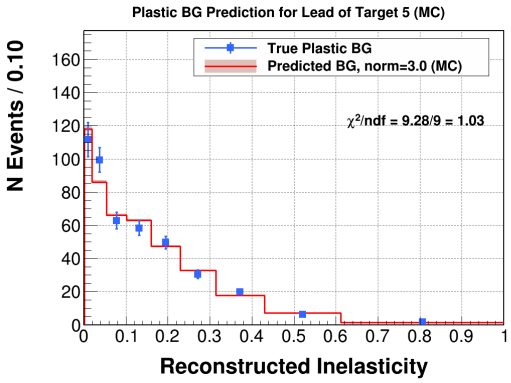

(b) Background as function of the y for lead of target 5

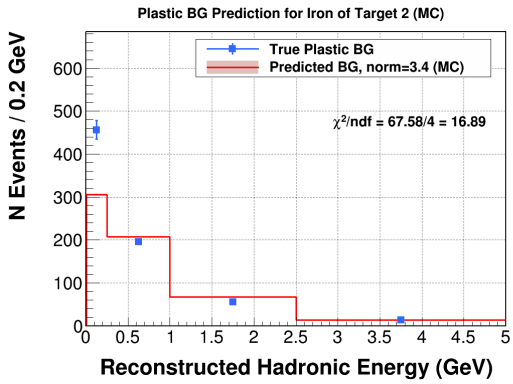

(c) Background as function of the hadronic energy for iron of target 2

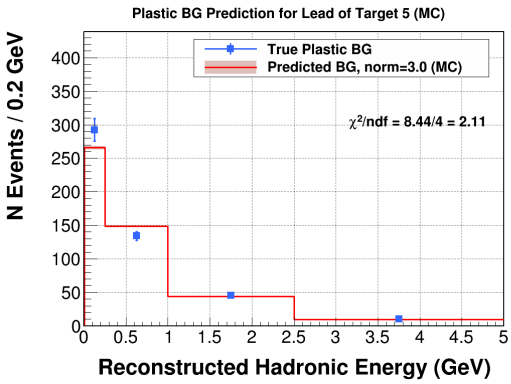

(d) Background as function of the hadronic energy for lead of target 5

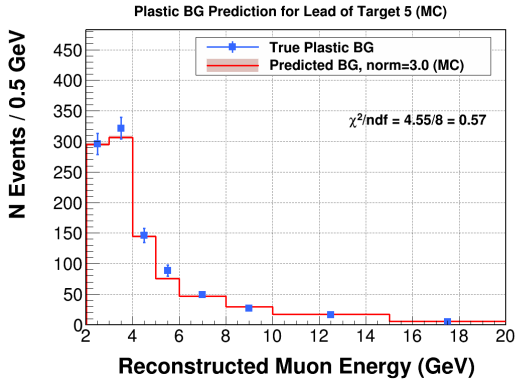

(e) Background as function of Emu for lead of target 5

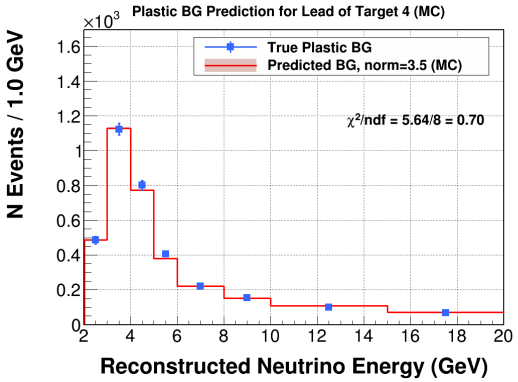

(f) Background as function of Enu for lead of target 4

Figure 6.14: Ratios of plastic background prediction compare to true background as shown by the MC,correction on hadronic energy is applied

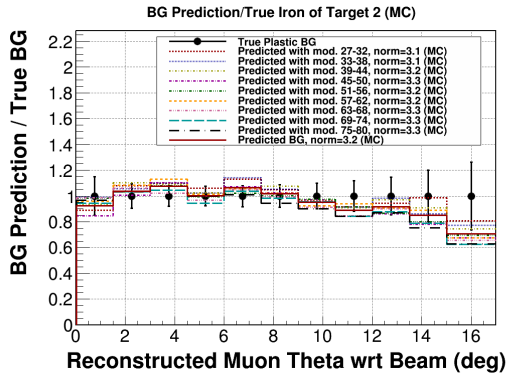

(a) Background prediction as function of the theta mu for iron of target 2

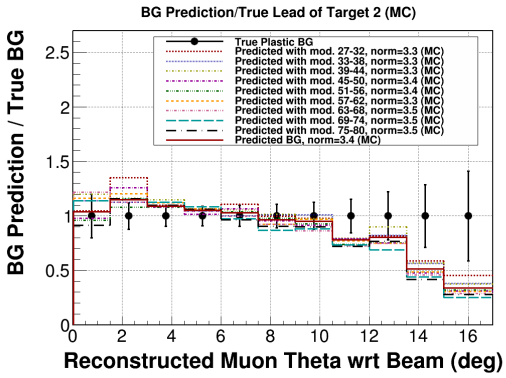

(b) Background prediction as function of the theta mu for lead of target 2

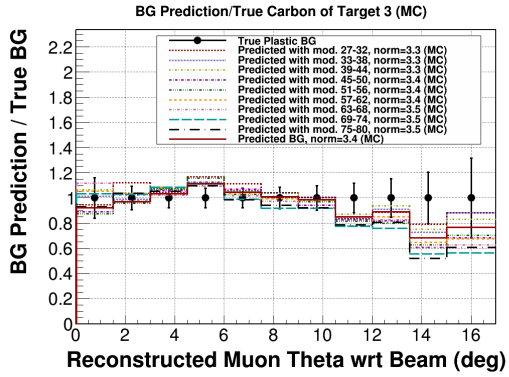

(c) Background prediction as function of the theta mu for carbon of target 3

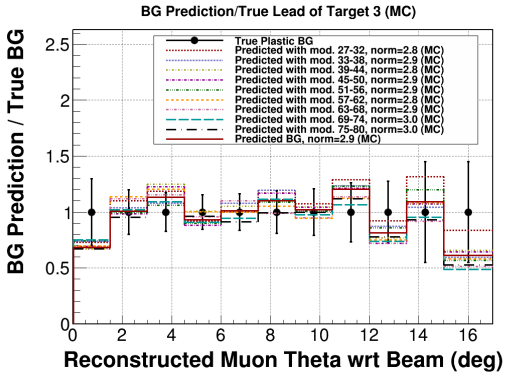

(d) Background prediction as function of the theta mu for lead of target 3

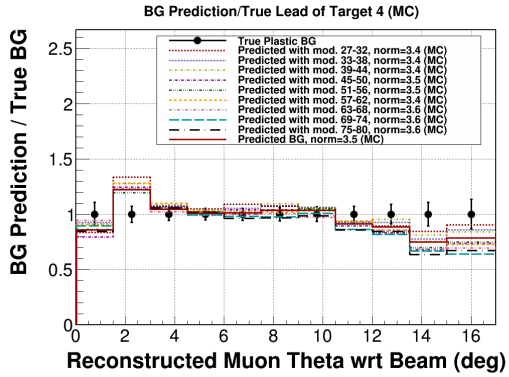

(e) Background prediction as function of the theta mu for lead of target 4

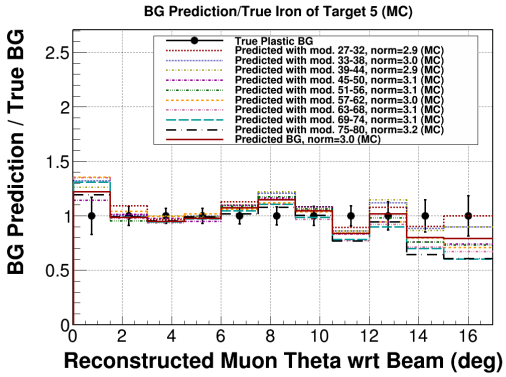

(f) Background prediction as function of the theta mu for iron of target 5

Figure 6.15: o

f plastic background prediction compare to true background as shown by the MC,correction on hadronic energy is applied]Prediction of plastic background prediction compare to true background as shown by the MC correction on hadronic energy is applied

6.2 CROSS SECTION CALCULATION

In order to obtain ratio of cross-section, it is mandatory to process first the absolute cross-section for each nuclei of interest. The ratio presented will be carbon over scintillator (C/CH), iron over scintillator (Fe/CH) and lead over scintallator (Pb/CH) Both numerator and denominator are computed using the same formula.

The total cross section for neutrino energy bin i is calculated as

$$\sigma_i = \frac{\sum_j U_{ij} \left(N_j - N_j^{bg} \right)}{\epsilon_i T \Phi_i}, \tag{6.3}$$

where j is the index of a smeared E_ν bin, U_{ij} is a function that accounts for smearing from true bin i to reconstructed bin j, N_j is the number of selected events, N_j^{bg} is the estimated number of background events, ϵ_i is the efficiency for reconstructing signal events, T is the number of target nucleons, and Φ_i is the flux in bin i. The flux-integrated differential cross section for an x_{bj} bin i is

$$\left(\frac{d\sigma}{dx_{bj}} \right)_i = \frac{\sum_j U_{ij} \left(N_j - N_j^{bg} \right)}{\epsilon_i T \Phi \Delta_i(x_{bj})}, \tag{6.4}$$

where Φ is the flux integrated over the acceptance range of E_ν = 2–20 GeV, $\Delta_i(x_{bj})$ is the width of the bin, and other terms have the same meaning as in Eq. 6.3.

details for selected sample N_j was described in Sec. 6.1 and background estimation N_j^{bg} in Sec. 6.1.7. Target numbers T are in Table 6.2. The remaining components that need to be developed are the Bin migration U_{ij} (6.2.1) and efficiency correction ϵ_i is outlined in Sec. 6.2.2. The flux is an important components of the cross-section but when the ratio is formed, the flux is the same regardless the nuclei so it cancels out for ratio results.

6.2.1 Unfolding detector smearing and bin migration

The general problem of unfolding consists in estimating a probability distribution where data is subject to random fluctuations due to limited resolution. Without unfolding, a measurement cannot be compared with the results of other experiments. In this analysis, E_ν and x_{bj} are the variable of interest. The background-substracted reconstructed E_ν distribution is unfolded into true kinematics E_ν distributions for each target section using the iterative Bayesian technique with 4 iterations [**?**].

The nuclear effects of the E_ν distribution are well simulated so any introduced model dependence is negligible. Reconstructed x_{bj} distributions are not unfolded because that may introduce a strong model dependence on x_{bj}-dependent nuclear effects that are not well simulated and the smearing in x_{bj} significant and asymmetric

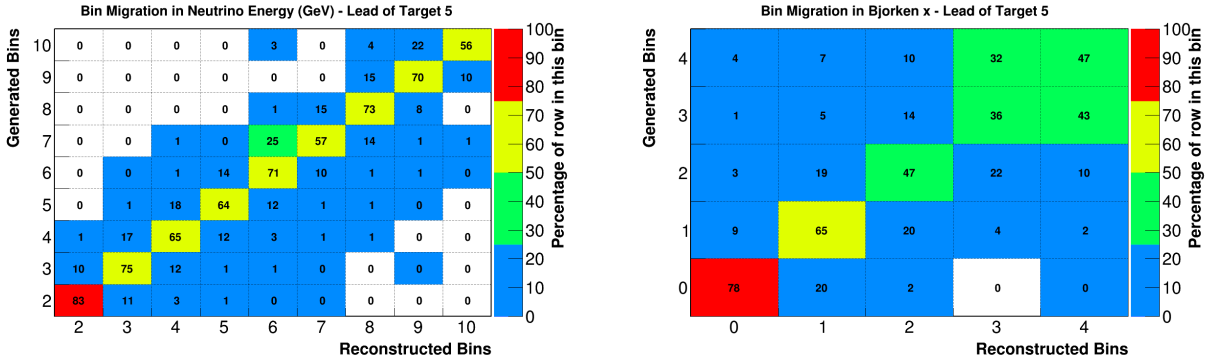

(a) E_ν, Lead of Target 5

(b) x_{bj}, Lead of Target 5

Figure 6.16: Bin migration matrices for E_ν (left) and x_{bj} (right) calculated with simulation. The x-axis is the reconstructed quantity and the y-axis is the generated quantity.

6.2.2 Efficiency correction

The efficiency is the rather complicated convolution of the MINERνA (and MINOS) detector acceptances, the muon tracking efficiency in both detectors, the muon track matching efficiency between MINERνA and MINOS, and the signal event selection efficiency of the applied selection. The following factors are applied:

The muon track matching efficiency need to be applied because of the lost of events cause by reconstruction failures in MINERνA or MINOS. To measure the tracking efficiency in MINERνA, a sample of events was selected which have a track in MINOS that is pointing into the MINERνA fiducial area and also have muon-like activity in the MINERνA detector. fraction of such events that also had a track in MINERνA is the muon track matching efficiency for MINERνA. Measuring the MINOS muon track matching efficiency is the inverse of MINERνA muon track matching efficiency with the difference that MINOS efficiency is sensitive to the intensity of the neutrino

playlist 5				
MINERνA μ tracking eff.	all events	0.976	$\pm$0.01	$\pm$0.01
MINOS μ tracking eff. low mom.	$p_{\mu}^{MINOS} \leq 3.0$ GeV/c	0.966	$\pm$0.003	$\pm$
MINOS μ tracking eff. high mom.	$p_{\mu}^{MINOS} > 3.0$ GeV/c	0.990	$\pm$0.001	$\pm$

Figure 6.17: Muon track matching efficiency for the antineutrino playlist and MINOS muon track matching efficiency classified into low and high momentum are applied

spill. This efficiency is then the fraction of events that has corresponding track in MINOS. The sample is divided into low and high momentum. The low momentum sample muons were deflected by more than 4 cm and high momentum are deflected by less than 1 cm in the MINERνA downstream calorimeters.

6.2.3 Reconstruction efficiency

The calculation of efficiency for neutrino and antineutrino at MINERνA is the same, so a comparison of the efficiency is shown at Figure (6.18). Efficiency is defined as the fraction of signal events that pass all event selection criteria. Efficiency for antineutrino is found to be higher because muon are more straight forward and more likely to end up into MINOS.

Efficiency for true kinematics bin i is measured in simulation as the fraction of generated events

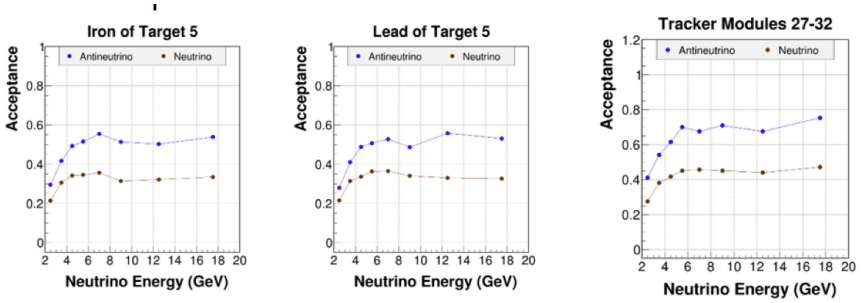

Figure 6.18: Monte Carlo simulation of efficiency for neutrino and antineutrino

which are observed and selection in the event sample

$$\epsilon_i = \frac{N^{obs.}_{i,sig}}{N^{gen.}_{i,sig.}}. \tag{6.5}$$

The numerator $N^{obs.}_{i,sig.}$ is the number of generated signal events in bin i which pass the event selection fiducial requirements. The denominator $N^{gen.}_{i,sig.}$ is the number of generated signal events in bin i. Note that the numerator definition does not require that the generated event is a charged-current ν_μ event, because the simulation will be used directly to predict the backgrounds from NC and WS events.

Purity is the fraction of events in the sample that are generated signal events ()

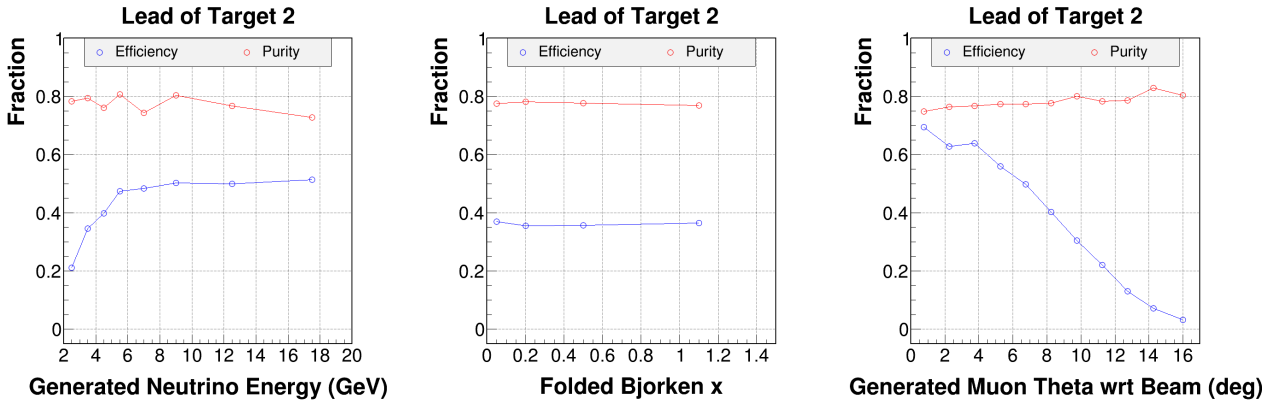

Figure 6.19: MC calculation of efficiency (red) and purity (black) for the lead of Target 2 as a function of E_ν (left), x_{bj} (center), and θ_μ (right). Efficiency is defined as the fraction of signal events selected. Purity is the fraction of selected events that are signal; the major source of impurity is the scintillator background. These plots are representative of all targets.

6.2.4 Antineutrino flux

The flux is an important components of the cross-section but when the ratio is formed but the a ratio will give a measurement independent of the flux. The flux contains many uncertainty that the entire community of neutrino cross-section measurements are still investigating, MINERνA can avoid including flux uncertainty yet by making ratio over different nuclei. The flux for antineutrino used for this analysis is show at the Figure 2.8.

6.2.5 Cross-section results

Absolute cross-section as function of E_ν and x_{bj} for carbon, iron, lead and scintillator are show on Figure (). Both data and MC are shown with statistical errors and systematic error details at (). Obvious large error bars on data are due to statistical limitation for carbon, iron and lead. The discrepancy between data and MC in general for these distribution are due to flux modeling which are still under heavy investigation at MINERνA. The number of events passing all selection requirements are the sample (6.21) and the background is the number of scintillator events contaminations in a passive target sample. The signal included in the cross-section calculation is the sample from which the background has been extracted.

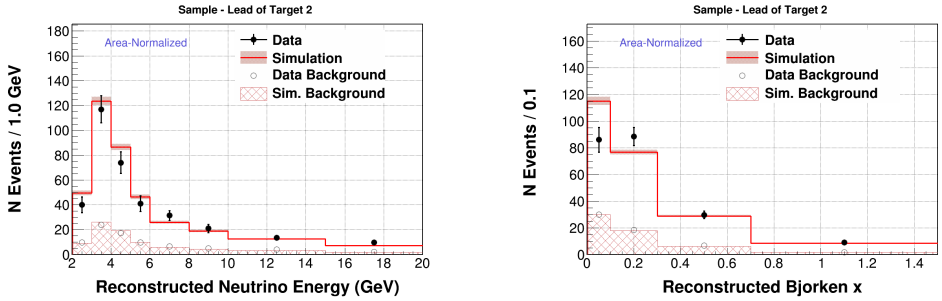

Figure 6.20: For lead of target 2 as function of E_ν and x_{bj}

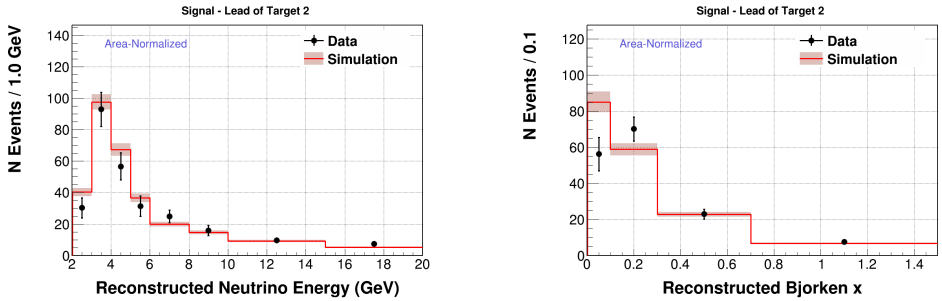

Figure 6.21: signal for lead of target 2 as function of E_ν and x_{bj} with data + statistical error and MC with total systematic error. Ratio of data to MC for signal. Fractional errors on signal is shown with the total summed in quadrature

The Absolute cross-section for each nuclei of each target is show at Figures (6.23,6.24, 6.25, 6.28, 6.26,6.30, 6.29). Data are shown with statical error and these errors are large due to statistical

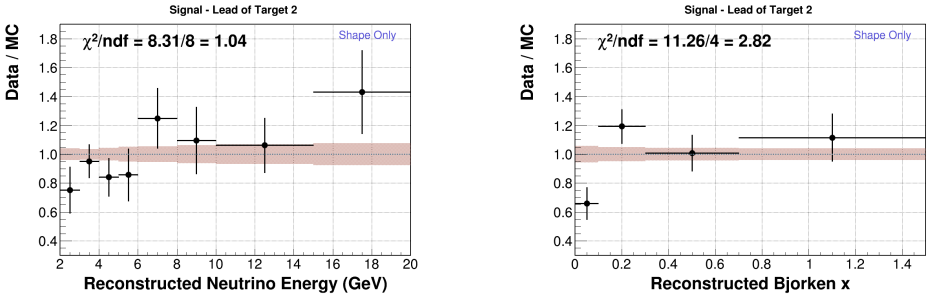

Figure 6.22: Ratio of data to MC for signal.

limitation. MC are show with error but the systematics that is mostly dominated by the flux in a very large fraction are shown at Figure 6.34, 6.31, 6.32, 6.33

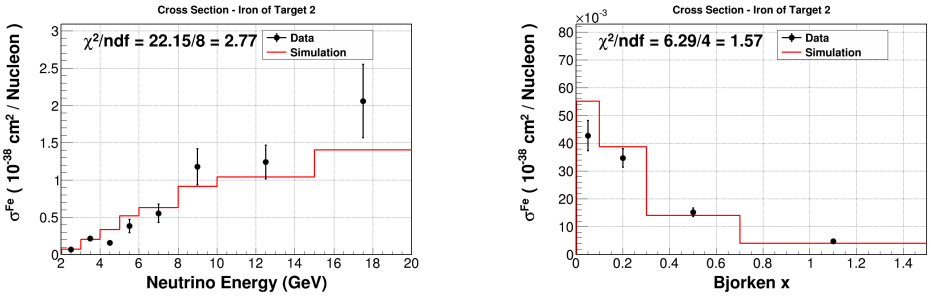

Figure 6.23: Measured and absolutely-normalized prediction (MC) of σ and $\frac{d\sigma}{dx_{bj}}$. Statistical error is shown on data points and total systematic error is shown in the shaded simulation band for iron of target 2

6.3 SYSTEMATICS ERRORS

6.3.1 Neutrino flux

The uncertainty in the knowledge of these parameters is represented as a systematic error that is estimated by using the so called ?many universes? method. This method consists in re-calculating

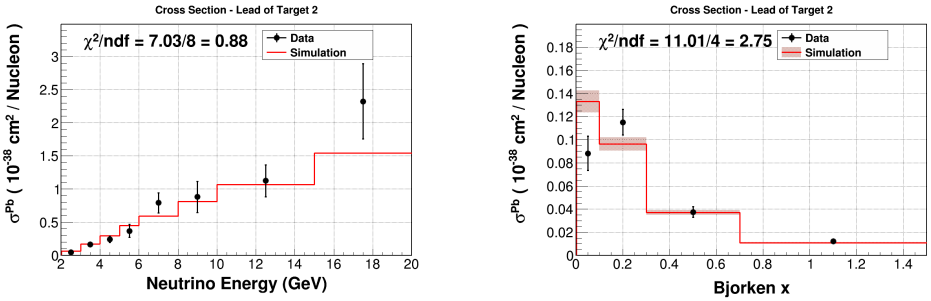

Figure 6.24: Measured and absolutely-normalized prediction (MC) of σ and $\frac{d\sigma}{dx_{bj}}$. Statistical error is shown on data points and total systematic error is shown in the shaded simulation band for lead of target 2

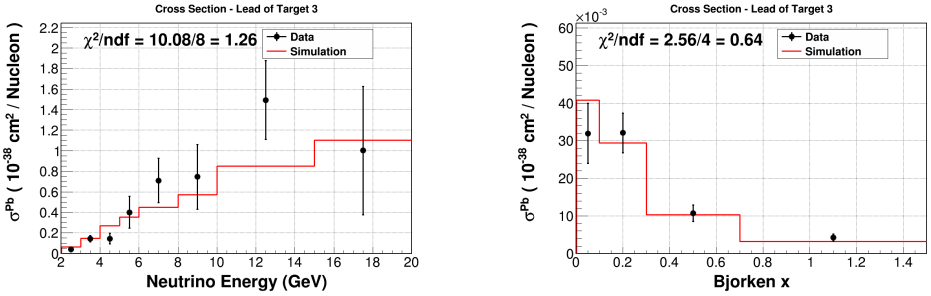

Figure 6.25: Measured and absolutely-normalized prediction (MC) of σ and $\frac{d\sigma}{dx_{bj}}$. Statistical error is shown on data points and total systematic error is shown in the shaded simulation band for lead of target 3

the cross section using different values of a model or reconstruction parameter.

$$\sigma_{i,universe} = \frac{\sum_j U_{i,universe}\left(N_{i,universe} - N^{bg}_{i,universe}\right)}{\epsilon_i T \Phi_i}, \tag{6.6}$$

Where the only difference from equation 6.3 s the additional index universe that represents the result in a different universe and CV stands for Central Value which is the result of the MC simulation without any variation. Notice that the migration matrix, selection efficiency and flux are also re-calculated for each universe. When the variation affects the event selection, the cross

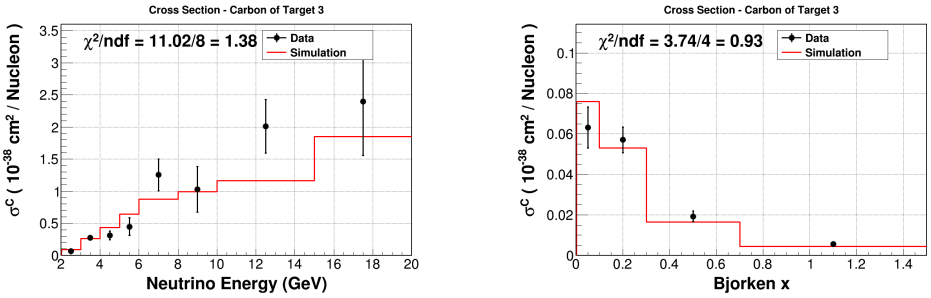

Figure 6.26: Measured and absolutely-normalized prediction (MC) of σ and $\frac{d\sigma}{dx_{bj}}$. Statistical error is shown on data points and total systematic error is shown in the shaded simulation band for carbon of target 3

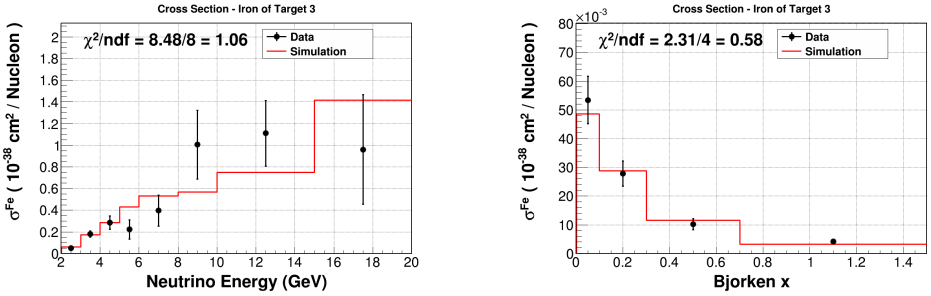

Figure 6.27: Measured and absolutely-normalized prediction (MC) of σ and $\frac{d\sigma}{dx_{bj}}$. Statistical error is shown on data points and total systematic error is shown in the shaded simulation band for iron of target 3

section is also re-calculated. For each model or reconstruction parameter there can be several universes and the covariance matrix and errors are calculated as:

$$cov_{i,j} = \frac{1}{N} \sum_{k=1}^{N} \left(x_{ki} - \bar{x_i}\right) \left(x_{kj} - \bar{x_j}\right). \tag{6.7}$$

Where N is the number of universes considered. Neutrino flux uncertainties are incorporated into the analysis by means of a re-weighting tech- nique. To generate a distribution in a given universe,

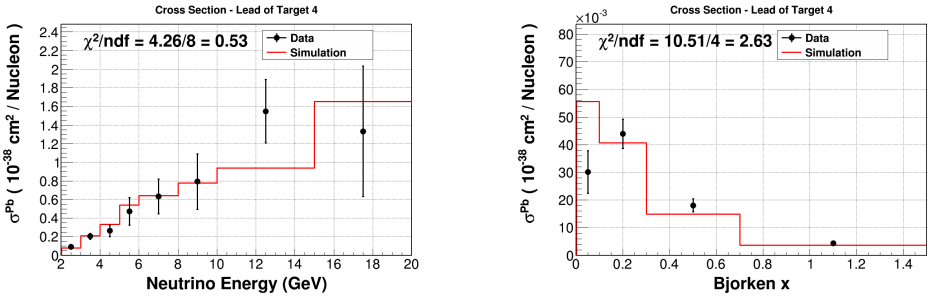

Figure 6.28: Measured and absolutely-normalized prediction (MC) of σ and $\frac{d\sigma}{dx_{bj}}$. Statistical error is shown on data points and total systematic error is shown in the shaded simulation band for lead of target 4

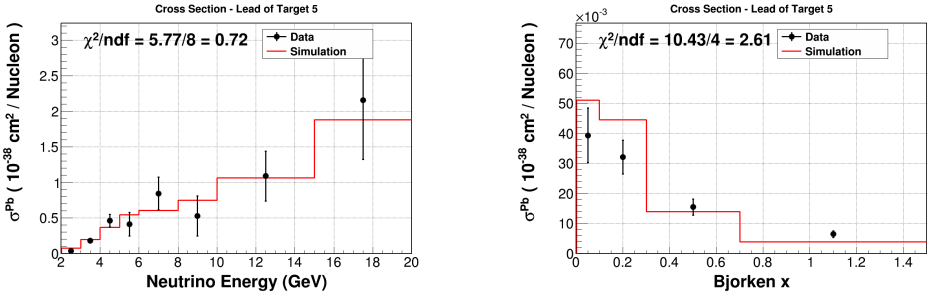

Figure 6.29: Measured and absolutely-normalized prediction (MC) of σ and $\frac{d\sigma}{dx_{bj}}$. Statistical error is shown on data points and total systematic error is shown in the shaded simulation band for lead of target 5

we apply the weight for that universe to each simulated interaction as a function of neutrino energy. Uncertainties due to the neutrino flux are divided in three types: Beam Focus- This category represents the uncertainties due to the proton beam and focusing system of the NuMI beamline such as the alignment and the magnetic field model in the horns. They are estimated to be small at most energies, but are significant (8%) at the focousing peak. NA49- Uncertainty due to the hadron production constraint on the flux simulation using data from the NA49 hadron production experiment at CERN. Beam Tertiary- Uncertainty due to the cascade model predictions of tertiary

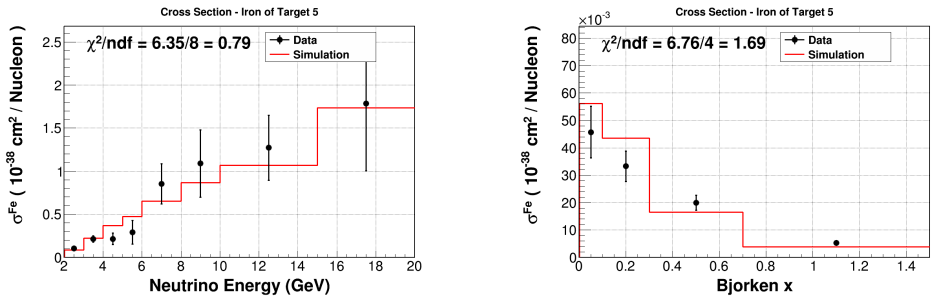

Figure 6.30: Measured and absolutely-normalized prediction (MC) of σ and $\frac{d\sigma}{dx_{bj}}$. Statistical error is shown on data points and total systematic error is shown in the shaded simulation band for iron of target 4

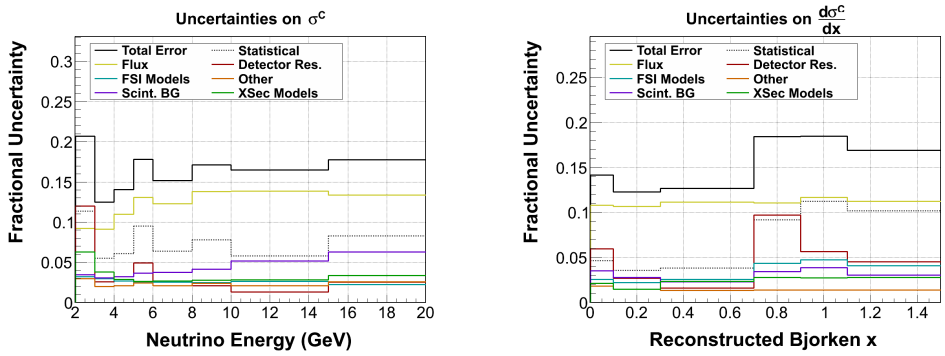

Figure 6.31: Fraction errors on the absolute cross-section for Carbon

pion production. This uncertainty can be as high as 30% in the focusing peak. The uncertainty on the number of muon neutrino charged current interactions in the MINER?A detector of the three sources listed above are given in Figure 6.35

6.3.2 Muon Energy Scale

Uncertainty due to the muon energy scale is the sum of three effects [99] and summarized at Table 6.4. There is additional error in energy loss in MINERνA due to uncertainties in the material assay and the dE/dx model, which are independent. These errors depend on how much material

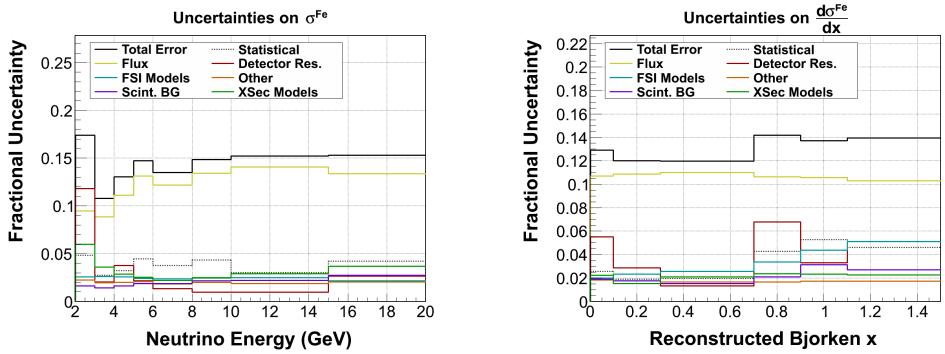

Figure 6.32: Fraction errors on the absolute cross-section for Iron

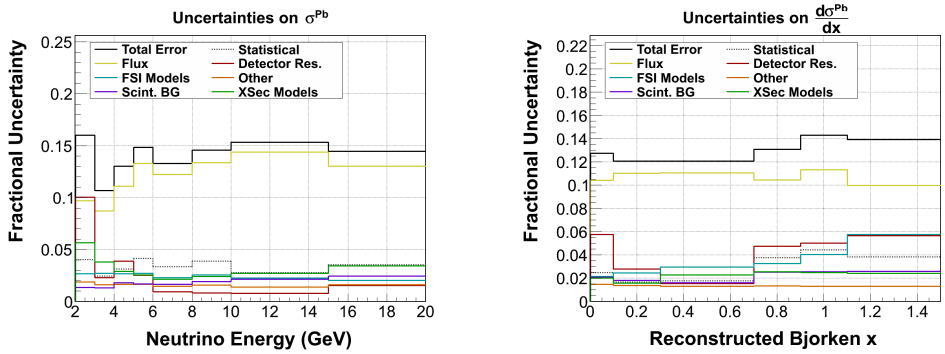

Figure 6.33: Fraction errors on the absolute cross-section for Iron

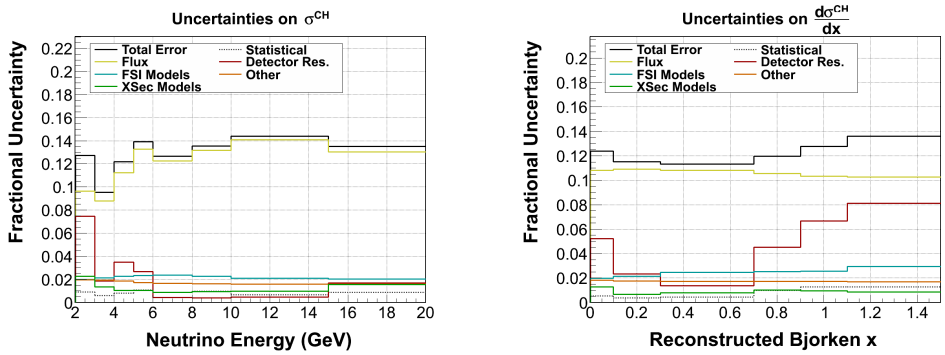

Figure 6.34: Fraction errors on the absolute cross-section for scintillator

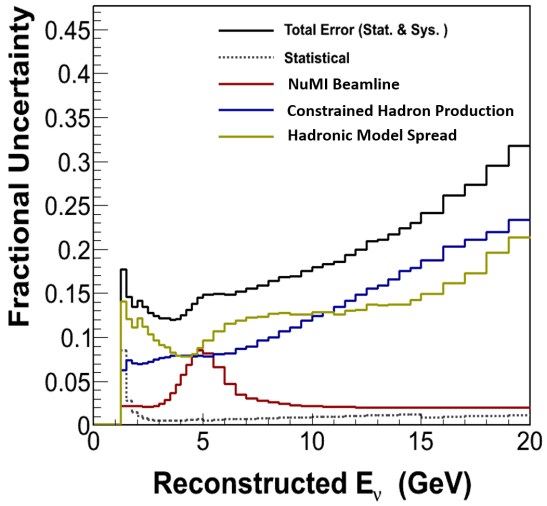

Figure 6.35: Flux errors on the charge current $\overline{\nu}_\mu$ event rate. The three uncorrelated sources of systematic uncertainty are discussed in detail in Sec. 6.2.4.

Error Source	Error
MINOS Range	2.0%
MINOS Curvature ($p_\mu < 1\text{GeV}/c$)	2.5%
MINOS Curvature ($p_\mu > 1\text{GeV}/c$)	0.6%
MINERνA dE/dx (scintillator events)	30 MeV
MINERνA dE/dx (C, Fe, Pb events)	40 MeV
MINERνA mass (scintillator events)	11 MeV
MINERνA mass (C, Fe, Pb events)	17 MeV

Table 6.4: Uncertainties on muon momentum reconstruction. The types of uncertainty are independent and added in quadrature. The MINOS range uncertainty is relevant for all muons. The MINOS curvature uncertainty is only relevant if the muon momentum was reconstructed by curvature.

the muon traverses in MINERνA, so there is a larger error assigned to events in the upstream passive nuclear targets region. The dE/dx model uncertainty adds 30 (40) MeV to the error budget on muon energy for events in scintillator (carbon, iron, or lead). The MINERνA material mass uncertainty adds 11 (17) MeV to the error budget on muon energy for events in scintillator (carbon, iron, or lead).

6.3.3 Recoil Energy Scale

For the recoil energy scale, the uncertainty on the response of protons, pions, neutrons and electromagnetic (EM) particles are considered. The simulated recoil energy that comes from final state protons are varied independently by 3.5%, pions by 5%, neutrons by 10% and EM particles by 10%. Each variation defines one universe. In addition, we treat the cross talk component of the recoil energy in the same way and it is varied by 20%.

6.3.3.1 Final State Interaction Models The α scale and the polyline corrections to the recoil energy of Eq. **??** have been tuned with a MC sample. The FSI models used in this MC determine what happens to a particle generated by the neutrino interaction before it exits the nuclear environment. Many of these uncertainties are evaluated by reweighting MC events. Reweightable FSI model parameters are shifted according to their uncertainty and the probability of the FSI scattering processes is recalculated. The cross section ratios analysis is repeated for each $\pm 1\sigma$ excursion of model parameters. Half of the maximum deviation among the excursions and central value is the error from the model parameter. Model parameters are varied independently, and the resulting errors are added in quadrature. Table 6.5 lists the reweightable model parameters and their uncertainties. FSI model parameters that cannot be handled through event reweighting are evaluated with statistically independent MC samples, which are discussed in Sec. 6.3.3.

6.3.3.2 Detector Response A MC prediction of the composition of the hits identified as the recoil system was used to evaluate the error in the detector response. The composition breaks down the visible energy, corrected for traversed passive material, into the sources of visible energy. This procedure used only reconstructed information to identify hits, but uses generator information to

Model Parameter	$\delta(P)/P$
Pion mean free path	$\pm 20\%$
Pion charge exchange probability	$\pm 50\%$
Pion elastic reaction probability	$\pm 10\%$
Pion inelastic reaction probability	$\pm 40\%$
Pion absorption probability	$\pm 20\%$
Pion π-production probability	$\pm 20\%$
Nucleon mean free path	$\pm 20\%$
Nucleon charge exchange probability	$\pm 50\%$
Nucleon elastic reaction probability	$\pm 30\%$
Nucleon inelastic reaction probability	$\pm 40\%$
Nucleon absorption probability	$\pm 20\%$
Nucleon π-production probability	$\pm 20\%$
AGKY model x_f distribution	$\pm 20\%$
Pion angular distribution	isotropic $\leftrightarrow$ Rein-Sehgal
Resonance branching ratio decay to photon	$\pm 50\%$

Table 6.5: Uncertainties on final state interaction models in GENIE. This table is based on a similar table found in [**?**].

Energy Source	Uncertainty
Proton	3.5%
Neutron (KE <50 MeV)	25%
Neutron (50 <KE <150 MeV)	10%
Neutron (KE >150 MeV)	20%
Muon	2.4%
γ, π^0, $e^{\pm}$	3%
$\pi^{\pm}$, Kaon	5%
Cross talk	20%
Other	20 %

Table 6.6: Uncertainties on the detector response to different sources of light.

identify the source responsible for the energy recorded. The uncertainties in the detector's response to each source of visible energy are summarized in Table 6.6.

6.4 ANALYSIS INDEPENDENT OF THE FLUX

Cross section ratios are formed with the sums of efficiency-corrected distributions, taking into account the number of targets. Dividing by the flux is not necessary because the flux has no spatial dependence throughout the detector; the flux is identical through all targets. Uncertainties in the flux model are considered and contribute a small uncertainty on the ratio, which is discussed in Sec. 6.2.4. The ratio of cross sections is formed simply by dividing the cross section of one nucleus by another nucleus.

A statistically independent scintillator sample is used to form each of the ratios of carbon, iron, and lead. The tracking modules in each sample are chosen using faux targets so that the areal shape

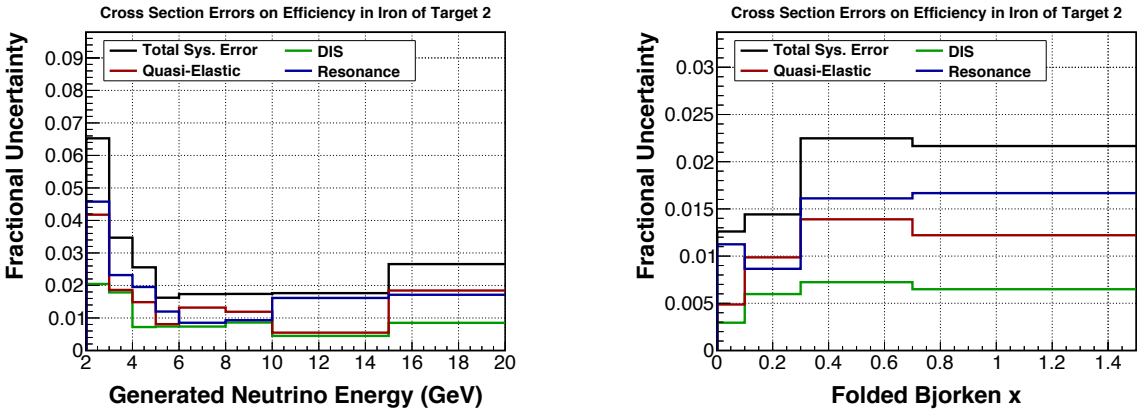

Figure 6.36: Relative errors on the reconstruction efficiency from uncertainty in cross section models. Model parameters are grouped by their associated interaction process. See Table **??** for the list of model parameters considered.

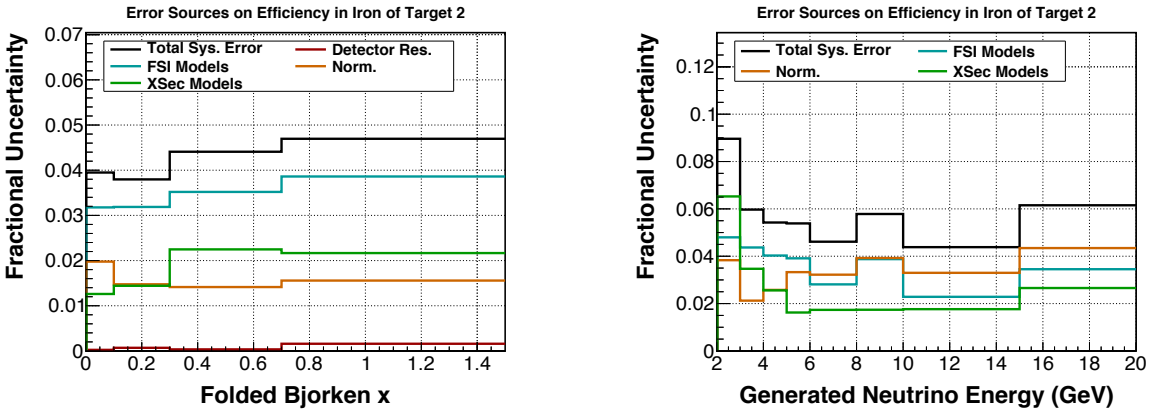

Figure 6.37: Summary of relative systematic errors on the reconstruction efficiency.

Target Number	Scintillator Modules
2	27–32, 51–56, 63–68
3	33–38, 57–62, 75–80
4	45–50
5	39–44, 69–74

Table 6.7: Listing of scintillator modules paired to each passive target assembly. This is done to keep the ratios statistically independent. The assignments are chosen to minimize systematic bias by varying the transverse and longitudinal areas of the modules.

of scintillator matches that of the target sections that comprise the target nucleus. Modules that are matched to each target come from varied longitudinal position to further avoid systematic bias. The modules used as the denominator in the ratio for each target are listed in Table 6.7.

6.4.1 Summing Over Targets

Event samples have thus far been separated by their target section or faux target; each has its own background, migration matrix, and efficiency correction because the reconstruction and acceptance differs across targets. This segregation increases the accuracy of all the above corrections. Event samples of similar nuclei are added after the efficiency correction is applied, since at that point all such differences have been removed. For example, the efficiency-corrected samples of the iron from Targets 2, 3, and 5 are added. The figure shows cross section ratios. The cross sections of the passive carbon, iron, and lead targets are normalized by the cross section on scintillator using the pairings of Table 6.7. The isoscalar correction has been applied. These plots suggest that the measurements of the cross sections using different targets are compatible and can thus be added without systematic bias.

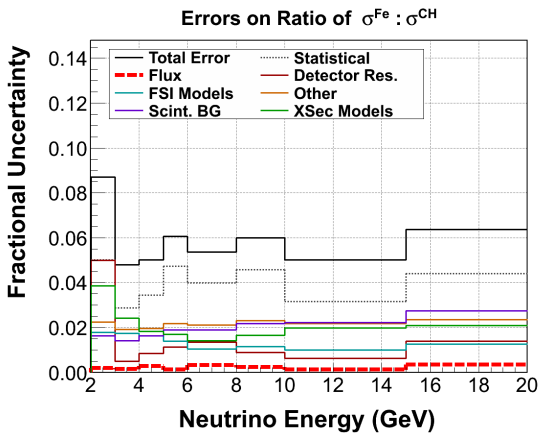

(a) $\sigma_{Fe} : \sigma_{CH}$

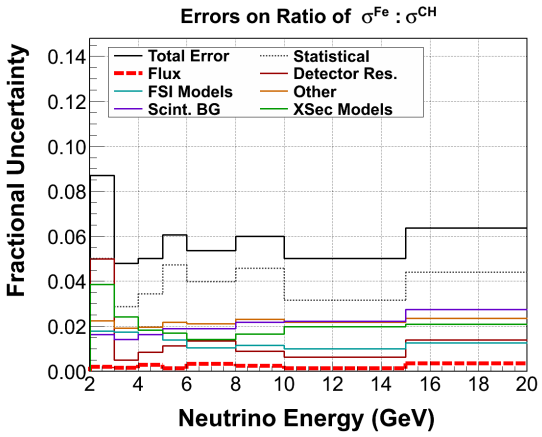

(b) $\frac{d\sigma_{Fe}}{dx} : \frac{d\sigma_{CH}}{dx}$

Figure 6.38: The flux error that was the dominant error in absolute cross-section is almost negligibly small in the measurement of cross section ratios.

6.4.2 Cancellation of Errors in Ratios

Many uncertainties on the measured cross section cancel or are greatly reduced through the use of ratios. A summary of errors for the absolute cross section of iron and the ratio of iron to scintillator cross sections is shown in Fig. 6.38, 6.39. and 6.40. Compare to 6.34, 6.31, 6.32, 6.33, the cancellation of errors from the flux is the most beneficial reduction created by the ratio.

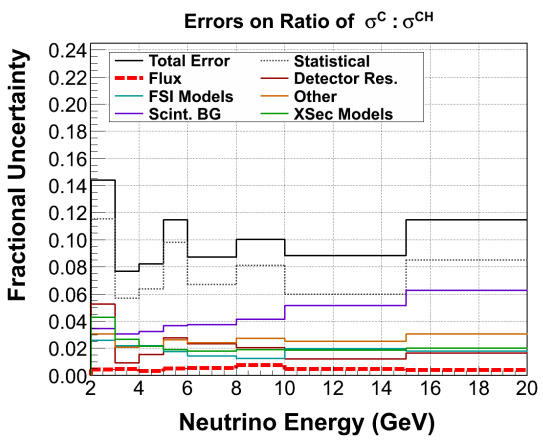

(a) $\sigma_C : \sigma_{CH}$

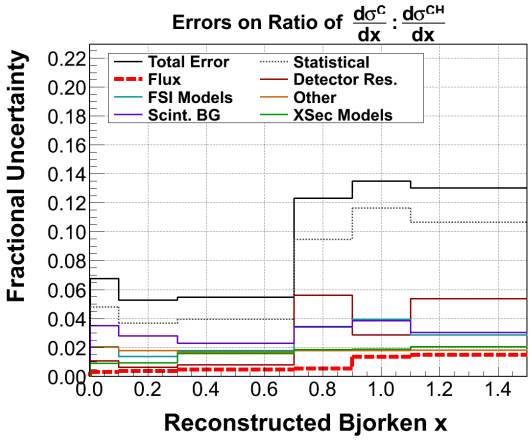

(b) $\frac{d\sigma_C}{dx} : \frac{d\sigma_{CH}}{dx}$

Figure 6.39: The flux error that was the dominant error in absolute cross-section is almost negligibly small in the measurement of cross section ratios.

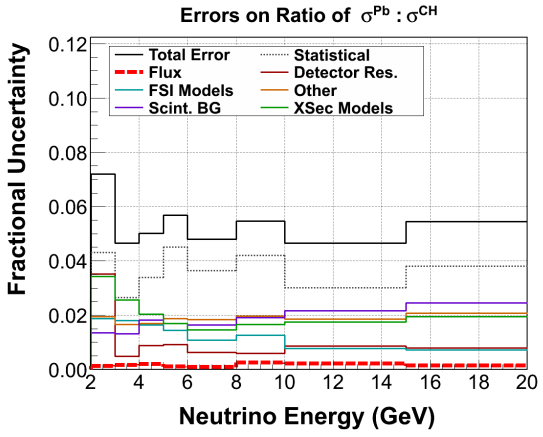

(a) $\sigma_{Pb} : \sigma_{CH}$

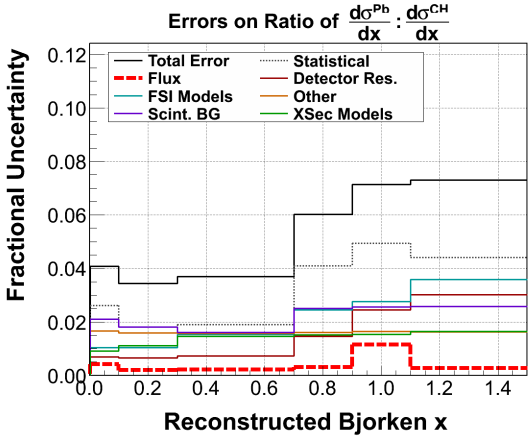

(b) $\frac{d\sigma_{Pb}}{dx} : \frac{d\sigma_{CH}}{dx}$

Figure 6.40: The flux error that was the dominant error in absolute cross-section is almost negligibly small in the measurement of cross section ratios.

7.0 RESULTS AND CONCLUSIONS

7.1 RESULTS

7.1.1 Neutrino Energy Result

Understanding neutrino energy is a crucial part of neutrino oscillation process. The results of this analysis is as a function of neutrino energy. Being able to make measurements of cross-section over different heavy nuclei and independent of the flux is important to study nuclear effects in neutrino interactions. If this is not well understood as function of E_ν, large uncertainties will be introduced in the shape of the neutrino energy which is an important components of the measurements of oscillation parameters. Within the statistics limitation of the sample, an overall agreement is observed as function of E_ν for a charge current inclusive ratio using antineutrino. Large errors bars for data are observed especially for carbon/CH ratio due to that limitation but Iron and lead measurements have already enough statistics to drawn conclusion. This agreement suggest that within the 1GeV bin of neutrino energy bin size, the MC contains well modeled nuclear dependence of inclusive charge current $\overline{\nu}_\mu$. This results also confirm the published results using inclusive charge current ν_μ published at [146] that a well modeled nuclear dependence as function of E_ν for 1 GeV bin size. Many improvement can be done for this analysis, in order first to increase statistics, MINERνA is working hard to take in consideration muons that stops within the detector, geometric acceptance of MINERνA relative to MINOS will not be a worry anymore since muons can be studies using matching with the ECAL or HCAL. Another important factor is that the target most upstream which is target composed by Iron and Lead has not been used for this analysis which impact the statistics because it contains 30% of the iron and lead data statistics.

This results shows that GENIE which is the current models used handle very neutrino energy simu-

lations, but there are questions remaining related to nuclear effects that will play role on oscillation searches since these nuclear effect will affect the cross-section measurements.
MINERνA collaboration are working hard to provide improvements on the E_ν bin size limitation because oscillation searches requires smaller bin size like for example, MINOS using 0.5 GeV bins. This smaller bin sized may shows unmodeled behavior in nuclear dependence.
Many neutrino oscillation experiments operate at energies slightly lower than those measured in this analysis. Lower energy experiments often attempt to isolate the quasi-elastic channel, which is the dominant channel for neutrino energies below 3 GeV.

The energy resolution of the detector will improve through better reconstruction and further analysis of data taken by the MINERνA Test Beam Collaboration (E977). MINERνA has already presented an analysis of quasi-elastic events in the tracker region and analysis of isolation quasi-elastic using the same nuclei for this inclusive measurements will be presented very soon. Lower energy below 3GeV bin disagreement in which charge current quasi-elastic channel is dominant, suggest that an isolation of that channel would help to understand more the nuclear dependence for elastics and inelastic interactions.

7.1.2 Bjorken x Result

This result shows small disagreement with MC at both low and high values of x_{bj}. In order to study the nuclear effects, neutrino physicist usually refer to the x_{bj}, for this analysis, we saw a disagreement with MC is observed for charge current inclusive ratio using $\overline{\nu}_\mu$ as function of x_{bj}. Carbon and scintillator is showing discrepancy for both low and high value of x_{bj}, this has been observed by the measurement using ν_μ as well but not statistically significant. For lead vs scintillator and iron vs scintillator on the other shows good agreements on highest bin of x_{bj} which was not observed by the ν_μ analysis. At low x_{bj}, the discrepancy is a suppression that grows with the size of the nucleus. at $x_{bj} < 0.1$ ia deficit is observe and it increases with the size of the nucleus, the possibly additional nuclear shadowing in n scattering is suspected to be the reason, a study more directly in deep inelastic region for antineutrino is underway at MINERνA to understand this effect. Nuclear shadowing plays a major roles for $\overline{\nu}_\mu$ interaction on heavy nuclei, pions final state are more likely to be absorb within the nucleus and modeling intranuclear effect is a challenge

that neutrino cross-section community are still dealing with.

7.1.2.1 High Bjorken x Events at high x_{bj} (x_{bj} = [0.7,1.1]) come predominantly from the quasi-elastic channel. The nuclear dependence of quasi-elastic neutrino scattering is not well simulated. The quasi-elastic cross section is usually simulated using a dipole for the axial form factor, which has just one parameter: the axial mass M_A. High precision measurements of M_A using quasi-elastic neutrino scattering off nuclei made in last decade show significant tension. At higher x_{bj}, only carbon shows disagreement between Data and MC, but iron and lead have a better agreements compared to the results of ν_μ which showed a enhancement of the discrepancy that grows as function of the size of the nucleus. charge current quasi-elactics dominates for events at high x_{bj}. the nuclear dependence of quasi-elastic neutrino scattering is not well simulated . Quasi-elactics cross-section measurements and nuclear dependence has been a topic of great interest in the field for the last few years. The nuclear dependence of transverse enhancement in quasi-elastic channel is suspected to be one reason of the discrepancy that is currently observed for both ν_μ mode et $\overline{\nu}_\mu$.

7.2 CONCLUSIONS

This thesis describe the results of our research at the Main Injector Neutrino Experiment for ν - A known as MINERνA. This work consists of the first measurement of the ratios of cross-section as a function of neutrino energy and differential cross-section as a function of Bjorken x for antineutrino charged current inclusive interactions on carbon, lead , iron and hydrocarbon (CH). The analysis required neutrino energy between 2GeV et 20GeV and the angle of muon $\theta_m u < 17$degree After producing absolute cross-section as input for a ratio, a measurement of ratio of charge current inclusive $\overline{\nu}_\mu$ cross section σ in carbon, iron, and lead to scintillator are shown in Fig. 7.1. and results of ratio for carbon, Iron and lead ratio to scintillator CH for $\frac{d\sigma}{dx_{bj}}$ are shown in Fig. 7.2. Figure 7.3 shows the relative errors on these measurements.

Avoiding statistics limitations and geometric limitations of MINERνA related to MINOS should have a tremendous improvements for future results. MINERνA will provides crucial inputs for neutrino oscillation experiments using these data on different nuclei which suggest a better under-

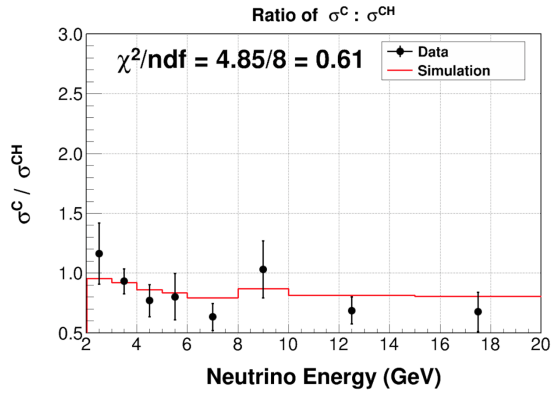

(a) Carbon

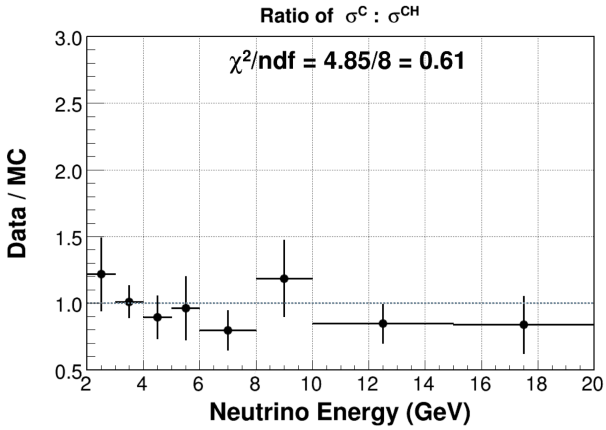

(b) Data to MC ratio for carbon

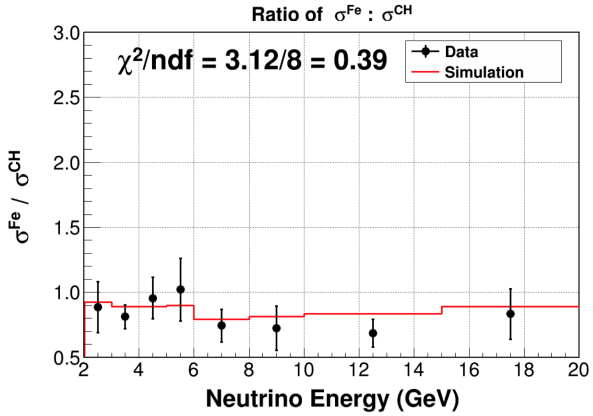

(c) Iron

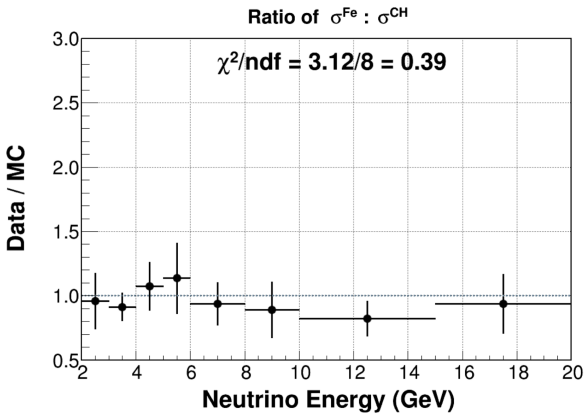

(d) Data to MC ratio for iron

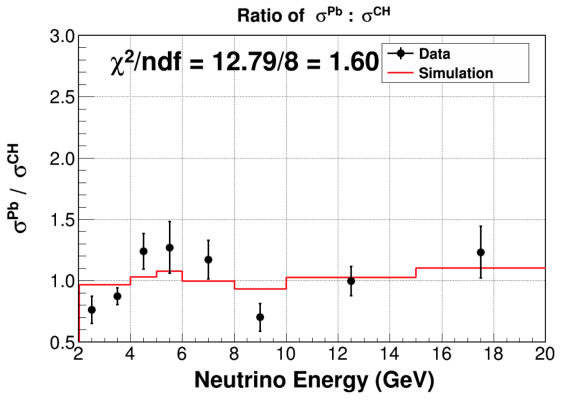

(e) Lead

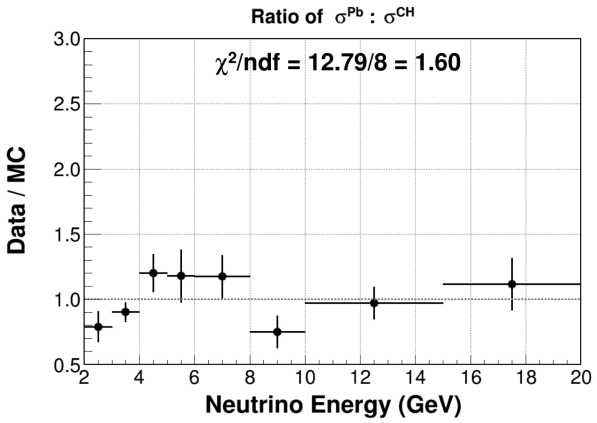

(f) Data to MC ratio for lead

Figure 7.1: (Left) Results for the measurement of ratios of numubar charged current inclusive σ in carbon (C), iron (Fe), and lead (Pb) to scintillator (CH). (Right) The ratio of data to MC of this

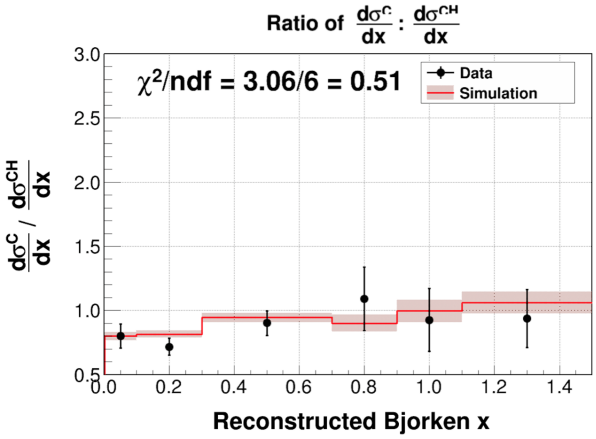

(a) Carbon

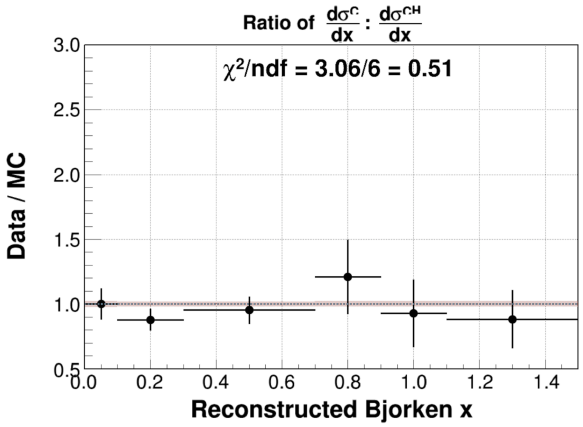

(b) Data to MC ratio for carbon

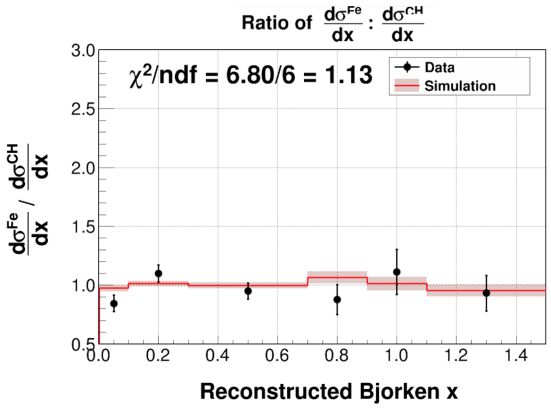

(c) Iron

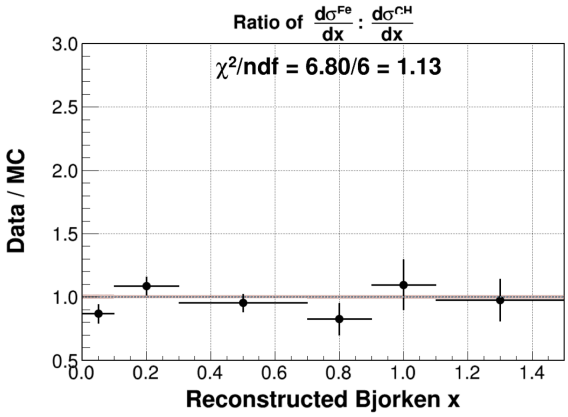

(d) Data to MC ratio for iron

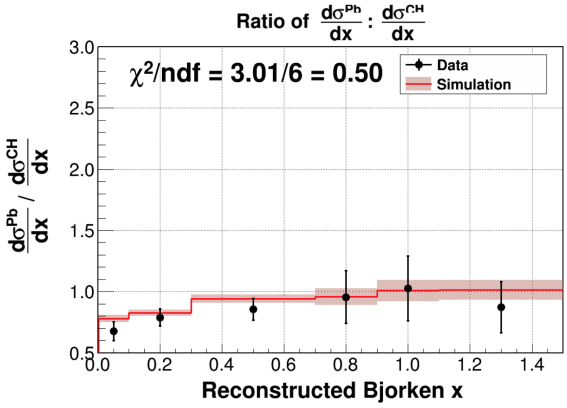

(e) Lead

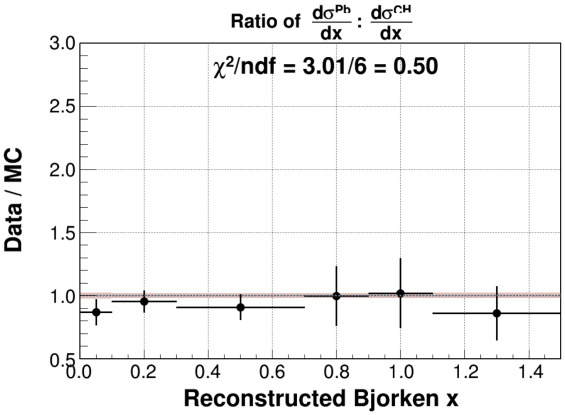

(f) Data to MC ratio for lead

Figure 7.2: (Left) Results for the measurement of ratios of $\overline{\nu}_\mu$ charged current inclusive $\frac{d\sigma}{dx_{bj}}$ in carbon (C), iron (Fe), and lead (Pb) to scintillator (CH). (Right) The ratio of data to MC of this

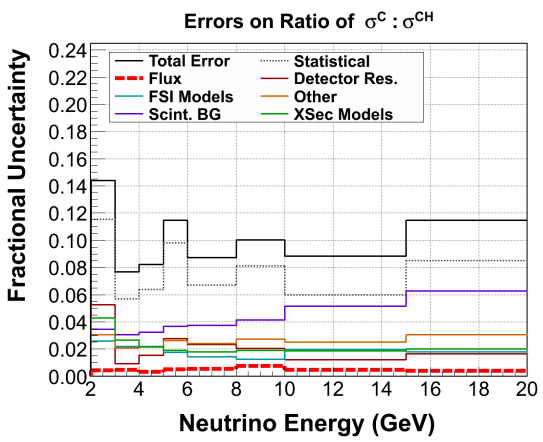

(a) Carbon E_ν

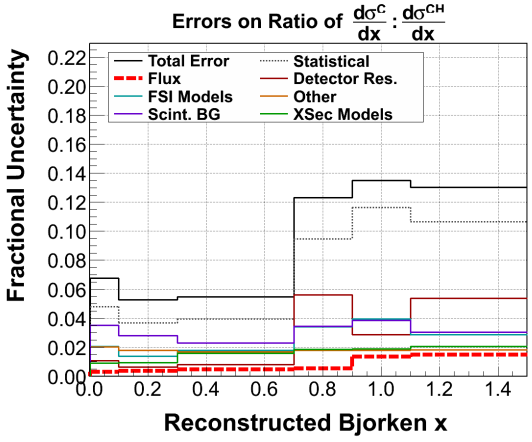

(b) Carbon x_{bj}

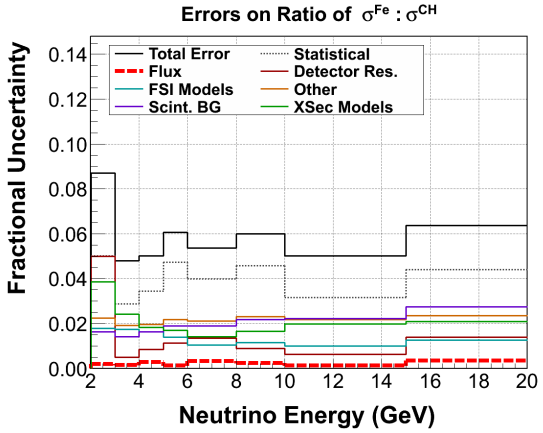

(c) Iron E_ν

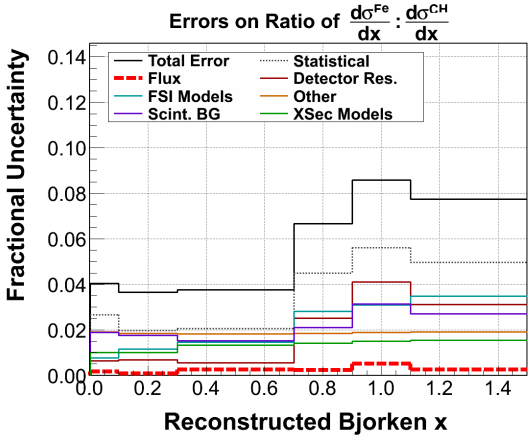

(d) Iron x_{bj}

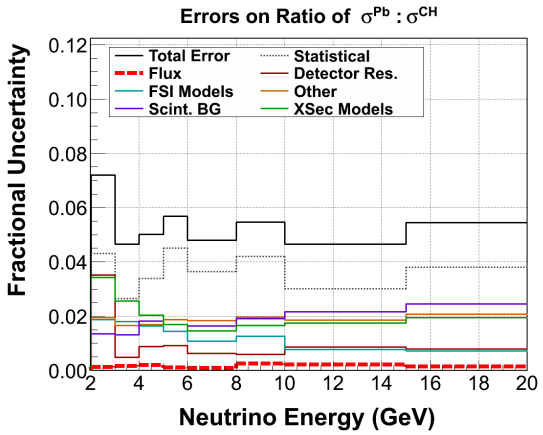

(e) Lead E_ν

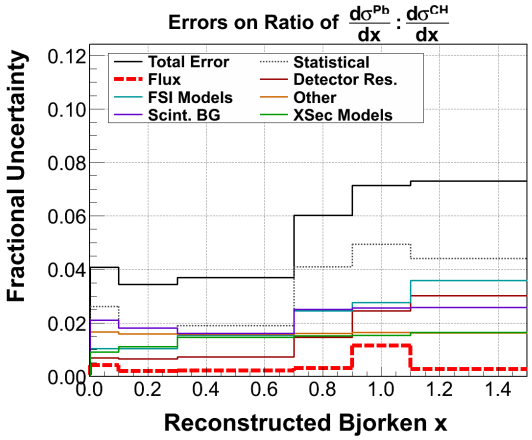

(f) Lead x_{bj}

Figure 7.3: Relative errors on ratios of σ and $\frac{d\sigma}{dx_{bj}}$.

standing of nuclear dependence of the neutrino inclusive cross-section in the few GeV neutrino energy. The results shown also suggest a better understudying of the statistics itself. In order to measure and to probe lower energies analysis using difference nuclei from which oscillations searches will take a input, improvements of statics. energy resolutions are needed.

The measurement of the nuclear dependence of $\frac{d\sigma}{dx_{bj}}$ shows two distinct behaviors for low and high x_{bj}. Low x_{bj} is again a confirmation of ν_μ analysis with a possible explanations include enhanced of nuclear shadowing. Higher x_{bj} disagreement is still under investigation of why similar behavior as ν_μ was not observed but several analysis are already on-going at MINERνA that study only isolated charge quasi-elastic events in the nuclear targets of the detector.

8.0 BIBLIOGRAPHY

[1] F. Halzen and D. Martin, "Quarks and Leptons: An Introductory Course in Modern Particle Physics," John Wiley and Sons, Inc. (1984).

[2] D. Schmitz Review of Current and Future Neutrino Cross?Section Experiments AIP Conference Proceedings 1222, 52 (2010).

[3] J. D. Bjorken and S. D. Drell, "Relativistic Quantum Mechanics," McGraw-Hill, Inc. (1964).

[4] G. Aad *et al.* [ATLAS Collaboration], "Observation of a new particle in the search for the Standard Model Higgs boson with the ATLAS detector at the LHC," Phys. Lett. B **716**, 1 (2012) [arXiv:1207.7214 [hep-ex]].

[5] S. Chatrchyan *et al.* [CMS Collaboration], "Observation of a new boson at a mass of 125 GeV with the CMS experiment at the LHC," Phys. Lett. B **716**, 30 (2012) [arXiv:1207.7235 [hep-ex]].

[6] J. Beringer *et al.* (Particle Data Group), Phys. Rev. D86, 010001 (2012).

[7] DONUT COllaboration: T. Patzak, First direct observation of the tau neutrino, Europhys. News 32, 56 (2001).

[8] V.N. Gribov and B. Pontecorvo, Phys. Lett B **28**(1969)493.

[9] ALEPH Collaboration:D. Decamp et al., Determination of the Number of Light Neutrino Species, Phys. Lett. B **231**(1989)519.

[10] Delphi Collaboration:P.A. Aarnio et al.,Measurement of the Mass and Width of the Z0 Paricle from Multi-Hadronic Final States Produced in the e+ e- Annihilation, Phys. Lett. B **231** (1989)539.

[11] L3 Collaboration:B. Adeva et al.,A Determination of the Properties of the Neutral Intermediate Vector Boson Z0, phys. Lett. B **231** (1989)509.

[12] A. Bradford, A. Bodek, H. Budd and J. Arrington, A New Parametrization of the Nucleon Elastic Form Factors, Nucl. Phys. Proc. Suppl. 159, 127 (2006).

[13] J. Nieves, Jose Enrique Amaro, and M. Valverde. Inclusive quasi-elastic neutrino reactions. In: Phys.Rev. C70 (2004), p. 055503.

[14] C. Athanassopoulos et ala., Candidate Events in a Search for Anti-Muon-Neutrino -¿ Anti-Electron-Neutrino Oscillations, Phys. Rev. Lett. 75, 2650, 1995.

[15] P. Minkowski, Phys. Lett. B 67 (1977) 421.

[16] S. L. Glashow, Quarks and Leptons ed M Le vy et al (New York: Plenum) p 707, 1980.

[17] R. N. Mohapatra and G. Senjanovich, Phys. Rev. Lett. 44 (1980) 912.

[18] Bernard, V., et al., 2002, J. Phys. G 28, R1.

[19] OPAL Collaboration:M.Z. Akrawy et al.,Measurement of the Z0 Mass and Width with the OPAL Detector at LEP, Phys. Lett. B bf 231 (1989)530.

[20] D. H. Perkins, "Introduction to High Energy Physics," Cambridge University Press, (2000).

[21] B.G Tice, "MIEASUREMENT OF NUCLEAR DEPENDENCE IN INCLUSIVE CHARGED CURRENT NEUTRINO SCATTERING (2013).

[22] C.S. Wu et al., Phys. Rev. **105** (1957)1413.

[23] M. Goldhaber, L. Grodzins, and A.W. Sunyar, Helicity of neutrinos, Phys. Rev. 109 (1958)1015.

[24] C. W. Kim, Neutrino Physics: Fundamentals of Neutrino Oscillations, Proceedings J. Korean Phys. Soc., Suppl. 1996. hep-ph/9607391

[25] B. Kayser, "Neutrino Mass, Mixing, and Flavor Change," (2008). [arXiv:hep-ph/08041497]

[26] G. Arnison, *et al.* [UA1 Collaboration, CERN, Geneva, Switzerland], "Experimental observation of isolated large transverse energy electrons with associated missing energy at s=540 GeV," Physics Letters B, Volume 122, Issue 1, 24 February 1983, Pages 103-116, ISSN 0370-2693, 10.1016/0370-2693(83)91177-2.

[27] G. Arnison, *et al.* [UA1 Collaboration,, CERN, Geneva, Switzerland], "Experimental observation of lepton pairs of invariant mass around 95 GeV/c^2 at the CERN SPS collider," Physics Letters B, Volume 126, Issue 5, 7 July 1983, Pages 398-410, ISSN 0370-2693, 10.1016/0370-2693(83)90188-0.

[28] G. Bertone, D. Hooper and J. Silk, "Particle dark matter: Evidence, candidates and constraints," Phys. Rept. **405**, 279 (2005) [hep-ph/0404175].

[29] A. G. Riess *et al.* [Supernova Search Team Collaboration], "Observational evidence from supernovae for an accelerating universe and a cosmological constant," Astron. J. **116**, 1009 (1998) [astro-ph/9805201].

[30] A. Aguilar *et al.* (LSND),"Evidence for Neutrino Oscillations from the Observation of Electron Anti-neutrinos in a Muon Anti-Neutrino Beam," Phys.Rev.D64:112007, (2001).

[31] A. A. Aguilar-Arevalo, et. al. First measurement of the muon neutrino charged current quasielastic double differential cross section. Phys. Rev. D 81, 092005. May 2010

[32] A. A. Aguilar-Arevalo *et al.* [MiniBooNE Collaboration], "A Combined $\nu_\mu \to \nu_e$ and $\bar{\nu}_\mu \to \bar{\nu}_e$ Oscillation Analysis of the MiniBooNE Excesses," arXiv:1207.4809 [hep-ex].

[33] G. Mangano, G. Miele, S. Pastor, O. Pisanti and S. Sarikas, "Constraining the cosmic radiation density due to lepton number with Big Bang Nucleosynthesis," JCAP **1103**, 035 (2011) [arXiv:1011.0916 [astro-ph.CO]].

[34] J. Schechter and J.W. F. Valle, "Neutrino masses in SU(2) $\otimes$ U(1) theories,"Phys. Rev. D22, 2227 (1980).

[35] J. W. F. Valle, "Current theoretical status of neutrino masses and mixing," AIP Conf. Proc. 1382, 9 (2011), DOI:10.1063/1.3644260.

[36] D.W. Schmitz, "A Measurement of Hadron Production Cross-Sections for the Simulation of Accelerator Neutrino Beams and a Search for $\nu_\mu \rightarrow \nu_e$ Oscillations in the $\Delta \mathrm{m}^2 \approx 1\ \mathrm{eV}^2$ Region," PhD Thesis, Columbia University, 2008.

[37] B. T. Cleveland, *et al.*, "Measurement of the solar electron neutrino flux with the Homestake chlorine detector," Astrophysical Journal 496: 505526, (1998).

[38] Y. Fukuda, *et al.* [The K2K collaboration], "Evidence for oscillation of atmospheric neutrinos," Physical Review Letters 81 (8): 1562-1567, (1998).

[39] M. H. Ahn *et al.*, "Measurement of Neutrino Oscillation by the K2K Experiment," Phys. Rev. D 74, 072003 (2006), [arxiv:hep-ex/0606032].

[40] P. Adamson *et al.* [MINOS Collaboration], "An improved measurement of muon antineutrino disappearance in MINOS," Phys. Rev. Lett. **108**, 191801 (2012) [arXiv:1202.2772 [hep-ex]].

[41] Q. R. Ahmad *et al.* [SNO Collaboration], "Measurement of the rate of nu/e + d $\rightarrow$ p + p + e^- interactions produced by B-8 solar neutrinos at the Sudbury Neutrino Observatory," Phys. Rev. Lett. **87**, 071301 (2001) [nucl-ex/0106015].

[42] K. Eguchi, *et al.*, [KamLAND Collaboration], "First results from KamLAND: evidence for reactor antineutrino disappearance". Physical Review Letters 90 (2): 021802021807, (2003).

[43] F. P. An *et al.* [DAYA-BAY Collaboration], "Observation of electron-antineutrino disappearance at Daya Bay," Phys. Rev. Lett. **108**, 171803 (2012) [arXiv:1203.1669 [hep-ex]].

[44] J. K. Ahn, *et al.* [RENO Collaboration], "Observation of Reactor Electron Antineutrino Disappearance in the RENO Experiment," Physical Review Letters 108 (18): 191802, (2012)

[45] M. Auger *et al.* [EXO Collaboration], "Search for Neutrinoless Double-Beta Decay in ^{136}Xe with EXO-200," Phys. Rev. Lett. **109**, 032505 (2012) [arXiv:1205.5608 [hep-ex]].

[46] J. Argyriades *et al.*, "Measurement of the double-beta decay half-life of ^{150}Nd and search for neutrinoless decay modes with the NEMO-3 detector," Phys. Rev. C 80, 032501(R) (2009).

[47] D. G. Phillips, II, E. Aguayo, F. T. Avignone, III, H. O. Back, A. S. Barabash, M. Bergevin, F. E. Bertrand and M. Boswell *et al.*, "The Majorana experiment: an ultra-low background search for neutrinoless double-beta decay," J. Phys. Conf. Ser. **381**, 012044 (2012) [arXiv:1111.5578 [nucl-ex]].

[48] F. Fraenkle, (2011), "KATRIN: an experiment to determine the neutrino mass," Proceedings of the DPF-2011 Conference, arXiv:1110.0087.

[49] K. Abe, *et al.* [The T2K Collaboration], The T2K experiment, Nuclear Instruments and Methods in Physics Research Section A659, 106-135 (2011).

[50] D. S. Ayres *et al.* [NOvA Collaboration], "NOvA: Proposal to build a 30 kiloton off-axis detector to study nu(mu) $\rightarrow$ nu(e) oscillations in the NuMI beamline," hep-ex/0503053.

[51] OPERA Collaboration, R. Acquafredda *et al.*, "The OPERA experiment in the CERN to Gran Sasso neutrino beam," JINST 4 (2009) P04018.

[52] D. Griffith, "Introduction to Elementary Particles," John Wiley and Sons, Inc., (1987).

[53] C. H. Llewellyn Smith, "Neutrino Reactions At Accelerator Energies," Phys. Rept. 3, 261 (1972).

[54] D.H. Wilkinson, "Limits to second-class nucleonic currents," Nuclear Instruments and Methods A455, 656659 (2000).

[55] M. Day and K. S. McFarland,"Differences in Quasi-Elastic Cross-Sections of Muon and Electron Neutrinos," arXiv:1206.6745 [hep-ph].

[56] H. S. Budd, A. Bodek and J. Arrington, "Modeling quasielastic form-factors for electron and neutrino scattering," arXiv:1206.6745hep-ex/0308005.

[57] J.J. Kelly, "Simple parametrization of nucleon form factors," Phys. Rev. C70, (2004).

[58] J. A. Formaggio, G. P. Zeller, From eV to EeV: Neutrino cross sections across energy scales, Rev. Mod. Phys.: Volume 84.1307 (2012).

[59] A. Bodek, S. Avvakumov, R. Bradford and H. S. Budd, "Vector and Axial Nucleon Form Factors:A Duality Constrained Parameterization," Eur. Phys. J. C **53**, 349 (2008) [arXiv:0708.1946 [hep-ex]].

[60] M. L. Goldberger and S. B.Treiman, "Decay of the Pi Meson," Phys. Rev. 5, 1178-1184 (1958).

[61] S. Adler. In: Phys.Rev. B135 (1964), p. 963

[62] Veljko Dmitrasinovic and T. Sato. PCAC constraints on pion production / absorption within nonrelativistic nuclear dynamics. In: Phys.Rev. C58 (1998), pp. 19371947.

[63] R. Fiore and V.R. Zoller. Color dipoles, PCAC and Adlers theorem. In: JETP Lett. 85 (2007). 14 pages, 2 figures, pp. 309314.

[64] D. Rein and L.M. Sehgal. PCAC and the Deficit of Forward Muons in pi+ Production by Neutrinos. In: Phys.Lett. B657 (2007), pp. 207209.

[65] S. Choi, V. Estenne, G. Bardin, N. De Botton, G. Fournier, P. A. M. Guichon, C. Marchand and J. Marroncle *et al.*, "Axial and pseudoscalar nucleon form factors from low energy pion electroproduction," Phys. Rev. Lett. 71, 3927 (1993).

[66] A. Liesenfeld *et al.* [A1 Collaboration], "A measurement of the axial form factor of the nucleon by the p(e,$e'\pi^+$)n reaction at W=1125 MeV," Phys. Lett. B 468, 20 (1999).

[67] M. N. Rosenbluth, "High Energy Elastic Scattering of Electrons on Protons," Phys. Rev. 79, 615619 (1950).

[68] A. Bodek, S. Avvakumov, R. Bradford and H. S. Budd, "Extraction of the axial nucleon form-factor from neutrino experiments on deuterium," J. Phys. Conf. Ser. **110**, 082004 (2008) [arXiv:0709.3538 [hep-ex]].

[69] V. Lyubushkin, *et al.* "A study of quasi-elastic muon neutrino and antineutrino scattering in the NOMAD experiment." Eur. Phys. J. C63:355-381, (2009).

[70] A.A. Aguilar-Arevalo *et al.*, "Measurement of Muon Neutrino Quasi-Elastic Scattering on Carbon," arXiv:0706.0926 [hep-ex], Phys. Rev. Lett. 100, 032301 (2008).

[71] A. A. Aguilar-Arevalo *et al.* [MiniBooNE Collaboration], "First Measurement of the Muon Neutrino Charged Current Quasielastic Double Differential Cross Section," Phys. Rev. D **81**, 092005 (2010) [arXiv:1002.2680 [hep-ex]].

[72] O. Benhar, N. Farina, H. Nakamura, M. Sakuda, and R. Seki, "Electron- and neutrino-nucleus scattering in the impulse approximation regime," Phys. Rev. D 72, 053005 (2005).

[73] J. T. Sobczyk, "Multinucleon ejection model for Meson Exchange Current neutrino interactions," Phys. Rev. C **86**, 015504 (2012) [arXiv:1201.3673 [hep-ph]].

[74] R. A. Smith, E. J. Moniz, "Neutrino Reactions On Nuclear Targets," Nucl. Phys. **B43**, 605 (1972).

[75] A. Bodek and J. L. Ritchie, "Fermi-motion effects in deep-inelastic lepton scattering from nuclear targets," Phys. Rev. D 23:5 1071-1091, (1981).

[76] A. M. Ankowski and J. T. Sobczyk, "Construction of spectral functions for medium-mass nuclei," Phys. Rev. C **77**, 044311 (2008) [arXiv:0711.2031 [nucl-th]].

[77] A. Bodek, H. S. Budd and M. E. Christy, "Neutrino Quasielastic Scattering on Nuclear Targets: Parametrizing Transverse Enhancement (Meson Exchange Currents)," Eur. Phys. J. C **71**, 1726 (2011) [arXiv:1106.0340 [hep-ph]].

[78] J. Amaro, M. Barbaro, J. Caballero, T. Donnelly, and J. Udias, 2011b, Phys. Rev. D 84, 033004.

[79] M. Barbaro, *et al.*, 2011, arXiv:1110.4739.

[80] C. Giusti, and A. Meucci, 2011, arXiv:1110.4005.

[81] M. Martini, M. Ericson, and G. Chanfray, 2011, Phys. Rev. C 84, 055502.

[82] J. Nieves, I. Simo, and M. Vacas, 2012, Phys. Lett. B 707, 72.

[83] M. Martini, M. Ericson, and G. Chanfray, 2011, Phys. Rev. C 84, 055502.

[84] J. T. Sobczyk, arXiv:1109.1081 (2012).

[85] C.D. Curtis, G.M. Lee, C.W. Owen, C.W. Schmidt and W.M. Smart, Linac H-beam operation and uses at Fermilab, IEEE Trans. Nucl. Sci. 26 (1979) 3760.

[86] Stephen Holmes *et al.* "Overview of the Tevatron collider complex: goals, operations and performance," 2011 JINST 6 T08001.

[87] C.W. Schmidt, The Fermilab 400 MeV Linac upgrade, in Proceedings of 1993 Particle Accelerator Conf., Washington U.S.A. (1993), pg. 1655.

[88] Detailed description of the Booster Beam in "Rookie Books," http://www-bdnew.fnal.gov/operations/rookie_books/Booster_V4.1.pdf.

[89] Detailed description of the Main Injector in "Rookie Books," http://www-bdnew.fnal.gov/operations/rookie_books/Main_Injector_v1.1.pdf.

[90] NuMI Technical Design Handbook, Chapter 2 Overview of the NuMI Beamline, http://www-numi.fnal.gov/numwork/tdh/TDH_V2_2_Overview.pdf.

[91] A.G. Abramov *et al.* "Beam optics and target conceptual designs for the NuMI project," Nuclear Instruments and Methods in Physics Research A 485 (2002) 209227

[92] Z. Pavlovic, "Observation of Disappearance of Muon Neutrinos in the NuMI Beam," FERMILAB-THESIS-2008-59.

[93] S. E. Kopp, "The NuMI neutrino beam at Fermilab," arXiv:0508001.

[94] Detailed description of the NuMI Beam in "Rookie Books," www-bdnew.fnal.gov/operations/rookie_books/NuMI_v1.pdf

[95] R. Zwaska *et al.* "Beam-based alignment of the NuMI target station components at FNAL," Nuclear Instruments and Methods in Physics Research A 568 (2006) 548560.

[96] James Hylen, personal communication.

[97] S. Kopp *et al.* "Secondary beam monitors for the NuMI facility at FNAL," Nuclear Instruments and Methods in Physics Research A 568 (2006) 503519.

[98] "Extruded Plastic Scintillator for MINERvA," A. Pla-Dalmau, A. Bross, V. Rykalin and B. Wood, 2005 IEEE NSS Conference Record, FERMILAB-CONF-05-506.

[99] MINERνA collaboration, "Design, Calibration, and Performance of the MINERvA Detector" , Nucl. Inst. and Meth. A743 (2014) 130.

[100] A. Pla-Dalmau *et al.*, Nuclear Instruments and Methods in Physics Research A 466 (2001) 482491.

[101] Kuraray Co. Ltd., "Scitntillation Materials" catalogue.

[102] http://sales.hamamatsu.com/en/products/electron-tube-division/detectors/photomultiplier-tubes/part-r7600-00-m64.php, (2011).

[103] G. Perdue, *et al.*, "The MINERνA Data Acquisition System and Infrastructure," submitted to Nuclear Instruments and Methods in Physics Research A (2012).

[104] B. Baldin, MINERvA Chain Readout Controller, MINERvA Doc-DB 1516, 2007.

[105] B. Baldin, VME Data Acquisition Modules for MINERvA Experiment, FERMILAB-TM-2458-PPD, 2010.

[106] B. Baldin, MINERvA CROC Interface Module, MINERvA Doc-DB 1238, 2009.

[107] The CAEN v2718 VME Crate Controller ¡http://www.caen.it/nuclear/product.php?mod=V2718¿, 2008.

[108] T. Fitzpatrick, C. Rotolo, MINOS Master Clock System Preliminary Design Specification, NUMI-NOTR-ELEC-827, Fermilab, 2000.

[109] Windows Vista. http://windows.microsoft.com/en-US/windows-vista/products/home; 2010.

[110] Fermi Linux. http://fermilinux.fnal.gov/; 2011.

[111] T. Cundiff, *et al.*, "The MINOS near detector front end electronics," IEEE Trans. Nucl. Sci. 53, 1347-1355 (2006).

[112] D.G. Michael *et al.*, "The magnetized steel and scintillator calorimeters of the MINOS experiment," Fermilab-Pub-08-126, Nucl.Instrum.Meth.A596:190-228(2008).

[113] C. Anderson *et al.*, "The ArgoNeuT Detector in the NuMI Low-Energy beam line at Fermilab," http://arxiv.org/abs/1205.6747 (2012).

[114] C.Andreopoulos, A.Bell, D.Bhattacharya, F.Cavanna, J.Dobson, S.Dytman, H.Gallagher, R.Hatcher, P.Kehayias, A.Meregaglia, D.Naples, G.Pearce, A.Rubbia, M.Whalley, T.Yang, "The GENIE Neutrino Monte Carlo Generator", Nucl.Instrum.Meth.A614:87-104,2010.

[115] J. Allison *et al.*, IEEE Transactions on Nuclear Science 53 No. 1 (2006) 270-278.

[116] A. M. McGowan, "Observation of deficit in NuMI neutrino-induced rock and non-fiducial muons in MINOS Far Detector and measurement of neutrino oscillation parameters," FERMILAB-THESIS-2007-31.

[117] C. Alt, B. Baatar, D. Barna, G. Barr, J. Bartke, L. Betev, H. Biakowska, C. Blume, B. Boimska and J. Bracinik, *et al.* "Inclusive production of charged pions in p + C collisions at 158 GeV/c beam momentum," NA Collaboration. Eur. Phys. J. C 49, 897917 (2007).

[118] M. Kordosky , et. al. A brief documentation of the flux used in the may 2013 analyses, (2013). MINERvA Internal Note.

[119] D.S. Barton *et al.* "Experimental study of the A dependence of inclusive hadron fragmentation," Phys. Rew. D Vol27 N 11.

[120] ROOT Collaboration, http://root.cern.ch.

[121] R. Bradford, A. Bodek, H. Budd and J. Arrington, "A new parameterization of the nucleon elastic form factors," Nucl. Phys. Proc. Suppl. 159, 127 (2006) [arXiv:hepex/0602017].

[122] D. Rein and L. M. Sehgal, "Neutrino Excitation Of Baryon Resonances And Single Pion Production," Annals Phys. 133, 79 (1981).

[123] A. Bodek, I. Park and U. -k. Yang, "Improved low Q**2 model for neutrino and electron nucleon cross sections in few GeV region," Nucl. Phys. Proc. Suppl. **139**, 113 (2005).

[124] R.E. Hendrick, L. Li, "Gauge-model constraints of recent elastic and deep-inelastic neutral-current data," Phys. Rev. D19, 779, (1979).

[125] J.B. Birks, Proc. Phys. Soc. A64: 874 (1951).

[126] Autodesk (2011). AutoCAD [Computer program]. Available at: http://usa.autodesk.com/autocad/ (Accessed 5 July 2011).

[127] "Geometry Description Markup Language for Physics Simulation and Analysis Applications," R. Chytracek, J. McCormick, W. Pokorski, G. Santin, IEEE Trans. Nucl. Sci., Vol. 53, Issue: 5, Part 2, 2892-2896

[128] J. W. J. Williams. "Algorithm 232 - Heapsort," Communications of the ACM 7(6): 347348, (1964).

[129] S. Carlsson, "Average-case results on heapsort," BIT 27(1): 2-17, (1987).

[130] N. Tagg, *et al.*, "Arachne - A web-based event viewer for MINERνA," Nucl.Inst.Meth. 676 (2012) 44-49.

[131] R. Fruhwirth, "Application of Kalman Filtering to Track and Vertex Fitting," Nucl.Instrum.Meth. A262 444-450, (1987).

[132] W. D. Hulsbergen, "Decay Chain Fitting with a Kalman Filter," Nucl.Instrum.Meth. A552 566-575 (2005).

[133] R. J. Barlow and C. Beeston, Comput. Phys. Commun. 77, 219 (1993).

[134] M. Lefebvre, R.K. Keeler, R. Sobie, J. White, "Propagation of Errors for Matrix Inversion," Nucl.Instrum.Meth. A451 (2000) 520-528.

[135] J. Bell, C. T. Coffin, R. N. Diamond, H. T. French, W. C. Louis, B. P. Roe, R. T. Ross and A. A. Seidl *et al.*, "A Study Of The Reaction Neutrino P $\rightarrow$ Mu- Delta++ At High-energies And Comparisons With Theory," Phys. Rev. Lett. **41**, 1012 (1978).

[136] Hugh Gallagher, personal communication.

[137] J. Beringer et al. (Particle Data Group), Phys. Rev. D86, 010001 (2012).

[138] William H. Press, Saul A. Teukolsky, William T. Vetterling, and Brian P. Flannery, "Numerical Recipes 3rd Edition: The Art of Scientific Computing," Cambridge University Press, (2007).

[139] T.Golan, C. Juszczak, J. Sobczyk, "Final State Interactions Effects in Neutrino-Nucleus Interactions," arXiv:1202.4197.

[140] http://www2.dupont.com/Tedlar_PVF_Film/en_US/index.html.

[141] http://www.eljentechnology.com/index.php/joomla-overview/paints/86-ej-510.

[142] http://www.momentive.com/Products/TechnicalDataSheet.aspx?id=3994.

[143] N. Tagg *et al.*, Nuclear Instruments and Methods in Physics Research A 539 (2005) 668678.

[144] http://www.tek.com/datasheet/data-pattern-generator.

[145] J. Estrada, C. Garcia, B. Hoeneisen, and P. Rubinov, "MCM II and the Trip chip", FERMILAB-TM-2226; (2004).

[146] B.Tice et all ”Measurement of ratios of ?? charged-current cross sections on C, Fe, and Pb to CH at neutrino energies 2?20 GeV”, Phys. Rev. Lett. 112, 231801 (2014).

APPENDIX

THE MINERνA COLLABORATION

G. Tzanakos

University of Athens

J. Cravens, M. Jerkins, S. Kopp, J. Ratchford

University of Texas at Austin

D.A.M. Caicedo, C.M. Castromonte, H. da Motta, G.A. Fiorentini, K. Hurtado, J.L. Palomino

Centro Brasileiro de Pesquisas Físicas

D.W. Schmitz

University of Chicago

J. Grange, J. Mousseau, B. Osmanov, H. Ray

University of Florida

D. Boehnlein, R. DeMaat, N. Grossman, D.A. Harris, J.G. Morfín, J. Osta, E. A. Paschos,
L. Rakotondravohitra, P. Rubinov, F.D. Snider, R. Stefanski

Fermilab

A. Blondel, A. Bravar, Y. Karadzhov, A. Korzenev, C. Martin Mari

University of Geneva

J. Felix, A. Higuera, Z. Urrutia, E. Valencia, G. Zavala

Universidad de Guanajuato

M.E. Christy, M. Datta, C. Keppel, W. Tan, T. Walton, L. Y. Zhu

Hampton University

A. Butkevich, S.A. Kulagin

Inst. Nucl. Reas. Moscow

G. Niculescu, I. Niculescu

James Madison University

E. Maher

Mass. Col. Lib. Arts

L. Fields, B. Gobbi, J.A. Hobbs, C.E. Patrick, L. Patrick, H. Schellman

Northwestern University

N. Tagg

Otterbein University

S. Boyd, S.A. Dytman, B. Eberly, Z. Isvan, C.L. McGivern, D. Naples, V. Paolone, L. Ren

University of Pittsburgh

G.A. Díaz , A.M. Gago, J.P. Velásquez

Pontificia Universidad Catolica del Peru

R. Napora

Purdue University Calumet

S. Avvakumov, A. Bodek, R. Bradford, H. Budd, J. Chvojka, M. Day, H. Lee, L. Loiacono, S. Manly, C.M. Marshall, K.S. McFarland, A.M. McGowan, A. Mislivec, J. Park, G.N. Perdue, P.A. Rodrigues, J. Wolcott

University of Rochester

G. J. Kumbartzki, T. Le, R.D. Ransome, E.C. Schulte, B.G. Tice

Rutgers University

O. Altinok, H. Gallagher, T. Kafka, W.A. Mann, W. P. Oliver

Tufts University

C. Simon, B.P.Ziemer

University of California at Irvine

R. Gran, M. Lanari

University of Minnesota at Duluth

M. Alania, C.J. Solano Salinas

Universidad Nacional de Ingeniería

W.K. Brooks, G. Maggi, J. Miller, C. Peña, I.K. Potashnikova, F. Prokoshin

Universidad Técnica Federico Santa María

L. Aliaga, J. Devan, M. Kordosky, J.K. Nelson, J. Walding, D. Zhang

College of William and Mary